

THE GEONEUTRINO SIGNAL IN THE SNO+ EXPERIMENT

by

INGRIDA SEMENEC

A thesis submitted to the
Department of Physics, Engineering Physics & Astronomy
in conformity with the requirements for
the degree of Doctor of Philosophy

Queen's University
Kingston, Ontario, Canada

November 2023

Copyright © Ingrida Semenec, 2023

Abstract

Since their first laboratory detection in 1956, neutrinos have played a unique role in our developing understanding of the universe around us. Because they are the only particle that interacts exclusively through the weak force, neutrinos interact very infrequently with matter, allowing most neutrinos to pass through many kilometers of matter without interacting. While this makes neutrinos hard to detect, it also allows for unique insights regarding processes occurring deep within the interior of the Sun and Earth. This thesis details the first SNO+ detection of antineutrinos coming from deep within the Earth's crust, produced in radioactive decays of uranium and thorium. Calibration processes are undertaken to study the detector response to neutrons, which is needed to characterize the $^{13}\text{C}(\alpha,\text{n})^{16}\text{O}$ background events versus the antineutrino interactions. The antineutrino events are characterized by the prompt annihilation of a positron with an electron, followed by the delayed production of gamma rays produced when hydrogen or carbon captures the produced neutrons. Both the promptly annihilating positron and delayed neutron capture signals are produced by the antineutrino inverse β decay interaction with protons, $\bar{\nu}_e + p \rightarrow n + e^+$. The geoneutrino flux observed at SNO+ will be particularly important for developing geophysical models, and in particular clarifying the Bulk Silicate Earth model, since

this is only the third time this measurement has been possible, following prior measurements in Japan at Kamland and in Italy at Borexino. In this thesis, we discuss the observation of 55 candidate antineutrino events for 110.8 days of data, which were then fit using a maximum likelihood method based on the prompt energy distributions, resulting in 15.2 ± 4.9 identified geoneutrino events. This number corresponds to 109 ± 35 TNU compared to the expected MidQ model prediction of $46.2^{+10.8}_{-7.5}$ TNU. We provide an introduction to geological models relevant to this thesis and discuss the implications of our findings for geophysical models, including suggestions for future analyses that can be undertaken at SNO+.

Acknowledgments

First of all, I would like to say thank you to my supervisor Mark Chen, for guiding me on my Ph.D. journey, even though it did include “tricking” me into trying nattō. I will always appreciate the amazing opportunities you have brought to me. During the completion of this thesis, I have benefited from collaborating with members of the SNO+ collaboration, and especially Charlie Mills, Janet Rumleskie, Serena Riccetto, Ryan Bayes, Erica Caden, Christine Kraus, Anthony Zummo, Logan Lebanowski, Stefan Nae. A very special place in my heart will always be dedicated to the fantastic neutrino geoscience meetings with Laura Sammon, Scott Wipperfurth, Ondřej Šrámek, Bill McDonough, Hiroko Watanabe, Bedřich Roskovec, Yufei Xi, Wolfgang Szwilus, Weisen Shen and Kai Watanabe-McDonough. Our discussions left me with a lifelong love for geology. I wish to thank my mother Lolita, and my grandmother Felicia: Noriu padėkoti mamai Lolitai ir močiutei Felicijai, kurių begalinė meilė ir pastangos sudarė man salygas būti smalsiai, studijuoti, nebijoti pasaulio, bet norėti ji pažinti. Most love for my husband Joseph Bramante along with our cats Pepper, Paprika, and Wasabi for their support during the completion of my PhD research and for being a continuous joy in my life.

Statement of Originality

This thesis was written by the author, including text and figures, except for figures adapted from other works as indicated in captions. The scientific analysis presented was conducted with input from the author's adviser, members of the SNO+ collaboration, and members of the geological scientific community. In particular, the author collaborated and gave input and corrections via meetings for the geoneutrino signal prediction code modifications performed by Laura Sammon, based on Scott Wipperfurth's MatLab code as cited and specified in the text. The author constructed a geoneutrino event generator for the SNO+ Monte Carlo simulation framework, by adding required production spectra and rates based on predictions. The author also analyzed AmBe external deployment data, as detailed in Chapter 5. For the analysis of the full scintillator data, the author created a coincidence selection code, muon tagging/veto scripts, and RooFit likelihood fit code. The author computed or collected computations of a number of backgrounds from collaborators - all outside contributions are indicated and cited in the text.

Contents

Abstract	i
Acknowledgments	iii
Statement of Originality	iv
Contents	v
List of Tables	viii
List of Figures	xii
Chapter 1: Introduction	1
1.1 A Brief History of the Neutrino	1
1.2 Neutrino Oscillations	2
1.2.1 Neutrino Oscillations in Vacuum	4
1.2.2 Neutrino Oscillations in Matter	10
1.3 Geoneutrinos	14
Chapter 2: Neutrino Geoscience Background and Motivation	18
2.1 Primordial and Radiogenic Heat in the Earth	18
2.2 Bulk Silicate Earth Models	20
Chapter 3: The SNO+ experiment and antineutrino detection	31
3.1 The SNO+ Experiment	31
3.1.1 Water Phase	32
3.1.2 Partial Fill Phase	32
3.1.3 Scintillator Phase	35
3.1.4 Tellurium Loaded Phase	35
3.2 Detector	37
3.3 Antineutrino Detection	38
3.3.1 IBD Cross Section	42

3.4	Event Simulation and Analysis Software	42
Chapter 4:	Geoneutrino Signal Prediction and Modeling	47
4.1	Geoneutrino Signal Calculation	48
4.2	Geoneutrino Rate Predictions for SNO+	50
4.2.1	Šrámek Model	50
4.2.2	Wipperfurth Model	52
4.3	Refined Regional Model	54
4.4	Geoneutrino Signal Prediction Comparison	59
Chapter 5:	Study of the $^{13}\text{C}(\alpha,\text{n})^{16}\text{O}$ Background for Geoneutrinos	61
5.1	The alpha-n Background	63
5.2	AmBe Neutron Source Calibration	69
5.3	AmBe Calibration Dataset	70
5.4	AmBe ΔT Feature	73
5.5	alpha-n IBD classifier	82
5.6	Proton Recoil Classifier Calibration	85
5.7	IBD Classifier Result	87
Chapter 6:	The Geoneutrino Search at the SNO+ Experiment	96
6.1	SNO+ Geoneutrino Dataset Selection	96
6.1.1	Event Reconstruction	97
6.1.2	Position Dependent Energy Correction	99
6.1.3	Target Protons	100
6.2	SNO+ Antineutrino IBD Backgrounds	102
6.2.1	Alpha-N	103
6.2.2	Atmospheric Neutrinos	105
6.2.3	Reactor Antineutrinos	106
6.2.4	Muon/High-NHit Veto and Multiplicity Cut	112
6.2.5	Accidental Events	114
6.3	Event Selection	114
6.3.1	Prompt and Delayed Event Distance Correlation	114
6.3.2	Prompt and Delayed event Time Correlation	115
6.3.3	Analysis cuts for IBD selection	117
6.4	Coincidence Tagging Algorithm	119
6.4.1	Coincidence Algorithm Classes	121
6.4.2	Coincidence Algorithm Functions	121
6.5	Geoneutrino Flux Result	124
Chapter 7:	Summary and Discussion	135
7.1	Summary	135

7.2	Overview of Previous Geoneutrino Measurements and Discussion . . .	136
7.3	Future Work	144
Bibliography		147

List of Tables

4.1	Variable definitions for Equation (4.1). Note that this is valid for a single radiogenic element. In this work, we sum over contributions from uranium and thorium to the geoneutrino flux.	49
4.2	Output of SNO+ geoneutrino signal calculations provided by Ondřej Šrámek, based on methods detailed in Šrámek et al. 2016 [55]. This shows the expected geoneutrino flux in TNU at SNO+, according to different radiogenic heat models.	51
4.3	Abundance estimates in terms of mass fraction of the element and the rock (kg/kg). For each layer, the abundances were assumed to be uniform [55].	51
4.4	Comparison of expected geoneutrino signal (in TNU) from each geo-physical crust composition model, from Wipperfurth’s code [66]. The top row is the contribution coming from the continental crust (CC) and the bottom row is the total signal.	53

4.5	Results of fifteen thousand iterations of our modified Wipperfurth MATLAB Monte Carlo simulation code [66], which incorporates three models of the Earth’s Bulk Silicate Region [56, 57, 58]. The Wipperfurth code was extended to include a high-resolution geological composition model around the detector. The high-resolution model was constructed by using the MATLAB CrustMaker package created by Laura Sammon during her research on the lower crustal composition in the Southwestern United States [72]. In addition, the upper crust was modeled using the Strati et al. model of the CUC, detailed in [68].	57
4.6	Comparison of total expected geoneutrino signal (in TNU) from Šrámek MidQ, Wipperfurth LITHO1, and Sammon & Semenec (where these latter models are also MidQ).	60
5.1	Summary of the AmBe coincidence selection cuts applied to calibration data.	72
5.2	The expected efficiency of the MC simulated signal and background statistics for the two proposed classifier cuts, $CR > -10, 0$ where the MC simulated classifier result values are shown in Figures 5.17 and 5.18. In order, the efficiencies for cut events are shown for uranium, thorium, alpha-n, and reactor Monte Carlo data.	91
6.1	An abbreviated list of run selection criteria for “gold”, “silver”, and “bronze” run lists.	97

6.2	The fuel isotope fission fractions for the modeled reactor designs in RAT. Representative fission fraction data for PWR and BWR was taken from [94] and data for PHWR were given in private SNO+ communication with Atomic Energy of Canada (AECL) in 2013.	107
6.3	Summary of the antineutrino candidate coincidence selection cuts applied to data ntuples for the geoneutrino IBD antineutrino analysis of this thesis. The cumulative efficiency for parameter cuts applied to official production MC geoneutrino IBD and alpha-n events is shown. Cuts shown at the bottom are the data cleaning mask, the Muon High Nhit cut which was applied to data, and the FitValid precut discussed in the text. The total parameter cut efficiency for the alpha-n MC event sample was $71.203(\pm 0.075)\%$ and for the IBD events was $80.87(\pm 0.23)\%$.	120
6.4	Fit values for the 55 IBD coincidence candidate events selected from 110.8 days of SNO+ “gold” run full scintillator fill data. An extended maximum likelihood fit was performed using four probability density functions generated using run-specific MC production. The reactor PDF for this fit was generated using $\Delta m_{21}^2 = 7.53 \times 10^{-5}\text{eV}^2$ [98]. The fit had two external constraints discussed in the text: $N(\alpha, n) = 17.4 \pm 5.2$, $U_{geonu}/Th_{geonu} = 3.74 \pm 1.3$.	129
6.5	Fit parameter correlation matrix corresponding to the fit result described in Table 6.4. YieldA, yieldR, yieldTh, and yieldU correspond to alphaN, reactor antineutrinos, thorium, and uranium geoneutrinos respectively.	130

6.6 Same as Table 6.4, but the reactor PDF was generated using $\Delta m_{21}^2 =$ $5.00 \times 10^{-5} \text{ eV}^2$.	130
--	-----

List of Figures

2.1 A simplified illustration of Bulk Silicate Earth (BSE) models, where the Earth is classified by the dominance of Lithophile (“rocky”) elements in its crust and mantle and siderophile (“metallic”) elements in its core. Of importance to this thesis, the Lithophile elements include the radiogenic elements thorium, uranium, potassium, which can be used to test models of the abundance and distribution of Lithophile elements in the Earth.	22
2.2 Log elemental abundances of the solar photosphere, measured using spectroscopic methods, versus the log element abundances of the C1 Chondrites, taken from [37]. These solar photosphere spectra are enriched in non-volatile noble gasses, which have abundances that are elevated above the visible trend. The spectra are comparatively underabundant in lithium, since it is consumed by Lithium fusion processes in the solar core, leading to a Lithium abundance lying below the general trend. The most important takeaway is that C1 Chondrite meteorites appear to provide a good model for the likely geological composition of bodies formed during the primordial formation of our Solar System.	24

2.5 This pie chart illustration shows the relative proportions of the heat produced in the mantle (orange) and the crust (blue) for each of Bulk Silicate Models indicated. The complete pie chart shows the relative pie slice proportions using the MidQ model (Wipperfurth et al. (2019) [43], McDonough & Sun (1995) [41]). However, the range in heat flux (given in TW) as shown in this largest pie includes the range of allowed values for all three models, LowQ, MidQ, and HighQ. The red dashed line denotes the radiogenic portion of the Earth’s heat budget, which can be measured using geoneutrinos.	29
3.1 A photo of the SNO+ detector during the partial fill. The interface between water and scintillator is noted with the arrow, where the less dense liquid scintillator floated atop the water. While unexpected, this partial-fill phase permitted a number of useful physics analyses. . . .	33
3.2 Illustration of the SNO+ detector [46]. The hold-down and hold-up ropes are visible, securing the Acrylic Vessel in a structure surrounded by photomultiplier tubes arranged in triangular and hexagonal formations on a photomultiplier tube support structure. The PMTs and associated concentrators cover about 54% of the solid angle surrounding the acrylic vessel. External to the acrylic vessel, a volume of water acts as shielding as an external muon veto.	36

3.3 Muon flux versus the depth of various underground experimental labs, given in meters of water equivalent [50]. The red and blue dashed lines represent different modeling approaches. The red dashed line is from an empirical formula for the muon flux for sites located directly underground, or “down a mineshaft.” The blue dashed line and shaded region represent the fit result from a GEANT4 model of the muon flux for sites underneath mountains. In this case, less rock shielding at shallow angles leads to more muon flux, compared to using the empirical formula appropriate for down mineshaft sites.	38
3.4 The Feynman diagram for the Inverse Beta Decay (IBD) reaction, where an electron antineutrino exchanges a W boson with a proton, thereby converting the proton into a neutron, and converting the electron antineutrino into a positron.	39
3.5 Illustration of an electron antineutrino detection inside a scintillator detector. The electron antineutrino interacts with a proton producing a positron and a neutron. The positron energy deposition and annihilation produce light, while the neutron thermalizes and gets captured by a nucleus which results in the emission of a 2.2 MeV γ and provides the visible light for the delayed event.	41

3.6 The rate for antineutrino production by labeled elements (solid lines) are shown on the left-side y-axis, as in Figure 1.2. Here this can be usefully compared to the cross-section for inverse beta decay given in Equation (3.6), shown on right-side y-axis (dashed line). It can be seen that the cross-section for IBD drops sharply around the IBD threshold of $E_{th} = 1.806$ MeV.	43
3.7 Example of the modified GEANT-4 generated MC of antineutrino interaction rate versus the inferred energy in SNO+ from the prompt event at SNO+. This plot depicts expected geoneutrino fluxes from ^{238}U and ^{232}Th in blue and red respectively with their proportions based on MidQ model calculations found in [55]. The green histogram shows the simulated reactor neutrino spectrum, including the effects of neutrino oscillations (for $\Delta m_{21}^2 = 7.53 \times 10^{-5}$ eV 2). Alongside this, the plot shows what the reactor spectrum would look like in the absence of neutrino oscillations, with the dotted line.	44

4.4 The distribution of Th in the nearfield crust model at example depths of 1km, 20km, and 30km. Color corresponds to the concentration of U(ppm). The white star marks the detector location, which is not centered due to 47 degrees latitude being the extent of the USArray seismic array [73]. White circles mark the location of seismic stations in the array.	59
4.5 The total expected geoneutrino signal in TNU for the SNO+ experiment (y-axis) versus the total U+Th radiogenic power in TW (x-axis). The scatter plot shows a total of fifteen thousand iterations of the modified Wipperfurth MATLAB code developed by Sammon and the author. Each point is one iteration, and the color map represents the point density.	60
5.1 The complete ^{238}U decay chain is shown, taken from [75], of which ^{222}Rn is a subset.	65

5.4 AmBe external deployment coincidence event prompt (top) and delayed (bottom) event positions in the acrylic vessel, given in x-y coordinates. No fiducial volume cuts were applied to these coincidence events, for illustration purposes. Both figures extend to AV volume, which is 6 m. These plots demonstrate that most interactions from the AmBe calibration source occurred at the edge of the SNO+ detector. This will be useful to keep in mind when examining the AmBe timing anomaly discussed below.	71
5.5 Schematic showing the top down view of SNO+ Deck Clean Room (DCR). Indicated in red are the calibration source deployment guide tube locations relative to the detector neck position.	72
5.6 Prompt coincidence event energies from AmBe external deployment data, after coincidence cuts are applied as given in Table 5.1. These are similar cuts that are also applied to select for the antineutrino inverse beta decay interaction. The shaded green is the energy area where most of the proton recoils are expected to be since these produce around 0.5-2 MeV prompt events (through the same interactions detailed for alpha-n neutrons in Section 5.1). The shaded red area shows that some neutrons captured on hydrogen are being tagged as prompt events as there is an evident bump at the characteristic 2.2 MeV gamma energy that is emitted when a proton is captured on hydrogen. The yellow shaded area contains the 4.4 MeV γ peak which is emitted in some AmBe events from excited carbon produced in the AmBe reaction. . .	74

5.7	Delayed coincidence event energy spectrum from AmBe August 2022 external deployment data.	75
5.8	The time separation ΔT between prompt and delayed event pairs is shown, where this data has been cut to emphasize prompt energies around 4.4 MeV (the cut made was $3.8 < E_p < 5.1$ MeV). Here we note that in each run, a visible deficit of events is apparent at a time difference of around $100\mu\text{s}$. This effect has been noted in three separate AmBe source deployment datasets from August 2022, May 2022, and February 2023.	76
5.9	The coincident event time separation ΔT between prompt and delayed event pairs is shown. Figures made for the August 2022 dataset, cut at different prompt energy regions according to figure 5.6. As well as a check on a very low energy region, by using a cut on nhits to be below a 100.	77
5.10	Measured AmBe neutron energy spectra. Three regions represent the neutrons produced depending on the carbon nuclei state. 1. ^{12}C was in second excited state. 2. ^{12}C was in 1st excited state. 3. ^{12}C was in ground state. [79]	79

5.11 The absorption and elastic scattering cross sections for neutrons of varying energies are shown, where cross sections for this plot were obtained from [80]. It is apparent that the scattering cross section neutrons on carbon and oxygen have resonances in the MeV energy region that is of interest for AmBe calibration. These cross sections are used to compute fast neutron diffusion lengths for the toy MC results presented in Figure 5.13. Further studies of this timing feature are underway.	80
5.12 Neutron diffusion length in water versus the neutron energy in MeV, using cross sections shown in 5.11.	81
5.13 The result of the toy MC showing the shift in the neutron capture time for 3, 4, and 5 MeV neutrons.	81
5.14 The alpha-n and IBD time residual pdfs created by Charlie Mills for the scintillator phase [76]. We can see that for $^{13}\text{C}(\alpha,\text{n})^{16}\text{O}$ the distribution has a broader peak and tail which can be explained by multiple proton scatters over a longer timescale than that of γ energy deposition for prompt IBD events.	84
5.15 Time difference between the prompt and delayed proton recoil coincidence event from AmBe external deployment data, where this data has been cut so that the prompt event has an energy $E_p < 1.7$ MeV, below which most coincidence events should have prompt events from proton recoils. The blue line gives the data histogram as measured from the AmBe source and the green dashed line shows an exponential fit. . .	86

5.16 The top plot shows the proton recoil time residual probability distribution functions, normalized, with a comparison between August AmBe external deployment data and the MC simulation for detector settings and state during the same period, where the AmBe data was selected to have mostly proton recoil prompt events by applying a cut $E_p < 1.7$ MeV to prompt events. The probability shown on the y-axis is the same probability function that defines the log-likelihood probability parameter in Equation (5.7), which itself is used in the alpha-n versus IBD classifier tested in this section. The MC was produced with RAT version 7.0.9. The lower box shows the residuals of the timing residual PDFs, between the simulation and data.	88
5.17 The classifier result values are shown for Monte Carlo simulations of α -n and the geoneutrino signals. The lines at -10 (orange) and at 0 (pink) will define the later explored cuts to determine the expected efficiency sacrifice after cuts of classifier result value $CR > -10$ and $CR > 0$ are applied to the full analysis of IBD antineutrino data at SNO+.	89
5.18 Same as figure 5.17 except the classifier result values are shown in a 2-D plot showing coincidence event prompt energies, for MC productions of alpha-n, along with thorium and uranium geoneutrinos. Event density is mapped with a color scale that increases from purple to red. The classifier value has some energy dependence with a notable increase in classifier result for higher energy uranium geoneutrino events.	90

5.19 Best fit fluxes are shown for geoneutrinos, reactor antineutrinos, and alpha-n backgrounds, after a classifier result value cut of $CV > -10$ and $CV > 0$ is applied to 107 days of data. See Equation (5.8) for the classifier definition. For a full accounting of the cuts and data analysis presented here, see Chapter 6. The expected signal efficiency for both IBD classifier values shown, -10 and 0 , are well below the efficiency predicted from Monte Carlo simulations shown in Table 5.2.	94
6.1 Energy correction using $^{214}\text{BiPo}$ tagged events. Binned correction map for tagged ^{214}Bi events. The left panel shows the correction map that can be applied to data, and the right panel shows the correction for the MC events [84].	100
6.2 The before (left) and after (right) of applying energy correction to AmBe data for events at $5.2 < R < 5.7$ m. Figure made by Tanner Kaptanoglu.	101
6.3 The measured ^{210}Po rate within detector fiducial over the data taking period from 29/04/22 to 5/3/23 (shaded in green). Each rate measurement shown above is normalized to a fiducial volume for the run, as indicated. Figure by V.Lozza, created as part of an internal SNO+ document.	103
6.4 Energy spectra of the emitted antineutrinos from each isotope of CANDU nuclear fuel accounting for the fission fractions presented in Table 6.2. These are combined with a detailed reactor Monte Carlo code to predict the total reactor antineutrino rate versus energy plot shown in Figure 6.5. Figure from [97].	109

6.5	The MC simulation of expected antineutrino spectrum for SNO+, particularly focusing on showing individual reactor contributions. Here the geoneutrino rate is arbitrary and used for illustration purposes. Shown are the contributions from the nearest reactors compared to the reactors further away from the experiment site. Plot made by Stefan Nae from an internal SNO+ document.	110
6.6	The probability density functions of the prompt event energy spectrum from the reactor antineutrino prediction at SNO+ using different Δm_{21}^2 values. This can be compared to the two different geoneutrino IBD fit results presented in Section 6.5, which use these PDFs to determine how the fit changes with variation of Δm_{21}^2	111
6.7	Distance between the prompt and delayed event (ΔR) distributions from thorium (top) and uranium (bottom). Data is obtained from the official Monte Carlo production simulations of geoneutrino IBD events in the SNO+ detector. Simulated events get uniformly distributed in the AV volume.	116
6.8	Time between the prompt and delayed event (ΔT) distributions from thorium (top) and uranium (bottom). Data is obtained from Monte Carlo simulations of geoneutrino IBD events in the SNO+ detector. .	118
6.9	Tagged coincidence counts versus the prompt event reconstructed radial position from the AV center. Here we see positions ranging from 4.5 m to 6 m, to illustrate the choice of 5.7 m FV volume cut. . . .	119

6.10 The pull distributions for each parameter from the ensemble test with 1000 pseudo-experiments. Here yield0, yield1, yield2, and yield3 correspond to uranium and thorium geoneutrinos, reactor antineutrinos, and alphaN background respectively.	127
6.11 The prompt energy (MeV) of 55 IBD coincidence candidate events selected from 110.8 days of SNO+ “gold” run full scintillator fill data. An extended maximum likelihood fit was performed using four probability density functions generated using run-specific MC production. The thorium produced geoneutrino PDF can be seen in red and uranium geoneutrinos are shown in blue. The reactor PDF (green) was generated using $\Delta m_{21}^2 = 7.53 \times 10^{-5}\text{eV}^2$. The alpha-n PDF (yellow) measured rate of $N(\alpha, n) = 17.4 \pm 5.2$ was used as an external constraint, along with the second external constraint on the uranium to thorium ratio, $U_{\text{geonu}}/Th_{\text{geonu}} = 3.7 \pm 1.3$. Fit result values can be seen in Table 6.4.	128
6.12 Same as Figure 6.11, which is the main result of this analysis, but in this fit we have tested the effect of setting $\Delta m_{21}^2 = 5.00 \times 10^{-5}\text{eV}^2$. Fit result values can be seen in Table 6.6.	129
6.13 2D histogram of fit parameter correlation matrix corresponding to the Table 6.5. YieldA, yieldR, yieldTh, and yieldU correspond to alphaN, reactor antineutrinos, thorium, and uranium geoneutrinos respectively.	130

6.14 Time between prompt and delayed events of the observed coincidence pairs fitted to an exponential. The mean time for neutron capture in SNO+ scintillator is expected to be around $200 \mu\text{s}$ and the fit here gives a mean $\Delta T = 179 \pm 63 \mu\text{s}$, which is within the expectation. . .	132
6.15 Delayed event reconstructed energy for the 55 IBD coincidence events in our full fit analysis presented in Table 6.4. Uranium geoneutrino Monte Carlo simulation data, normalized to 55 events, is overlaid for comparison.	133
6.16 Distance between the prompt and delayed events for the 55 IBD coincidence events in our full fit analysis presented in Table 6.4. Uranium geoneutrino Monte Carlo simulation data, normalized to 55 events, is overlaid for comparison.	134
7.1 Schematic drawing of the KamLAND detector[17].	138
7.2 Schematic drawing of the Borexino detector [106].	138
7.3 First ever measured antineutrino energy spectrum, taken at KamLAND. The main panel shows the data points with the total expectation given in the thin black dotted line. The total expected spectrum is shown without the geoneutrino signal as a thick black line. The expected ^{238}U and ^{232}Th signals are shown in a dot-dashed red line and dotted green line respectively. The brown dotted line shows the alpha-n background. [108]	139
7.4 Light yield prompt event spectrum from 21 candidate events. The geoneutrino contribution is shown in the darker etched area. [109] . .	140

7.5	Light yield spectral plot of Borexino 154 prompt IBD candidate events. In blue geoneutrinos are shown for a fixed ratio of Th/U = 3.9. Reactor neutrinos are shown in yellow. [25]	140
7.6	Stacked prompt energy spectrum for three periods of data. Period 1 is from 2002 to 2007, period 2 from 2007 to 2011 and period 3 from 2011 to 2020 [103]. The area in white is the fitted reactor neutrino background. above in green the alphaN and in peach accidental backgrounds. The blue-shaded area is the best-fit geoneutrino spectrum.	142
7.7	Illustration of the historical perspective on the geoneutrino measure- ments reported by KamLAND and Borexino. Each result is extrap- olated to TNU. KamLAND results from [108][111][112][107][103]. Borex- ino results from [109][113][114][25]. For SNO+, in red the measurement from this thesis, as well as a prediction for a measurement using MidQ model production for 2 years worth of data in gray.	143

Chapter 1

Introduction

1.1 A Brief History of the Neutrino

The neutrino was first postulated in 1930s by Wolfgang Pauli [1], while he was trying to find the missing energy in nuclear Beta decay experiments. Pauli proposed a neutral, spin-half, weakly interacting particle to carry away the missing energy and momentum in these β decay interactions. This sparked the interest of Enrico Fermi, who later gave the particle the name “neutrino”, which is a diminutive Italian coinage meaning “neutral little one” [2]. Fermi’s theory included weak interactions to explain the continuous β -decay energy spectrum, where these weak interactions were modeled to fit neutron decay data from a process wherein neutrons decayed to a proton, electron, and neutrino, $n \rightarrow p + e^- + \nu_e$. It took more than 20 years for the first neutrino to be detected. In 1956 F.Reines and C.Cowan confirmed the detection of electron antineutrinos at the Savannah River nuclear reactor [3] [4]. One of the first proposals for finding neutrinos involved producing them with a nuclear bomb as a neutrino source, but after careful consideration Reines and Cowan decided to use a nuclear reactor instead. It took another 10 years to observe electron neutrinos

produced from nuclear reactions in the sun by R.Davis and his collaboration at the Homestake gold mine in 1968 [5]. As additional solar neutrino data was collected, and these were compared against solar nuclear reaction predictions [6] it became clear that the number of the observed neutrinos was only one third of the theoretical prediction, and this disagreement created increased interest in neutrino physics trying to resolve the “Solar Neutrino Problem”. Much earlier, some authors had suggested a possible solution to this problem: in 1962 Maki, Nakagawa and Sakata suggested the idea of neutrino oscillations, which implied that neutrinos would change flavor as they traveled [7]. This proposal coincided with the first time another neutrino was measured, namely the measurement of a muon neutrino by Lederman, Schwartz, and Steinberger [8]. The measurement of the third neutrino flavor would not come until the year 2000 when the tau neutrino was detected by the DONUT experiment [9].

1.2 Neutrino Oscillations

As discussed above the “Solar Neutrino Problem” eventually led to the discovery of neutrino oscillations. The purpose of the Homestake experiment was to detect neutrinos emitted by the nuclear fusion reactions in the Sun. The experiment involved a neutrino capturing on chlorine to form argon $\nu + {}^{37}\text{Cl} \rightleftharpoons {}^{37}\text{Ar} + e^-$. After the Homestake experiment completed its data-taking and analysis, that experiment observed solar neutrino fluxes coming from ${}^8\text{B}$ and ${}^7\text{Be}$ that were in total around 1/3 of the Standard Model predictions [10].

Long prior to Homestake’s results, Bruno Pontecorvo was the first to postulate that if neutrinos have mass, then it would be possible for neutrinos to oscillate between flavor states [11]. In that paper both the oscillation between particle and antiparticle

neutrinos, $\nu \rightleftharpoons \bar{\nu}$, along with flavor oscillations, $\nu_e \rightleftharpoons \nu_\mu$ were detailed. Robert Ehrlich then suggested that Pontecorvo's theory could solve the solar neutrino problem [12]. If it was possible for ν_e and ν_μ to oscillate between themselves, a fraction of electron neutrinos coming from the sun would transform into muon or even tau neutrinos, before they were detected on Earth, resulting in an effective loss of observed neutrinos, since at the time solar neutrinos were being detected solely as electron (as opposed to muon or tau) neutrinos.

The first breakthrough in the measurement of neutrino oscillations was presented by Super-Kamiokande in 1998 [13]. Super-Kamiokande is a large-scale water Cherenkov experiment. They measured the asymmetry in the flux of upward-going muon neutrinos traveling through the Earth compared to the atmospheric neutrinos coming from above the detector [14], thereby obtaining the first measurement of atmospheric neutrino flavor oscillations. A few years later on June 18th, 2001 the Sudbury Neutrino Observatory (SNO) announced their first solar neutrino results [15] explaining the missing solar neutrinos. Alongside another paper published in 2002 [16], SNO definitively demonstrated that ν_e produced from ^8B decays in the sun, undergo a flavor transition, which resolved the solar neutrino problem. Compared to Super-Kamiokande, the SNO experiment had a unique advantage, as they used heavy water as the target volume, which meant that they were sensitive not only to charged current (CC, equation (1.1)), but also neutral current (NC, equation (1.2)) and elastic

scattering (ES, equation (1.3)) interactions with deuterium (d):



Prior to this no other single experiment was sensitive to neutrino flavors through this many interaction channels. In measuring the total electron neutrino flux alongside the total neutrino flux for all flavors, SNO confirmed what had been predicted by the standard solar model [6], and observed the mixing between ν_e , ν_μ , and ν_τ .

The KamLAND experiment [17] in 2005 then subsequently published a measurement of reactor antineutrinos [18]. In their measurement, they similarly observed that the measured energy spectrum disagreed with the expected spectral shape in the absence of neutrino oscillation at 99.6% significance and preferred a model with flavor oscillation effects.

1.2.1 Neutrino Oscillations in Vacuum

The process of neutrino flavor change, which is also referred to as “neutrino oscillation,” occurs as neutrinos propagate through space. This is most commonly described using a quantum mechanical description where the neutrinos are traveling in a quantum superposition of flavor states. More technically, the usual treatment of neutrino propagation models them as a superposition of flavor eigenstates $|\nu_\alpha\rangle$ (where $\alpha = e, \mu, \tau$), which together in some proportion form a different superposition for each of the neutrino mass eigenstates $|\nu_k\rangle$ (where $k = 1, 2, 3$). The Equation (1.4) describes the flavor and mass states in superposition, where the $U_{\alpha k}^*$ is the weight term from

the unitary mixing matrix also called the Pontecorvo-Maki-Nagawa-Sakata (PMNS) matrix, given in Equation (1.6). The neutrino flavor basis is then related to the mass basis via

$$|\nu_\alpha\rangle = \sum_k U_{\alpha k}^* |\nu_k\rangle \quad (1.4)$$

$$\langle \nu_k | \nu_j \rangle = \delta_{kj}, \quad \langle \nu_\alpha | \nu_\beta \rangle = \delta_{\alpha\beta}, \quad (1.5)$$

where here we have indicated that each of the flavor and mass eigenbases are chosen to be orthonormal, *i.e.* δ_{kj} and $\delta_{\alpha\beta}$ are Kronecker delta functions. The PMNS matrix that relates these bases has the following usual form,

$$U = \begin{pmatrix} U_{e1} & U_{e2} & U_{e3} \\ U_{\mu 1} & U_{\mu 2} & U_{\mu 3} \\ U_{\tau 1} & U_{\tau 2} & U_{\tau 3} \end{pmatrix} \quad (1.6)$$

$$= \begin{pmatrix} 1 & 0 & 0 \\ 0 & c_{23} & s_{23} \\ 0 & -s_{23} & c_{23} \end{pmatrix} \begin{pmatrix} c_{13} & 0 & s_{13}e^{-i\delta} \\ 0 & 1 & 0 \\ -s_{13}e^{i\delta} & 0 & c_{13} \end{pmatrix} \begin{pmatrix} c_{12} & s_{12} & 0 \\ -s_{12} & c_{12} & 0 \\ 0 & 0 & 1 \end{pmatrix} \quad (1.7)$$

$$\text{where } U^\dagger U = \mathbb{1} \quad \text{and} \quad c_{ij} = \cos \theta_{ij}, \quad s_{ij} = \sin \theta_{ij} \quad (1.8)$$

are the customarily defined mixing angles between the neutrino eigenstates.

To give a fuller description of the three-flavor neutrino oscillations, it can further be said that the PMNS is a 3×3 matrix that is a representation of the $SO(3)$ group of unitary rotations. In Equation (1.8) the $\theta_{12}, \theta_{23}, \theta_{13}$ represent the three Euler angles

mixing the mass eigenstates. In Equation (1.7) the exponentiated δ factor, parameterizes a possible charge conjugation-parity phase for the PMNS matrix, usually called the CP-phase for short. If this phase is nonzero, it is possible that the PMNS matrix and neutrinos could be involved in the generation of the matter/antimatter asymmetry in the early universe. However, this would probably require additional particles beyond the Standard Model [19].

The evolution of neutrino mass eigenstates can be described by the Schrödinger Equation (1.9), where $E_k = \sqrt{\vec{p}^2 + m_k^2}$ are the eigenvalues.

$$H|\nu_\alpha\rangle = E_k|\nu_k\rangle \quad (1.9)$$

For the evolution of the mass eigenstates over time it is good to consider the time-dependent Schrödinger equation (Equation (1.10)) using a plane wave solution (Equation (1.11)). Equation (1.12) shows the evolution of flavor states in terms of mass states.

$$i\frac{d}{dt}|\nu_k(t)\rangle = H|\nu_k(t)\rangle \quad (1.10)$$

$$|\nu_k(t)\rangle = e^{-iE_k t}|\nu_k\rangle \quad (1.11)$$

$$\implies |\nu_\alpha(t)\rangle = \sum_k U_{\alpha k}^* e^{-iE_k t} |\nu_k\rangle \quad (1.12)$$

Then the mass states can be written as a superposition of flavor states $|\nu_k\rangle = \sum_\beta U_{\beta k} |\nu_\beta\rangle$ and substituted back into Equation (1.12), to show that in this framework, a neutrino created at $t = 0$ with a pure flavor state will be a superposition of

other flavor states at $t > 0$.

$$|\nu_\alpha(t)\rangle = \sum_{\beta,k} U_{\alpha k}^* e^{-iE_k t} U_{\beta k} |\nu_\beta\rangle \quad (1.13)$$

Furthermore, the amplitude of the transition Equation (1.15) can be used to express the canonical probability Equation (1.14) of one flavor changing to the other in terms of PMNS matrix elements, Equation (1.16)

$$P_{\nu_\alpha \rightarrow \nu_\beta} = |A_{\nu_\alpha \rightarrow \nu_\beta}(t)|^2 \quad (1.14)$$

$$A_{\nu_\alpha \rightarrow \nu_\beta}(t) \equiv \langle \nu_\beta | \nu_\alpha(t) \rangle = \sum_k U_{\alpha k}^* U_{\beta k} e^{-iE_k t} \quad (1.15)$$

$$\implies P_{\nu_\alpha \rightarrow \nu_\beta} = \sum_{k,j} U_{\alpha k}^* U_{\beta k} U_{\alpha j} U_{\beta j}^* e^{-i(E_k - E_j)t} \quad (1.16)$$

This probability can be further simplified considering that neutrinos are usually ultrarelativistic particles ($m \ll p$), from which we can approximate that $E = |\vec{p}|$. Using this approximation we can express the energy difference between two mass states as:

$$p = \sqrt{E^2 - m_k^2} = E \sqrt{1 - \frac{m_k^2}{E^2}} \approx E - \frac{m_k^2}{2E} \quad (1.17)$$

$$\implies E_k - E_j = \frac{(m_k^2 - m_j^2)}{2E} = \frac{\Delta m_{kj}^2}{2E} \quad (1.18)$$

In the experimental setting, we have to consider that the time at which the neutrino is created is usually harder to determine than knowing the distance, L , from the source to the detector. Since the neutrinos are ultrarelativistic we can use approximation $t \simeq L$. With all of this, substituting Equation (1.18) into Equation (1.16)

provides the expression of probability that can be more easily applied to the experimental analysis, given in Equation (1.19).

$$P_{\nu_\alpha \rightarrow \nu_\beta} = \sum_{k,j} U_{\alpha k}^* U_{\beta k} U_{\alpha j} U_{\beta j}^* e^{-i \frac{\Delta m_{kj}^2 L}{2E}} \quad (1.19)$$

In the case of reactor and accelerator neutrino experiments, L and E are known quantities and the measured spectral shape of neutrino energies can provide very good data for determining the neutrino oscillation probability. In particular, there are experimental programs based on both reactors and accelerators with known “baselines” and neutrino energies, to determine the values of the neutrino mass splittings Δm_{kj}^2 , along with the elements of the PMNS matrix U , which are probed using a variety of detectors [20].

It will be useful to examine a simplified neutrino mixing formalism for the discussion of matter effects and neutrino oscillations contained in the next section. Turning then to the case of two-flavor neutrino oscillations, we can reduce the comparatively ornate PMNS matrix to a simple rotational matrix, (1.20):

$$\begin{pmatrix} \nu_\alpha \\ \nu_\beta \end{pmatrix} = \begin{pmatrix} \cos \theta & \sin \theta \\ -\sin \theta & \cos \theta \end{pmatrix} \begin{pmatrix} \nu_1 \\ \nu_2 \end{pmatrix} \quad (1.20)$$

From which we can find the flavor state evolution over time using the Hamiltonian

treatment previously provided, in a simpler form

$$|\nu_\alpha(t)\rangle = \cos\theta e^{-iE_1 t}|\nu_1\rangle + \sin\theta e^{-iE_2 t}|\nu_2\rangle, \quad (1.21)$$

$$\text{where } |\nu_1\rangle = \cos\theta|\nu_\alpha\rangle - \sin\theta|\nu_\beta\rangle \quad (1.22)$$

$$|\nu_2\rangle = \sin\theta|\nu_\alpha\rangle + \cos\theta|\nu_\beta\rangle \quad (1.23)$$

$$(1.24)$$

From this we can express the evolution of the neutrinos in terms of flavor states and not mass states:

$$|\nu_\alpha(t)\rangle = (\cos^2\theta e^{-iE_1 t} + \sin^2\theta e^{-iE_2 t})|\nu_\alpha\rangle - \cos\theta \sin\theta (e^{-iE_1} - e^{-iE_2 t})|\nu_\beta\rangle \quad (1.25)$$

Substituting the flavor-basis neutrino oscillation states back into the probability Equation (1.16) gives us Equation (1.31), which is the probability that neutrino oscillated into another flavor in the two-flavor case.

$$P_{\nu_\alpha \rightarrow \nu_\beta}(t) = |\langle \nu_\beta | \nu_\alpha(t) \rangle|^2 \quad (1.26)$$

$$= (\cos\theta \sin\theta)^2 (e^{-iE_2 t} - e^{-iE_1 t})(e^{iE_2} - e^{iE_1 t}) \quad (1.27)$$

$$= \left(\frac{\sin 2\theta}{2} \right)^2 (1 - e^{i(E_2 - E_1)t} - e^{-i(E_2 - E_1)t} + 1) \quad (1.28)$$

$$= \frac{\sin^2 2\theta}{4} (2 - 2\cos((E_2 - E_1)t)) \quad (1.29)$$

$$= \sin^2 2\theta \sin^2 \left(\frac{E_2 - E_1}{2} t \right) \quad (1.30)$$

$$\implies P_{\nu_\alpha \rightarrow \nu_\beta} = \sin^2 2\theta \sin^2 \left(\frac{\Delta m_{21}^2}{4E} L \right) \quad (1.31)$$

It will be useful to put this oscillation probability into a format that can be easily

referenced to determine what baseline we expect neutrino oscillations to occur over. Equation (1.32) gives the neutrino oscillation probability using SI units with length L expressed in kilometers, energy E in GeV, and the mass squared difference in units of electronvolts squared, eV², which is a convenient set of units for experimental applications, where these values are close to what would be physically realized at a reactor, collider experiment, or an experiment like SNO+.

$$P_{\nu_\alpha \rightarrow \nu_\beta} = \sin^2 2\theta \sin^2 \left(1.27 \frac{\Delta m^2 L [\text{eV}^2][\text{km}]}{E [\text{GeV}]} \right) \quad (1.32)$$

1.2.2 Neutrino Oscillations in Matter

So far we have discussed neutrinos traveling in a vacuum. However, in some cases, one needs to account for an extra potential in the neutrino propagation Hamiltonian, which is associated with the elastic forward scattering of propagating neutrinos off electrons and nucleons present in matter. Because we know neutrinos have some interactions with nucleons and electrons, this must be accounted for in our Hamiltonian formalism if they are traveling through matter. This usually goes by a name like the “matter effect” on neutrino oscillations, since it is an extra term in the Hamiltonian coming from the presence of matter along the propagation length of the neutrinos. As it turns out, the matter effect will not be important for the propagation of the neutrinos measured in this thesis. However, for the sake of completeness, we present a treatment of the matter effect on neutrino oscillations to explicitly show this is true.

To obtain these matter effects on neutrino oscillations, we need to account for flavor-specific interactions with matter through both charged current (CC) and neutral current (NC) interactions. Neutral current interactions between neutrinos and

Standard Model fermions occur through the exchange of a Z boson. For the case of propagation through terrestrial matter, the neutral current interaction will be with electrons and nucleons in the Earth. For these neutral current interactions all flavors of neutrinos couple equally to electrons and nucleons.

On the other hand, considering the charged current interactions for neutrinos moving through electrons, there is a difference in the matter potential V_e for electron neutrinos, as compared to muon and tau neutrinos moving through matter. Specifically, this difference in the matter effect potential for electron neutrinos versus muon or tau neutrinos [21] is given by $V_e - V_{\mu,\tau} \equiv V_{CC} = \pm \sqrt{2}G_F N_e$, where N_e is the electron density in matter and $G_F = 1.166 \times 10^{-5}$ GeV $^{-2}$ is the Fermi coupling constant. Therefore we must consider this difference in the potential for the propagation of electron versus muon neutrinos V_{CC} in our matter effect oscillation probability. The potential for neutral current interactions that apply to all the flavors is defined as $V_{NC} = \pm \frac{1}{2}\sqrt{2}G_F N_\alpha$. For both cases, V_{CC} and V_{NC} , the plus is for neutrinos and the minus sign is for antineutrinos.

The matter effect neutrino oscillation parameters that properly account for the difference in the Hamiltonian potential for electron versus non-electron neutrinos propagating through matter can be derived by accounting for the potential V_{CC} and appropriately modifying the resulting new oscillation parameters in terms of the already discussed vacuum ones. These matter effect equivalent parameters will be defined in this thesis as Δm_M^2 and $\sin^2 2\theta_M$ in terms of the vacuum oscillation parameters Δm^2 and $\sin^2 2\theta$. These parameters are given below in Equation (1.33) and

Equation (1.34) respectively,

$$\Delta m_M^2 \equiv \Delta m_{21}^2 \sqrt{\sin^2 2\theta + (\cos 2\theta - A_{CC})^2} \quad (1.33)$$

$$\sin^2 2\theta_M \equiv \frac{\sin^2 2\theta}{\sin^2 2\theta + (\cos 2\theta - A_{CC})^2}, \quad (1.34)$$

where additionally we define a charged current matter potential term

$$A_{CC} = -2\sqrt{2}G_F N_e E / \Delta m_{21}^2, \quad (1.35)$$

where the minus sign comes from these being antineutrinos. Then accounting for the matter effect alteration of neutrino propagation, using the above oscillation angle and mass splitting parameters, results in the following expression for neutrino oscillation probability in matter:

$$P_{\nu_\alpha \rightarrow \nu_\beta}^M = \sin^2 2\theta_M \sin^2 \left(\frac{\Delta m_M^2}{4E} L \right). \quad (1.36)$$

Now we will consider how the matter effect contribution given in Equation (1.34) would affect antineutrino oscillations. In the case that $|A_{CC}|$ is large, the effective mixing angle will become smaller, $\sin^2 2\theta_M \rightarrow 0$, indicating a small effective value for θ_M , which is different than the expected value of $\theta_{12} \approx 34^\circ$. This condition, where the effective mixing angle in matter is different than in free space is often called the Mikheyev-Smirnov-Wolfenstein (MSW) effect, which is another name for neutrino matter effect-induced oscillations. For this large mixing shift to occur the electron number density and antineutrino energy have to take certain values determined by Equations (1.33) and (1.34). In practice, the electron density varies through the

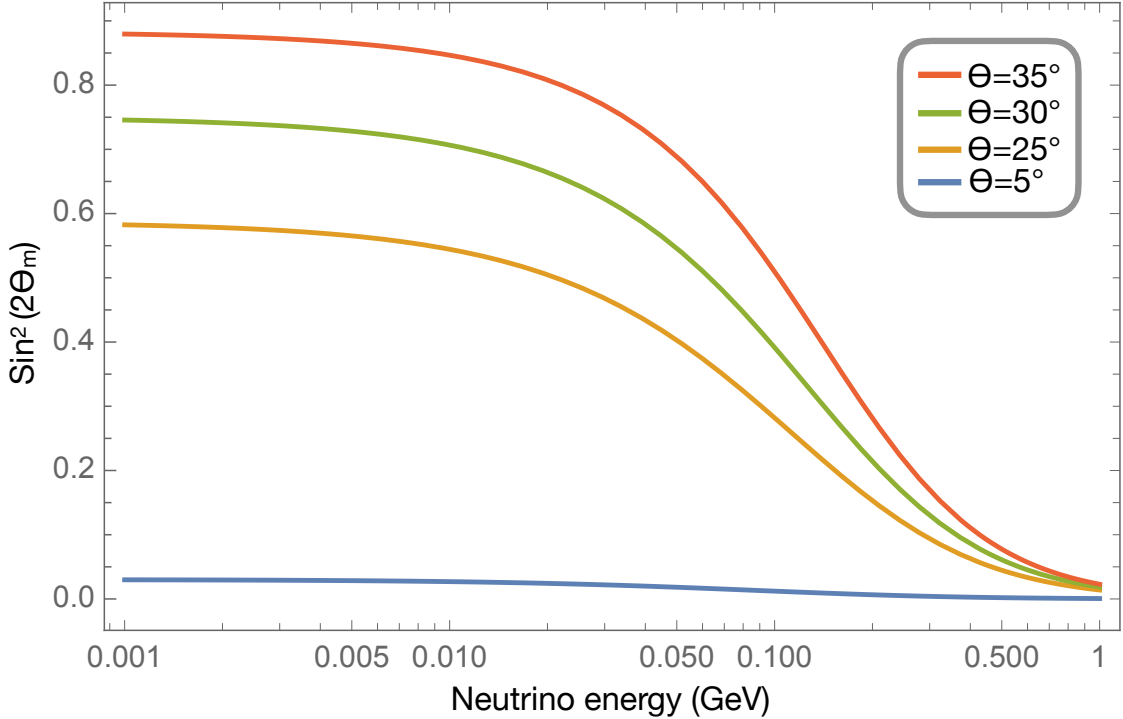


Figure 1.1: The effective mixing angle of a two neutrino oscillation framework, computed for propagation through Earth-like matter, where the effective mixing angle is given as a function of neutrino energy. A shift in the effective oscillation angle appears at energies of order 0.1 GeV or more, for a matter density of 3 g/cm³ and $\Delta m_{21}^2 = 7.5 \times 10^{-5}$ eV². For reference, the measured solar mixing angle is $\theta_{12} \approx 34^\circ$ [20]. In the text, we discuss that we do not expect to see very sizeable MSW-like effects for the neutrino energies considered in this thesis.

Earth and other astrophysical matter. For such a varying electron density, there is a corresponding variation in the effective mixing angle and energy at which the matter-effect causes noticeable matter mixing effects.

When measuring geoneutrinos and reactor neutrinos we can assume matter density to be around 3 g/cm², which is the average density of the Earth's crust [22]. Figure 1.1 shows the effective mixing angle versus the antineutrino energy for the average crust electron density. The matter effect mixing angle shifts substantially for neutrino

energies of the order of GeV, while the geoneutrino and reactor antineutrino are of the order of MeV, which has a much smaller apparent shift in mixing angle due to matter effects. Most of the measured geoneutrinos come from the crust, which is relatively near to the detector as will be discussed in Chapter 4. Using Eq. (1.36), we estimate that the matter effect shift in $\sin^2 2\theta_{12}$ from matter effects is $< 1\%$ for 2 MeV neutrinos and $< 2\%$ for 5 MeV neutrinos. This has also been investigated by Enomoto Sanshiro, who found the matter effect shifted the oscillation probability by less than about 2% in a dedicated study [23]. Because of this, we are making an assumption that matter effects will have a small contribution to the expected geoneutrino signal compared to the statistical uncertainties and geoneutrino geological prediction uncertainties and do not include them explicitly.

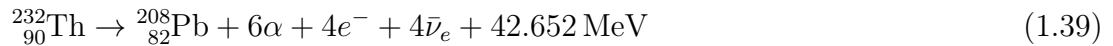
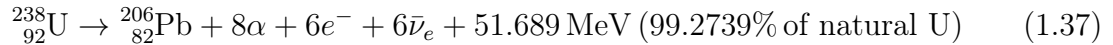
1.3 Geoneutrinos

The main topic of this thesis is the measurement of the geoneutrino flux at the SNO+ experiment. Geoneutrinos are electron antineutrinos, and in lesser abundance electron neutrinos, produced in radioactive beta decays naturally occurring in the Earth. The geoneutrinos that have been observed, and those that can be measured by SNO+ come from ^{232}Th and ^{238}U decay chains occurring in the Earth's crust and mantle. For example, uranium in the Earth's crust and mantle will decay into lead through a sequence of eight alpha and six beta decays and in the process produce six electron antineutrinos. These decay processes also each release a substantial amount of energy, which is transferred to the surrounding material in the Earth. The heat produced in the decay of radioactive isotopes in the Earth is called radiogenic heat.

Measuring the geoneutrino flux is useful for improving geological models for a

number of reasons. First, this measurement helps to place limits on the absolute abundance of U and Th, which in turn can provide insights into the radioactive isotopic composition of the planet, and provide an indirect probe of the depths of the Earth that are otherwise out of the reach of current geological surveys. In particular, there are three Bulk Silicate Earth models, called LowQ, MidQ, and HighQ, ordered by increasing abundance of U and Th, which geoneutrino measurements could discriminate between. A more detailed geological motivation is presented in Chapter 2. Thus far, all geoneutrino measurements have been carried out by using large detectors filled with liquid scintillators through inverse beta decay (IBD) interactions, where an electron antineutrino interacts with a proton to create a neutron and a positron.

The important processes that have a non-negligible contribution to the radiogenic heat, that also produce geoneutrinos, are listed below. These nuclear decay processes represent a sequence of uranium, thorium, and potassium decays down through a chain of isotopes to the final stable isotope shown, and the resulting yields of alpha, electrons, electron neutrinos, and electron antineutrinos.



The geoneutrino flux that can be measured at a liquid scintillator experiment like SNO+ is determined by the geoneutrino production spectra shown in Figure 1.2.

These spectra are normalized under the assumption that one of each of the listed isotopes decays fully down through its isotopic decay chain. In practice, the local abundance of each parent decay isotope must be modeled and integrated over the volume surrounding a detector, when predicting geoneutrino spectra. Using information obtained about the spatial distribution of geoneutrino emitting elements in the Earth, one can produce a geoneutrino flux energy spectrum and integrate over the volume of the Earth at a specific chosen detector location to get an expected spectrum at the location of the experiment. This will be discussed in more detail in Chapters 2 and 4.

The geoneutrino flux has been measured twice thus far, by the Borexino [25] and KamLand [26] experiments, located in Italy and Japan respectively. Neutrinos from ^{40}K have yet to be observed at any experiment since potassium geoneutrino energies are below the inverse beta decay threshold $E_{ibd} \approx 1.8$ MeV at liquid scintillator experiments. Inverse beta decay is currently the sole process by which geoneutrinos have been observed at liquid scintillator experiments.

The third measurement of the geoneutrino flux has been obtained at the SNO+ experiment, as presented in this thesis. This new measurement will begin to provide the additional geological data necessary for characterizing the abundance of uranium and thorium in the Earth. Notably, the SNO+ geoneutrino result is the first such measurement taken in North America. Eventually, with enough data accumulated, the measurement of geoneutrinos at SNO+ will also produce unique information that can be used to eventually determine the correct geological model for the abundance of radioactive isotopes, and by extension, the radiogenic heat budget of the Earth, in part because the geology around the Sudbury mine has been rather well characterized,

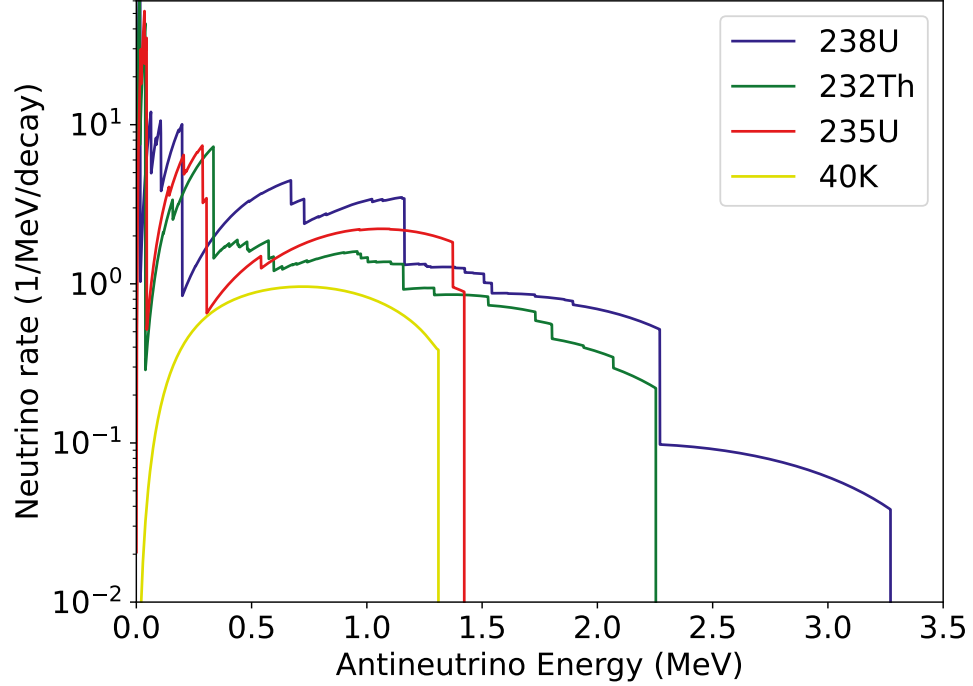


Figure 1.2: The geological antineutrino energy spectra are shown, for each relevant isotope. The isotope antineutrino production spectra plotted here are based on the isotopic spectral data computed in [24]. Uranium and thorium are the only radiogenic elements which have spectra that extend beyond the 1.8 MeV inverse beta decay threshold at liquid scintillator-based neutrino experiments.

as we will explain further in Chapter 4. At present, geoneutrino measurements at Borexino and Kamland experiments have been insufficient for discriminating between the different proposed radiogenic heat models for the Earth’s interior (LowQ, MidQ, HighQ). Further discussion of these models will be contained in Chapters 2 and 4, while further discussion of existing geoneutrino results will be contained in Chapter 7.

Chapter 2

Neutrino Geoscience Background and Motivation

This chapter details the importance of measuring neutrinos for determining certain geological properties of the Earth that are inaccessible to other methods. The discussion centers on the two major geological questions that neutrino measurements can weigh in on in the near future: the heat budget of the Earth and the refinement of the Bulk Silicate Earth Model.

2.1 Primordial and Radiogenic Heat in the Earth

The heat flow out of the Earth is an important geological data point, since this provides indirect information about the present-day physics and formative history of our planet. Geo-scientists have measured the total amount of heat flow at the surface of the Earth to be 46 ± 3 TW [27]. This measurement of the Earth's heat flow at the surface has been modeled by geologists as the outflow of all known interior heat sources. Primarily, it is assumed that these heat sources are the cooling of the mantle and core, which are still cooling after Earth's primordial formation process, and radiogenic heat, which comes from the radioactive decay of unstable isotopes inside the Earth. The radiogenic heat from the crust can be measured rather well

since samples can be extracted from the surface and to \sim kilometer-scale depths. The availability of crust samples and years of accumulated geological data allow for geoneutrinos produced in the crust to be accounted for in the analysis that follows. However, it is very hard to sample deeper layers of crust or take direct samples from the mantle, although there have been futuristic proposals to this end [28]. Therefore, the exact amount of radioactive elements contained within layers of the Earth deeper than a few kilometers is still unknown.

Before discussing the primordial component of heat flowing from the Earth, it will be useful to note that the science of planetary formation is an active and rapidly evolving field [29]. As a consequence, models of the amount of primordial heat remaining after the formation of planets, including small rocky Earth-like planets, have large uncertainty [30, 31, 32]. Furthermore, as could be guessed from the discussion above about the absence of deep geological samples, there is no direct information on how the sub-crustal layers of the Earth evolved in temperature over geologic timescales. Without much data to work with, the existing models for planetary formation are varied and there are significant disagreements between them about the amount of primordial heat that remains [33, 34, 32]. This means that probably the best strategy moving forward is to accurately measure the radiogenic heat, and then from this determine what proportion of heat flowing out of the Earth is primordial. In order to measure the total radiogenic heat, we will need to understand the absolute abundances and distributions of all radiogenic heat-producing elements rather well.

Because models predicting a certain current amount of primordial heat are intertwined with geological models of the deep interior of the Earth, since these affect each

other, it is useful to turn to a specific Earth model framework to clarify the relationship between primordial heat, radiogenic element abundances, and specific geological models.

2.2 Bulk Silicate Earth Models

Building an accurate model of the composition of the Earth’s interior is an ongoing endeavor. Currently, the most popular class of Earth models are the Bulk Silicate Earth Models (BSE) [35], which are a generalized framework for specifying the Earth’s composition, subject to a few well-motivated geological assumptions about the bulk distribution of certain elements in the Earth. Bulk Silicate Earth models classify elemental compositions by simplifying the Earth into two main portions as seen in Figure 2.1. These two portions are firstly the crust plus mantle, which comprises the “Bulk Silicate Earth” portion, and secondly, a portion that is simply the core of the Earth referred to as the “core.” For the sake of clarity in the following geological discussion, it is important to emphasize that the Bulk Silicate Earth models derive their name from the outer portion of the Earth (the crust and mantle), which itself is called the “Bulk Silicate Earth.” BSE models treat this portion as a largely monolithic quantity, which is the origin of the BSE model name.

The outer portion of the Earth in BSE models called the Bulk Silicate Earth layer, is dominated by so-called lithophile (rock) elements, which include calcium (Ca), aluminum (Al), potassium (K), thorium (Th), and uranium (U), while the core composition is predominantly siderophile (*i.e.* metallic) elements, such as iron (Fe), nickel (Ni), cobalt (Co), phosphorous (P), and gold (Au). The names lithophile and siderophile are part of the Goldschmidt classification of elements proposed in the

1930s [36]. *Lithophile* elements have chemical properties that allow them to easily combine with oxygen, which generally prevents them from sinking down into the Earth's core. This can be compared to *siderophile* elements which combine readily with heavy metals like iron and therefore more rapidly settle into the core of the Earth.

- Siderophile (S) - The metals near iron in the periodic table that exhibit metallic bonding. These are expected to sink to the Earth's core.
- Lithophile (L) - Elements that form ionic bonds (generally have filled outer electron shells). They typically bond to oxygen in silicates and oxides. Since they bind to lighter elements, siderophiles are expected in the upper Earth, the mantle and the crust.

For the purposes of this thesis, the main takeaway from Bulk Silicate Earth models is that there is an expectation of negligible amounts of K, Th, and U in the metallic core because these elements have been determined to not combine with metal alloys at high pressure and temperature (they do not tend to dissolve in metal), so they will not tend to sink like siderophile elements into the core of the Earth.

Bulk Silicate Earth models can be further generalized into three categories, which for our purposes classify neatly into a low (LowQ), medium (MidQ), and high (HighQ) amount of heat production, corresponding to the amount of radiogenic heat each model is expected to produce. We will return to these shortly. First, it would be useful to discuss the motivation for BSE models, and how they have been devised. The way Bulk Silicate Earth models are made is by extrapolating from assumptions about the primordial minerals that formed the Earth and then attempting to account for the evolution of these minerals using geophysical dynamics and geochemistry

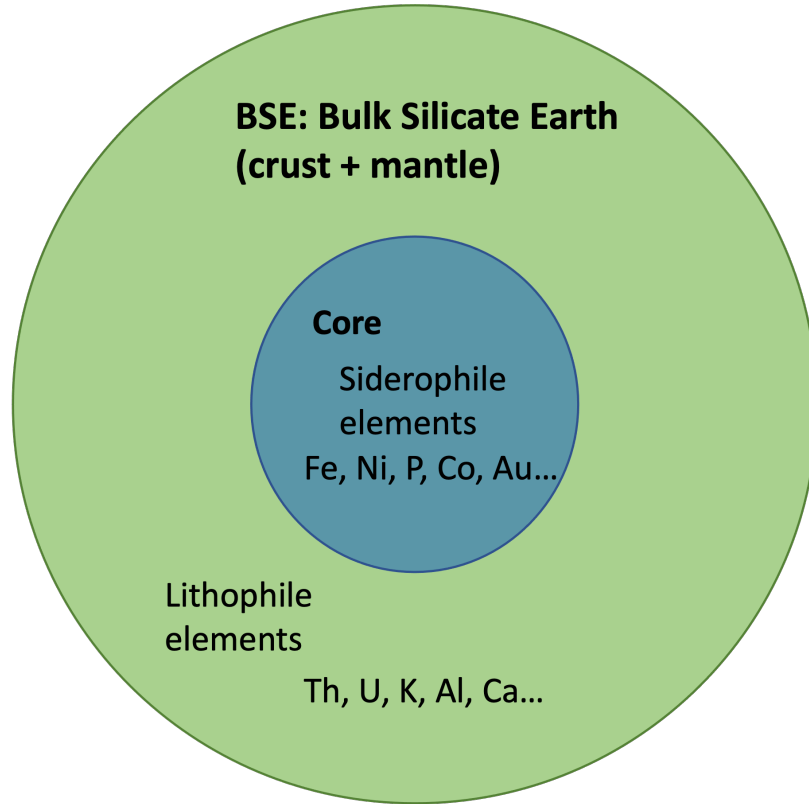


Figure 2.1: A simplified illustration of Bulk Silicate Earth (BSE) models, where the Earth is classified by the dominance of Lithophile (“rocky”) elements in its crust and mantle and siderophile (“metallic”) elements in its core. Of importance to this thesis, the Lithophile elements include the radiogenic elements thorium, uranium, potassium, which can be used to test models of the abundance and distribution of Lithophile elements in the Earth.

measurements. To that end, understanding the initial abundance of elements that formed the Earth is especially important. This is achieved by examining the meteorite composition, which we now briefly discuss.

Chondritic meteorites are meteorites that have been found, which are composed of a mixture of silicate and metal materials in proportions similar to that found on the Earth. The most primitive of the chondritic meteorites is the C1 carbonaceous (carbon-rich classification) chondrite [37]. It has actually been shown using solar

spectra, that the composition of chondritic meteorites matches the composition of the solar photosphere, *i.e.* the outer surface of the sun. Figure 2.2 shows the elemental abundances of the solar photosphere versus the log elemental abundances of the C1 Chondrites.

Examining Figure 2.2 a clear match to C1 chondrite elemental abundances is visible, with a few exceptions including noble gasses lying above the trend, due to the solar photosphere being enriched with non-reactive noble gasses, as well as lithium being underneath the trend due to the solar fusion consuming most of the lithium within the sun [37]. The Sun accounts for about 99% of the mass of the solar system, supporting the assumption that the composition of the primordial solar nebula, from which all of the Solar System bodies were formed, is approximately the same as the composition of the sun. This in turn provides guidance as to the correct initial elemental abundances we should assume were present during the formation of our terrestrial planet. Speaking more generally, the comparison shown in Figure 2.2 deserves further attention, since spectroscopy measurements of trace elements in the solar photosphere are still being improved, with meteorite samples providing an important cross-check, as we sharpen our understanding of primordial elemental abundances present at the formation of our Solar System.

Now that we have described what is known about the building blocks from which our planet was formed, it is important to understand the difference between refractory and volatile elements, and the geochemical evolution of the Earth's formation. This is summarized in Figure 2.3 showing the elemental abundances versus their condensation temperatures. The condensation temperature of the element, along with its detailed chemical interactions with other elements, combined further with geological

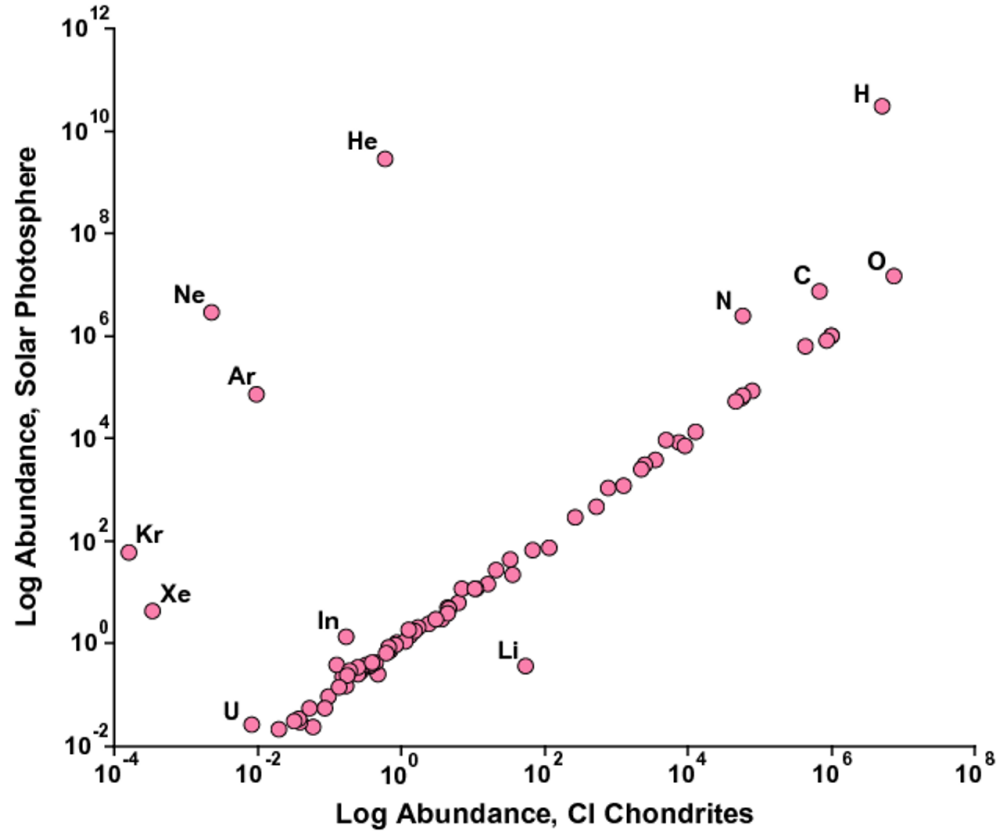


Figure 2.2: Log elemental abundances of the solar photosphere, measured using spectroscopic methods, versus the log element abundances of the C1 Chondrites, taken from [37]. These solar photosphere spectra are enriched in non-volatile noble gasses, which have abundances that are elevated above the visible trend. The spectra are comparatively underabundant in lithium, since it is consumed by Lithium fusion processes in the solar core, leading to a Lithium abundance lying below the general trend. The most important takeaway is that C1 Chondrite meteorites appear to provide a good model for the likely geological composition of bodies formed during the primordial formation of our Solar System.

processes that themselves can respond to geochemistry, all determine how the elements will cluster inside the Earth. In Figure 2.3, the y-axis shows relative elemental abundances normalized to the C1 carbonaceous chondrites, which serve as a reasonable approximation of the absolute initial abundances, since the actual abundance values are not precisely known. In Figure 2.3 the top x-axis shows the condensation temperature in Kelvin and the bottom shows condensation pressure in MegaPascals. These two values represent the pressure and condensation temperature at which 50% of the abundance of the element is condensed from a vapor to a solid phase.

Figure 2.3 can be interpreted as showing under what conditions the primordial elements start crystallizing out of the solar nebula and begin forming a rocky planet, and which elements tend to remain near the surface (and which sink to the core) after this occurs. Thus the final abundances measured at the Earth's surface will depend on how readily the elements condensed during the Earth's formation, and whether they later settled into the core of the Earth. A clear separation between the lithophile and siderophile elements is apparent (and expected). As a subcategory of the lithophile elements, the refractory elements are elements that condensed out of a nebular disk at high temperatures and empirically are observed in equal ratios in most rock samples (shown in blue in the upper left of the plot). The abundance of siderophile elements (green) are affected by the formation of the core, which is to say, they tend to settle into the core and are therefore underabundant at the surface of the Earth, as shown in Figure 2.3. It should also be noted that siderophile elements have an abundance that can vary markedly in different meteorite samples [37].

Generally the lithophile elements (shown in blue) are more abundant, as expected from their chemical properties which makes them tend to stay near the surface of the

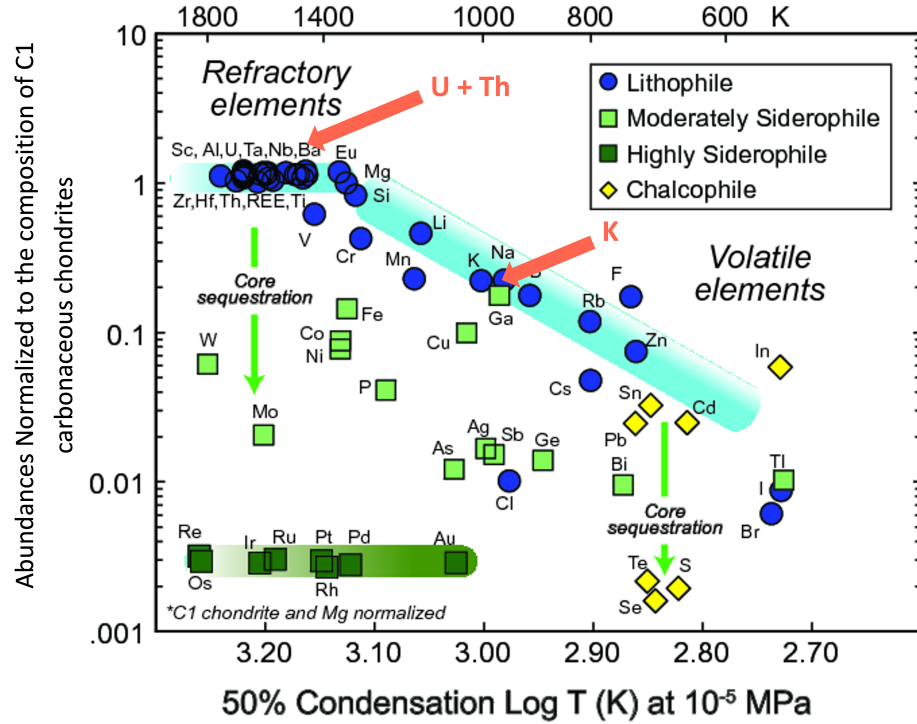


Figure 2.3: The elemental abundance of silicate Earth as measured from a variety of samples [38], versus each isotope's 50% condensation temperature and pressure. Figure as modified from [37]. Here the y-axis shows the relative element abundances as normalized to the C1 carbonaceous chondrites, which are meteorites that have elemental abundances that match primordial proportions. The top x-axis shows the temperature in K and the bottom x-axis shows pressure in MPa. These two values show the pressure and condensation temperature at which 50% of the abundance of each depicted element is condensed from a vapor to a solid phase. It can be seen that lithophile elements are much more abundant than siderophile, as discussed in the text. The chalcophile elements depicted in this figure are not otherwise discussed in this thesis. With some exceptions they are rare and tend to remain near the Earth's surface (via readily reacting with sulfur and “chalcogens”).

Earth. However, we can see a decrease in the abundance of the lithophile elements, especially for those with a lower condensation temperature, which are called volatile elements. Volatile elements show elemental abundance variation due to a more acute sensitivity to condensation temperature. It is an open question whether the slope of the volatile elements in Figure 2.3 is as shown for the bulk of the Bulk Silicate Model region, including the mantle, or whether the volatile elemental abundance will have a different slope than measured at the surface of the Earth. Certainly, the slope of volatile elemental abundances varies across different chondrite (meteorite) samples, as shown in Figure 2.4.

This presents a special opportunity for geoneutrino analyses: if we can establish the absolute abundance of thorium and uranium in the planet, we can use chondritic ratios of refractory elements to set their abundances and from that model the remaining abundances of the other elements. Furthermore, if we could determine the absolute abundance of potassium, a moderately volatile element in the Earth, we would have a first measurement of the possible slope of the volatile elemental abundances for the interior of Earth.

With our preliminary discussion of Bulk Silicate Earth Models complete, we now turn to the simplified BSE models that may be discriminated between using geoneutrino measurements. These models essentially suppose there are different amounts of refractory elements, using either evidence in the form of analogue mineral measurements, arguments about the early planetary dynamics of lithophile elements, or arguments concerning the supposed heat flow present in the mantle from indirect measurements.

1. The LowQ model for the Bulk Silicate Earth predicts the radiogenic heat to

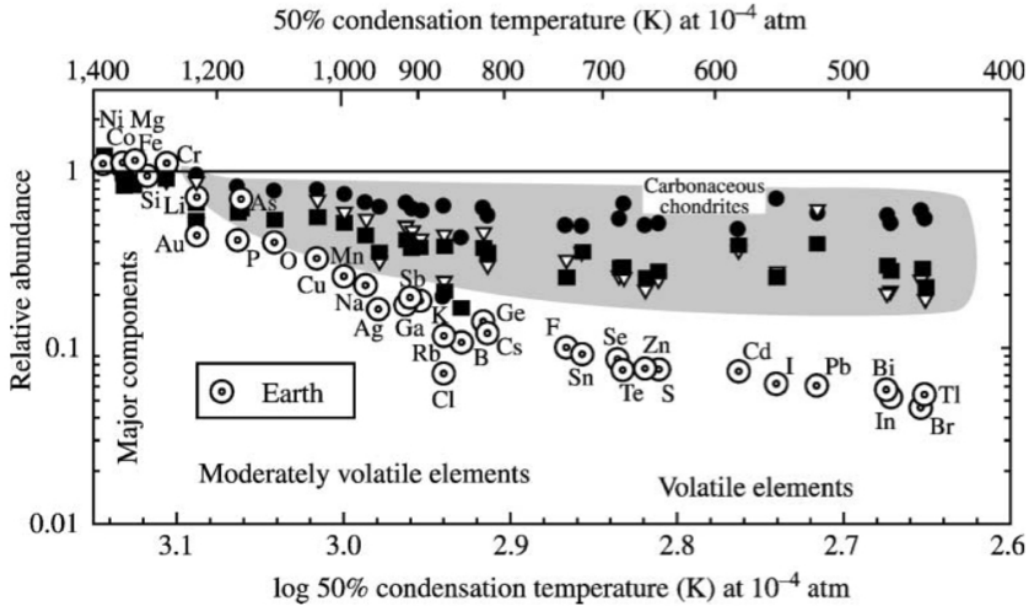


Figure 2.4: The elemental abundance of refractory elements for silicate Earth (dotted circles), as compared to the abundance of refractory elements in a variety of different chondrite meteorite samples (solid filled shapes). Figure adapted from [38]. The distribution trends for the volatile elements shown to the right can be usefully compared to Figure 2.3, which only shows volatile elemental abundance measurements for silicate Earth. Future observations including geoneutrino measurements, will help determine the actual abundance of the volatile elements in the deep crust and mantle of the Earth.

be ≈ 10 TW, and is primarily derived from the observation of isotopic similarities between Earth and enstatite chondrite [39], which altogether suggests a relatively low abundance of refractory elements. On the other hand, the LowQ model is also supported by early collisional erosion models with the assumption of a non-chondritic Earth [40].

2. The MidQ models for Bulk Silicate Earth, which predict around ≈ 20 TW of radiogenic heat, are the result of combining observations of chondrites and

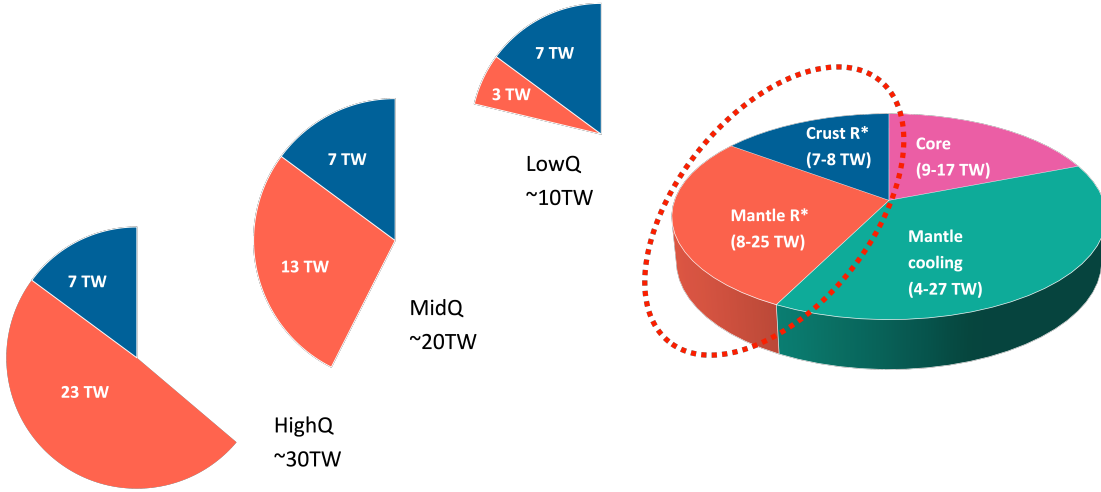


Figure 2.5: This pie chart illustration shows the relative proportions of the heat produced in the mantle (orange) and the crust (blue) for each of Bulk Silicate Models indicated. The complete pie chart shows the relative pie slice proportions using the MidQ model (Wipperfurther et al. (2019) [43], McDonough & Sun (1995) [41]). However, the range in heat flux (given in TW) as shown in this largest pie includes the range of allowed values for all three models, LowQ, MidQ, and HighQ. The red dashed line denotes the radiogenic portion of the Earth’s heat budget, which can be measured using geoneutrinos.

terrestrial sample mantle melting trends [41].

3. Finally, the HighQ models are drawn from mantle convection model parameters [42], which indicate that perhaps the mantle has a high amount of heat, presumably coming from a large amount of refractory elements and by extension radiogenic elements, in an abundance larger than might be supposed from a simple comparison to chondrite abundances, resulting in a prediction for radiogenic heat of ≈ 30 TW.

The three BSE models we have introduced are illustrated using pie charts in Figure 2.5, which show the relative proportions of the heat production in the mantle

(orange) and the crust (blue) for each of the LowQ, MidQ, and HighQ Bulk Silicate Earth models. The large pie chart on the right shows the relative proportions using the MidQ model (Wipperfurth et al. (2019) [43] McDonough & Sun (1995) [41]), in terms of the proportions of the pie. However, in the largest pie, the range in Terrawatts that is given inside each pie slice spans all model values (from LowQ to HighQ). The red dashed line denotes the radiogenic portion of the Earth’s heat budget, which can be measured using geoneutrinos. The measurement of the radiogenic heat could improve the understanding of the amount of energy available for mantle convection, plate tectonics, and geodynamo as well as provide constraints on the relative absolute abundances of the other refractory elements [44].

We have seen that even a relatively simple model of the Earth’s interior, like the Bulk Silicate Earth Model, carries substantial uncertainty regarding the variation of elemental abundances that could be found. To begin sorting out the correct model, we will require additional data from new detectors. We now turn to a summary of the SNO+ detector at SNOLAB, which we will use in this thesis to make the third measurement of geoneutrinos.

Chapter 3

The SNO+ experiment and antineutrino detection

In this chapter, we introduce the SNO+ experiment and provide some details on the physics and software underpinning the detection of radiogenic electron antineutrinos at SNO+, which is the main focus of this thesis.

3.1 The SNO+ Experiment

The SNO+ experiment is a multipurpose large-scale liquid scintillator detector located in SNOLAB, a 2070m underground, 10000 square ft, Class-2000 clean room in Vale's Creighton mine near Sudbury, Ontario, Canada [45]. The main objective of SNO+ is to search for neutrinoless double beta decay ($0\nu\beta\beta$) in the decay of tellurium, in order to determine if neutrinos are Majorana or Dirac particles and to gain knowledge about the absolute mass of the neutrino. Other topics of interest are reactor neutrino oscillations, supernova neutrinos, geo-neutrinos, solar neutrinos, and some exotic searches, including dark matter and nucleon decay. Even though the main focus of the experiment has been to search for neutrinoless double beta decay, SNO+ has been operating in several phases, which have a variety of physics goals [46]:

3.1.1 Water Phase

The first SNO+ phase was the water phase, running from May 2017 to October 2018. In this phase, the Acrylic Vessel (AV) was filled with 905 tonnes of Ultra Pure Water (UPW). Besides the commissioning of updated electronics and data acquisition (DAQ) systems, the phase also saw the completion of two major physics analyses. First, there was a measurement of ${}^8\text{B}$ solar neutrino flux with very low backgrounds [47]. Secondly, SNO+ data was able to set some new limits on invisible modes of nucleon decay in water [48]. This phase was also rather useful for understanding and measuring the radiation produced by the hold-down and hold-up ropes, AV, and external water, which could then be carried forward to improve the understanding of the backgrounds in the following phases.

3.1.2 Partial Fill Phase

After the water phase was completed the process of replacing water in the Acrylic Vessel with liquid scintillator (LS) began. The SNO+ liquid scintillator cocktail is comprised of liquid alkylbenzene (LAB) as a solvent and 2,5-diphenyloxazole (PPO) as a primary fluor. The filling process was intended to run continuously so that the phase of full scintillator fill could begin as soon as possible. However, the process of scintillator fill was interrupted by the COVID-19 pandemic. All scintillator fill activities were stopped for seven months between March 2020 and October 2020. This left the detector with 365 tonnes of scintillator floating on top of 480 tonnes of ultra-pure water as can be seen in figure 3.1. The interface was located at approximately the $z = 0.75\text{m}$ position, where $(x, y, z) = (0, 0, 0)$ is the center of the Acrylic Vessel. This clean separation between the two fluids was the result of a difference in density

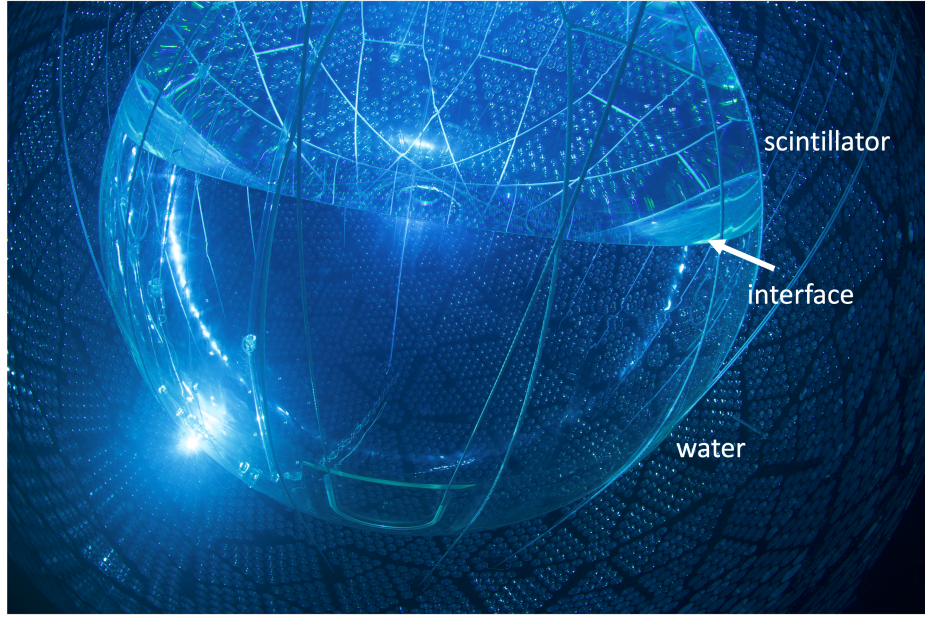


Figure 3.1: A photo of the SNO+ detector during the partial fill. The interface between water and scintillator is noted with the arrow, where the less dense liquid scintillator floated atop the water. While unexpected, this partial-fill phase permitted a number of useful physics analyses.

since LAB has a density of 0.865 g/cm^3 at 13° C temperature, which is the average temperature of the SNO+ cavity during the scintillator phases, as compared to the usual density of water which is 1 g/cm^3 . The scintillator deployment also included the addition of 2,5-diphenyloxazole (PPO) as a fluor into the scintillator mix, with the original concentration of the partial fill being 0.6 g/L . The configuration of liquid scintillator floating atop water was quite stable, allowing for a number of unique physics analyses to be carried out, and thus providing SNO+ with an unexpected phase of the experiment.

During the partial-fill phase, reactor antineutrino oscillation analyses were performed, and SNO+ is currently in the process of submitting a paper to publish these results. Given the geoneutrino-focus of this thesis, we will note here for completeness

that while detecting geoneutrinos in the partial fill phase would have been possible in principle, the expected signal for the timescale and volume of scintillator would produce a small number of geoneutrino events compared to backgrounds, and so would not have provided enough statistics for a robust analysis.

However, preparation for the geoneutrino analysis was undertaken during the partial fill phase, by checking the validity of coincidence and background tagging procedures on partial fill data, and comparing these to the same procedures followed by the reactor analyses that were mentioned above. Some scientists also took the opportunity to refine their analysis techniques to determine important backgrounds in preparation for the $0\nu\beta\beta$ search. An interesting analysis was completed by Josie Paton on the preservation of directional information in liquid scintillator neutrino events. Normally, it is nearly impossible to reconstruct the directionality of neutrinos interacting in a scintillator volume. However, during the partial fill phase, it was possible to obtain directional information for ^8B solar events, due to the stable period of data acquisition at a lower concentration of PPO of 0.6g/L , rather than the target 2.2g/L . This lower concentration period created a slower scintillation profile. Directional Cherenkov light was separated from the slower isotropic scintillation light using time-based profiling. Collaborator Josephine Paton presented the first reconstruction of event-by-event direction in a high-light yield large-scale liquid scintillator detector [49].

3.1.3 Scintillator Phase

Currently, SNO+ is in the liquid scintillator(LS) phase. The fill was completed in April 2021 with 790t of LS. For the period of April 2021 to June 2021, the LS concentration of added PPO was at a lower concentration of 0.6g/L . Data collected during this time was mainly used to verify optical parameters by performing optical calibrations, including validation of predicted light yield and timing. In addition, background measurements were performed during this time period, including more calibration and background measurement work in preparation for tellurium and other planned measurements. In April 2022 the target concentration of PPO of 2.2g/L in the liquid scintillator mix was achieved. At present, the scintillator phase has several ongoing analyses, including the measurement of the ${}^8\text{B}$ solar neutrino flux, a new measurement of reactor antineutrino oscillation parameters, the detection of any galactic supernovae that may go off, and of course, the geoneutrino analysis presented here. For the purpose of the present thesis, all the discussed data comes from the full fill liquid scintillator phase with 2.2g/L PPO in LAB concentration.

3.1.4 Tellurium Loaded Phase

The final major phase of the SNO+ experiment will be the tellurium-loaded phase. During this phase, the search for $0\nu\beta\beta$ will be performed. The natural tellurium will be added to the liquid scintillator by recirculating the existing scintillator from the AV through a tellurium processing plant. ${}^{130}\text{Te}$ is particularly suited to the task due to its high natural abundance and long $2\nu\beta\beta$ half-life [46]. The pure scintillator phase will also be used to sharpen the understanding of backgrounds (for example the alpha-n background discussed in Chapter 5) that will impact the $0\nu\beta\beta$ region of

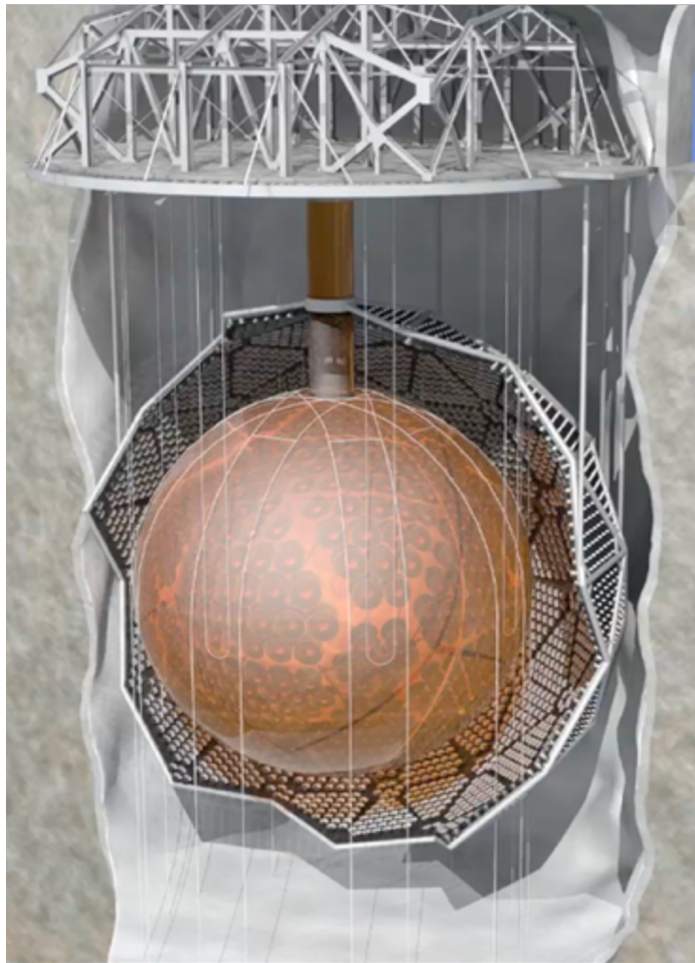


Figure 3.2: Illustration of the SNO+ detector [46]. The hold-down and hold-up ropes are visible, securing the Acrylic Vessel in a structure surrounded by photomultiplier tubes arranged in triangular and hexagonal formations on a photomultiplier tube support structure. The PMTs and associated concentrators cover about 54% of the solid angle surrounding the acrylic vessel. External to the acrylic vessel, a volume of water acts as shielding as an external muon veto.

interest during the tellurium phase.

3.2 Detector

Figure 3.2 shows an illustration of the SNO+ detector. The detector is located within a thirty meter tall cavity. The cavity is filled with 7000 tonnes of ultra-pure water (UPW), which adds shielding from external radiation and acts as a volume for a muon veto. The detector uses a twelve meter diameter and 5.5 cm thick Acrylic Vessel, which is filled with a liquid scintillator. The scintillation light is detected by ≈ 9400 8-inch Hammamatsu R1408 photomultiplier tubes (PMTs) located on the PMT support structure (PSUP) surrounding the AV. The PMT's photocathode area coverage is about 54% of the solid angle of the target volume. There is also an array of PMTs facing outward from the target volume called OWLs (OutWard Looking PMTs). These detect events that happen outside the PSUP and provide a means to veto incoming muons. The low cosmic muon background rate of $0.286 \pm 0.009 \text{ m}^{-2}\text{day}^{-1}$ [46], due to the lab's location deep underground in the Sudbury mine, is a huge benefit. Figure 3.3 shows the comparison of the expected cosmic muon rate at different lab locations.

Turning back to the SNO+ detector, for the purpose of calibrations, the AV can be accessed through its neck. The neck is about seven meters high and can be accessed from the deck clean room (DCR). The whole of the water and scintillator volumes are additionally covered by a cover gas system. The very top area of the cavity has high-purity nitrogen gas circulating above the water. The area of the neck above the scintillator additionally has a layer of sealed nitrogen gas, where this volume of gas is constantly monitored for radon contamination.

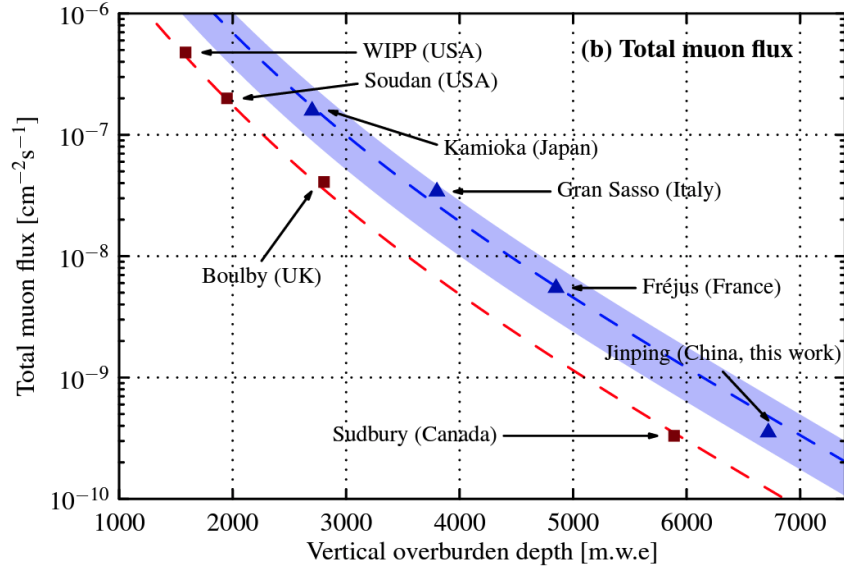


Figure 3.3: Muon flux versus the depth of various underground experimental labs, given in meters of water equivalent [50]. The red and blue dashed lines represent different modeling approaches. The red dashed line is from an empirical formula for the muon flux for sites located directly underground, or “down a mineshaft.” The blue dashed line and shaded region represent the fit result from a GEANT4 model of the muon flux for sites underneath mountains. In this case, less rock shielding at shallow angles leads to more muon flux, compared to using the empirical formula appropriate for down mineshaft sites.

3.3 Antineutrino Detection

We turn to the detection of antineutrinos at the SNO+ experiment. Electron antineutrinos are detected through the so-called “Inverse Beta Decay” (IBD) interaction, as depicted in Figure 3.4:



In short, an electron antineutrino interacts with a proton to create a neutron and positron.

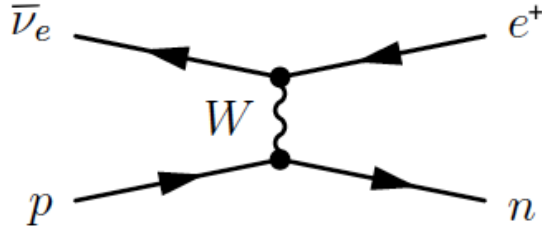


Figure 3.4: The Feynman diagram for the Inverse Beta Decay (IBD) reaction, where an electron antineutrino exchanges a W boson with a proton, thereby converting the proton into a neutron, and converting the electron antineutrino into a positron.

Inside the detector, the resulting particles are detected through their nuclear interactions with hydrogen (in the case of the neutron), and their annihilation with electrons (in the case of the positron). This is depicted in more detail in Figure 3.5, which shows an incoming antineutrino interacting with a proton, thereby creating a positron and a neutron. The positron will rather quickly (over timescales of a few nanoseconds) annihilate with an electron in the liquid scintillator volume, creating two 0.511 MeV gamma rays in a prompt flash of light, which alongside with the deposited kinetic energy is known as the prompt signal in antineutrino detection. The neutron undergoes a thermalization process for about 200 microseconds and then gets captured by a nucleus (most commonly hydrogen or carbon in a scintillator), which creates a delayed light signal of around 2.2 MeV after capturing on hydrogen. By observing the coincidence of prompt and delayed events, and using appropriate energy and timing cuts, we can count the number of electron antineutrino candidates that interact with the SNO+ volume. We define the time separation between the prompt and delayed events using the fit time of each event, as determined by SNO+ data analysis software, reviewed in Section 3.4. The timing difference between the prompt

and delayed events is defined in this thesis as $\Delta T = t_d - t_p$, this will be discussed in great detail in Chapter 6.

Measuring the prompt scintillation light from the positron kinetic energy gives us a good estimate of the incident antineutrino energy. In more detail, the antineutrino energy can be reconstructed from the deposition of energy by the positron, followed by the positron/electron annihilation energy. We can define the prompt energy of the reaction as

$$E_{prompt} = T_{e^+} + 2m_e \quad (3.2)$$

where T_{e^+} is the positron kinetic energy, m_e is the electron mass. Then from the energy conservation we have

$$E_{\bar{\nu}_e} + M_p = T_{e^+} + m_e + M_n + T_n \quad (3.3)$$

here M_n is the neutron mass, M_p is the proton mass, and T_n is the neutron kinetic energy. We can ignore the neutron's kinetic energy here because most of the antineutrino kinetic energy is distributed to the positron, due to its small mass relative to the neutron, and momentum conservation. As a result, the neutron recoil energy in this case is on average only a few tens of keV. Therefore from the equation (3.2) and (3.3), we get

$$E_{\bar{\nu}_e} = E_{prompt} + (M_n - M_p) - m_e \simeq E_{prompt} + 0.78 \text{ MeV} \quad (3.4)$$

The energy released in the delayed neutron capture is determined by the mass difference between the final ${}^2\text{H}$ nucleus and the initial masses of proton and neutron, resulting in all neutron captures on free protons emitting 2.2 MeV γ . The importance

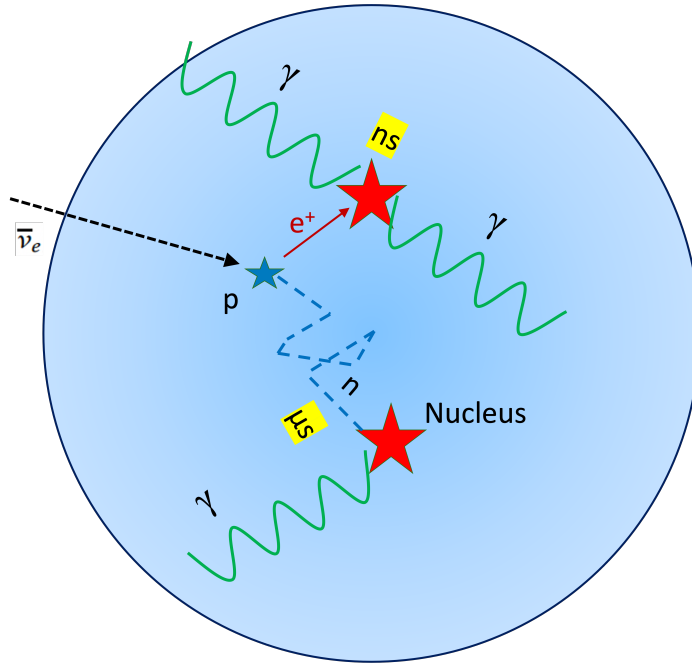


Figure 3.5: Illustration of an electron antineutrino detection inside a scintillator detector. The electron antineutrino interacts with a proton producing a positron and a neutron. The positron energy deposition and annihilation produce light, while the neutron thermalizes and gets captured by a nucleus which results in the emission of a 2.2 MeV γ and provides the visible light for the delayed event.

of having a prompt and delayed scintillation event for detecting electron antineutrinos cannot be overstated: this type of delayed coincidence allows for extremely efficient rejection of most backgrounds, which do not have the delayed coincidence signal. It must also be noted that equation (3.4) is a simplified version of energy reconstruction, the full 4-momentum conservation calculations are performed by the SNO+ RAT software energy fitters when reconstructing the energy of the event.

For the inverse beta decay reaction to occur the incoming antineutrino has to have sufficient energy to convert the proton to a neutron, and create a positron. The threshold for this interaction in liquid scintillator is around 1.8 MeV. A simple energy

conservation analysis, which applies to all particle interactions, allows us to obtain the threshold energy for the inverse beta decay interaction. This threshold energy corresponds to the mass difference between initial and final particles in a lab frame as shown in equation (3.5). Here E_{th} is the threshold energy, M_n is the neutron mass, M_p is the proton mass, m_e is the electron mass.

$$E_{th} = \frac{(M_n + m_e)^2 - M_p^2}{2M_p} = 1.806 \text{ MeV} \quad (3.5)$$

3.3.1 IBD Cross Section

It will be useful to examine the inverse beta decay cross-section, and compare this to the electron antineutrino flux from uranium and thorium isotopes.

The cross-section for electron antineutrino-induced inverse beta decay as depicted in Figure 3.4 is given by [51]

$$\sigma_{IBD}(E_{\bar{\nu}_e}) = 9.52 \times 10^{-44} \text{ cm}^2 \times (E_{\bar{\nu}_e} - E_{th} + m_e)^2 \left[1 - \frac{m_e}{(E_{\bar{\nu}_e} - E_{th} + m_e)^2} \right]^{1/2}, \quad (3.6)$$

where the units of energy are in MeV, and which has an energy dependence that cuts off the interactions sharply around the threshold energy of 1.8 MeV. In Figure 3.6, we have plotted this cross-section alongside the production rates of radiogenic antineutrinos. From this it is apparent that the IBD process cannot be used to detect antineutrinos produced from potassium.

3.4 Event Simulation and Analysis Software

We turn to a discussion of the analysis framework that SNO+ uses to analyze detector data. The SNO+ collaboration uses the Reactor Analysis Tool (RAT) [52],

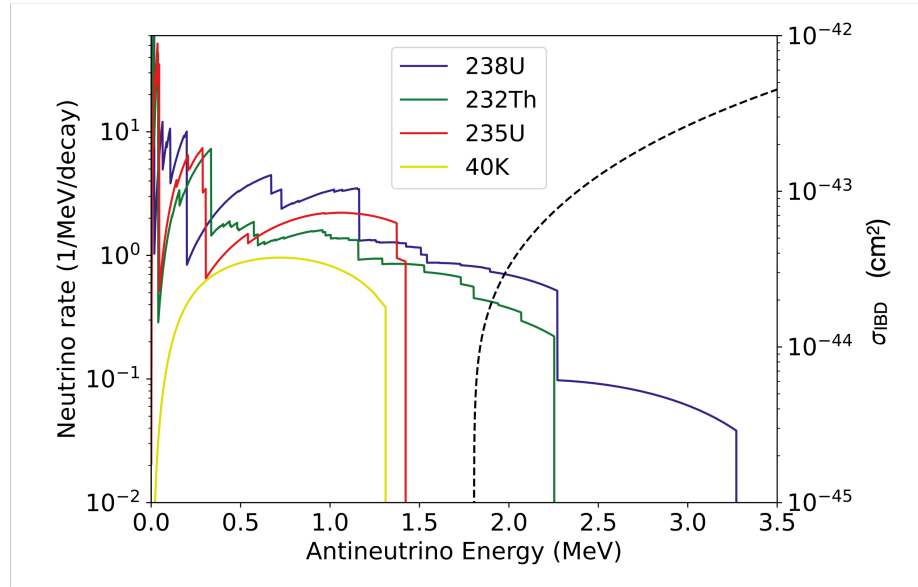


Figure 3.6: The rate for antineutrino production by labeled elements (solid lines) are shown on the left-side y-axis, as in Figure 1.2. Here this can be usefully compared to the cross-section for inverse beta decay given in Equation (3.6), shown on right-side y-axis (dashed line). It can be seen that the cross-section for IBD drops sharply around the IBD threshold of $E_{th} = 1.806$ MeV.

which combines Monte Carlo (MC) simulations with event-based analysis tasks, built specifically for the analysis needs of experiments like SNO+. RAT is written in C++ and the Monte Carlo portion simulating particle interactions inside the detector is based on GEANT-4 software [53]. The SNO+ RAT framework has evolved over the years and was adapted to perform exactly to SNO+ experiment specifications [46]. It contains the custom particle generators, and calculations for particle propagation in the SNO+ scintillator, including reflections, absorption, and scattering depending on SNO+ geometry. SNO+ RAT is also able to call run-by-run information of the detector conditions, such as the state of electronics and the data acquisition system (DAQ) response, which improves the accuracy of the simulation of the detector for

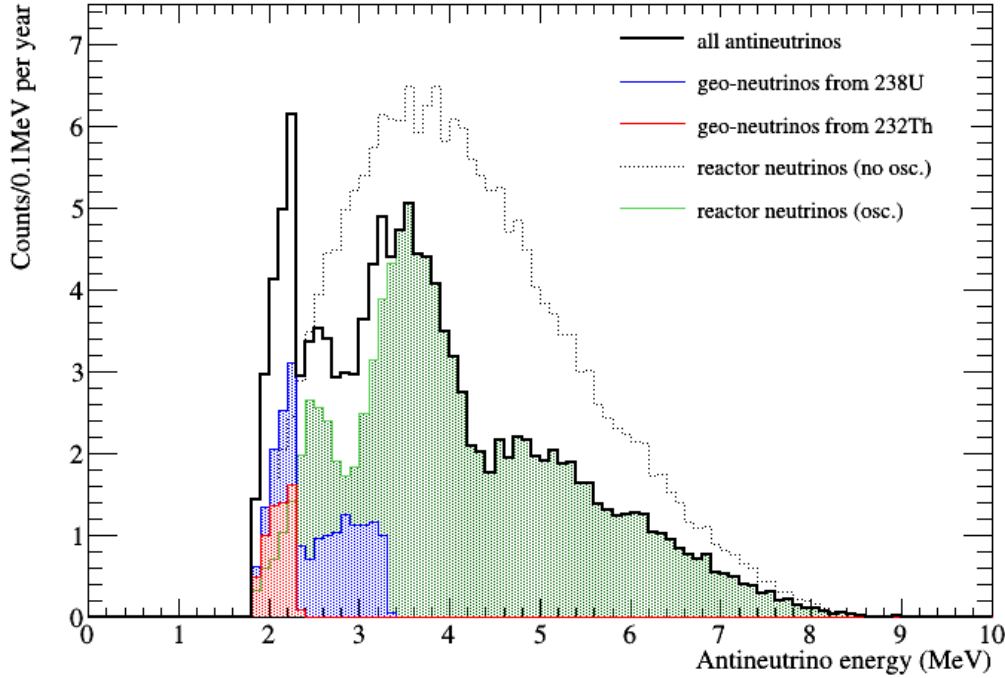


Figure 3.7: Example of the modified GEANT-4 generated MC of antineutrino interaction rate versus the inferred energy in SNO+ from the prompt event at SNO+. This plot depicts expected geoneutrino fluxes from ^{238}U and ^{232}Th in blue and red respectively with their proportions based on MidQ model calculations found in [55]. The green histogram shows the simulated reactor neutrino spectrum, including the effects of neutrino oscillations (for $\Delta m_{21}^2 = 7.53 \times 10^{-5} \text{ eV}^2$). Alongside this, the plot shows what the reactor spectrum would look like in the absence of neutrino oscillations, with the dotted line.

a specific dataset. For its analysis pipelines, the SNO+ experiment uses ROOT libraries [54], and all the processed data and simulation are stored in custom files called RATDS. This way both data files and detailed simulation files can be tested through the same reconstruction and analysis algorithms for accurate comparison. The detector state information and the simulation are constantly being updated as the detector is calibrated and the understanding of the detector responses improves.

When undertaking a simulation of the expected antineutrino flux from nearby

reactors, which are a primary background to the flux of geoneutrinos, the key pieces of information that need to be obtained are the distance from nearby reactor sources, and their energy spectra. These are stored in the continually updated ratDB tables, in which the spectra and other information needed for the simulation are determined by looking at publicly available reactor thermal output tables, and simulating spectra for each reactor as the distance to them is well known.

In order to simulate geoneutrinos in RAT the author created a SNO+ geoneutrino event generator. Unlike for reactor neutrinos, where the spectral shape can change depending on the location of reactors, oscillation baselines, and mix of fission isotopes, for geoneutrinos the spectrum is assumed as being produced by a uniform mix of naturally occurring uranium and thorium isotopes as discussed in Chapter 4. In addition, we note that over the Earth’s volume, the effect of neutrino oscillations averages out so that there is a single predicted geoneutrino spectral shape, see [23]. To create the SNO+ geoneutrino MC events for our analysis, the SNO+ RAT database tables were created using antineutrino spectra for uranium and thorium from calculations presented by Enomoto Sanshiro [24]. For the MC events, the expected relative rate of uranium and thorium contributions were obtained from Ondřej Šrámek’s calculations [55] described in greater detail in Chapter 4. For the purposes of Monte Carlo simulation, the default value of the geoneutrino flux was set to the MidQ rate (as given explicitly in Chapter 4, Table 4.2), however, the author wrote the MC generation code so that the relative rates can be adjusted.

With a given expected antineutrino input rate chosen, the IBD reaction was simulated uniformly inside the detector. This produced both positrons and neutrons simultaneously at the same location and time for Monte Carlo simulated IBD events.

These particles were then propagated through the volume according to their respective physical processes, using the GEANT-4 codebase. For positrons, this included a propagation path that allowed for scattering, ionization, and annihilation with appropriate γ rays produced as a result of each of these processes. For neutrons, this included the scattering and the capture on hydrogen and carbon, which were all modeled by the modified version of GEANT4 explained above.

For analysis in RAT presented in this thesis, the MC runs used for fitting and efficiency calculations had an exaggerated geoneutrino rate to provide additional statistics. We also emphasize that the Monte Carlo of geoneutrino detection was produced run-by-run, to ensure that fluctuations in detector state were accounted for in determining the signal acceptance efficiency for geoneutrino events. For each equivalent run of data, there was a simulation produced with all the recorded detector conditions, including threshold settings and overall detector status settings. Figure 3.7 shows an example of the MC-generated expected antineutrino spectra in SNO+. Geoneutrinos from ^{238}U and ^{232}Th are shown in blue and red respectively, with their proportions based on the MidQ model calculations by Ondřej Šrámek [55]. The reactor neutrino spectrum was produced both with the effect of neutrino oscillations included (shown in green for $\Delta m_{21}^2 = 7.53 \times 10^{-5} \text{ eV}^2$), and also for comparison, a spectrum of reactor antineutrinos was produced without neutrino oscillations (shown with a dotted line).

We now turn to the modeling of the geoneutrino signal spectra at SNO+, and in particular, the modeling of Sudbury’s surrounding geology to determine the natural radiogenic local contributions to the geoneutrino measurement at SNO+.

Chapter 4

Geoneutrino Signal Prediction and Modeling

In this chapter, we will discuss the elements needed for the prediction of the geoneutrino signal at the SNO+ detector. The bulk of this chapter will focus on the methodology the author developed with collaborator Laura Sammon over the course of PhD research, but we will also detail two other complementary approaches to the calculation undertaken by colleagues Ondřej Šrámek and Scott Wipperfurth, and compare the predictions from all these methods for the geoneutrino signal at the SNO+ site.

The three methods explored here include

1. A model for geological neutrino sources by Ondřej Šrámek, with whom the author has discussed methods for geoneutrino flux prediction, and from whom the author has obtained independent calculations for the predicted geoneutrino flux at SNO+, which are included in this thesis for comparison.
2. A model for geological neutrino sources by Wipperfurth, who developed a MATLAB code that implements three different geological models. This is a similar approach to Šrámek's, but allows for the incorporation of three different crust composition thickness and density maps, CRUST1.0 [56], CRUST2.0 [57], and

LITHO1.0 [58] (where these geological models have been compiled by other authors), for the purpose of marginalizing over different geophysical assumptions using Monte Carlo methods that will be discussed.

3. A refined model for geological neutrino sources created by Laura Sammon and implemented in collaboration with the author to determine the geoneutrino signal rate at SNO+. Our work on this expands Wipperfurth’s codebase to incorporate regional and lower crust information local to SNO+, and specifically to create a high-resolution geophysical model based on a MidQ Bulk Silicate Earth abundance prediction.

For the purposes of geoneutrino signal characterization, we have to understand production and detection at each specific experimental site. Figure 1.2 shows the geoneutrino energy spectra coming from different radiogenic heat-producing elements. In this thesis, we will focus only on uranium and thorium, as these are the radiogenic elements that have a portion of their antineutrino spectra extending above the detection threshold $E_{\text{IBD}} = 1.806 \text{ MeV}$. Therefore when building an expected geoneutrino signal in this thesis, we will only consider the uranium and thorium abundances as predicted by geological models.

4.1 Geoneutrino Signal Calculation

We now turn to the basic principles of computing a geoneutrino flux for a detector like SNO+. Consider a detector located at a given position r . Given a certain geological model, the antineutrino spectrum at a position r can be calculated using Equation (4.1) [51], which is a volume integral weighted by radiogenic elemental abundances, the decay rate of these radiogenic elements, and the probability of a

$\frac{dN(\vec{r}, E)}{dE}$	Number of detectable geoneutrinos	TNU
ϵ	10^{32} protons $\times 3.154 \times 10^7$ s $\times 100\%$	protons \times s
λ	decay constant	decay / (atom \times s)
N_A	Avogadro's number	atom / mol
μ	Standard atomic mass	kg / mol
σ_ν	IBD interaction cross-section	m^2 / proton
$\frac{dn_\nu}{dE}$	Geoneutrino production spectra	$\bar{\nu}$ / decay
P_{ee}	electron antineutrino survival probability	-
A	abundance (mass fraction) of geoneutrino emitters	-
ρ	density	kg / m^3
$ \vec{r} - \vec{r}' $	distance to detector	m

Table 4.1: Variable definitions for Equation (4.1). Note that this is valid for a single radiogenic element. In this work, we sum over contributions from uranium and thorium to the geoneutrino flux.

neutrino propagating from source point r' to r as a function of neutrino energy. Then the equation for the expected number of neutrino events is

$$\frac{dN(\vec{r}, E)}{dE} = \epsilon \frac{\lambda N_A}{\mu} \sigma_\nu \left(\frac{dn_\nu}{dE} \right)_i \int_{\oplus} P_{ee}(E, |\vec{r} - \vec{r}'|) \frac{A(\vec{r}') \rho(\vec{r}')}{4\pi |\vec{r} - \vec{r}'|^2} d\vec{r}'. \quad (4.1)$$

In this Equation, $\frac{dN(\vec{r}, E)}{dE}$ is the differential of the number of geoneutrinos that will interact in a detector per unit neutrino energy, $\epsilon \frac{\lambda N_A}{\mu} \sigma_{IBD}$ is the expected production rate adjusted to include the IBD cross-section and a conversion factor ϵ to give the result in a standard unit, the Terrestrial Neutrino Unit (TNU, one interaction per 10^{32} protons per year), $\left(\frac{dn_\nu}{dE} \right)_i$ is the antineutrino production spectrum, $P_{ee}(E, |\vec{r} - \vec{r}'|)$ is the survival probability (see Chapter 1), and $\frac{A(\vec{r}') \rho(\vec{r}')}{4\pi |\vec{r} - \vec{r}'|^2}$ contains the geological abundance of each radiogenic element, weighted by a $1/R^2$ flux factor. Table 4.1 provides a more detailed definition of all the variables. In total, Equation (4.1) yields a rate for the observable geoneutrino spectrum, accounting for the effective exposure of the detector

ϵ , which is defined in units of TNU. Hence when using this result and comparing it to observations at a detector, we must determine what the effective exposure of our experiment is, which depends on the number of target protons, observation time, and an efficiency factor that is not included above. This expression also incorporates how the IBD threshold affects the IBD detection rate, since σ_{IBD} is a function of energy (see Chapter 3, Equation 3.6), so that the yield quoted here only is restricted to the number of antineutrinos that would actually be detectable by SNO+.

Finally, we note that when implementing the above procedure for computing the geoneutrino signal, our choice of the abundance factor A , in the case of uranium and thorium, will be determined using details of U and Th abundances in various types of crustal rock as determined in crustal models, plus the whole Earth abundances of refractory elements outlined in Chapter 2 (in general based on the models of the Bulk Silicate Earth). However, if this analysis were extended to include potassium as a geoneutrino source, some additional modeling would be necessary.

4.2 Geoneutrino Rate Predictions for SNO+

4.2.1 Šrámek Model

Table 4.2 shows the output for SNO+ calculations done by Ondřej Šrámek, for LowQ, MidQ, and HighQ models, provided in private communication. The calculation is based on the same methods of Šrámek et al. 2016 [55]. For this calculation, the assumption of an overall average neutrino oscillation survival probability was used ($\langle P_{ee} \rangle = 0.553$). For the geological input, the three-dimensional spatial structure and rock density were integrated from CRUST1.0 [56]. For the estimates of chemical composition, the crust was divided into layers: Oceanic Crust (OC) and Continental

	Low Q	Mid Q	High Q
Th	8.21 ± 0.65	9.53 ± 0.77	11.51 ± 0.81
U	29.72 ± 4.69	34.11 ± 5.04	41.54 ± 4.95
Th+U	37.93 ± 5.34	43.64 ± 5.81	53.05 ± 5.75

Table 4.2: Output of SNO+ geoneutrino signal calculations provided by Ondřej Šrámek, based on methods detailed in Šrámek et al. 2016 [55]. This shows the expected geoneutrino flux in TNU at SNO+, according to different radiogenic heat models.

Layer	Th	U
Upper CC + sediments	$(10.5 \pm 10\%) \times 10^{-6}$	$(2.7 \pm 21\%) \times 10^{-6}$
Middle CC	$(6.5 \pm 8\%) \times 10^{-6}$	$(1.3 \pm 31\%) \times 10^{-6}$
Lower CC	$(1.2 \pm 30\%) \times 10^{-6}$	$(0.2 \pm 30\%) \times 10^{-6}$
OC sediments	$(8.10 \pm 7\%) \times 10^{-6}$	$(1.73 \pm 5\%) \times 10^{-6}$
OC crust	$(0.21 \pm 30\%) \times 10^{-6}$	$(0.07 \pm 30\%) \times 10^{-6}$
CLM	$(150 \pm^{+277}_{-97}) \times 10^{-9}$	$(33 \pm^{+49}_{-20}) \times 10^{-9}$
Depleted Mantle	$(21.9 \pm 20\%) \times 10^{-9}$	$(8.0 \pm 20\%) \times 10^{-9}$
Enriched Mantle	$(147 \pm^{+74}_{-57}) \times 10^{-9}$	$(33 \pm^{+24}_{-18}) \times 10^{-9}$

Table 4.3: Abundance estimates in terms of mass fraction of the element and the rock (kg/kg). For each layer, the abundances were assumed to be uniform [55].

Crust (CC) including sediment layers. Below these layers, a layer of Continental Lithospheric Mantle (CLM) was included, which extended to 175 km depth. This mantle layer was separated into two layers as well: the Depleted Mantle (DM) and Enriched Mantle (EM). All the layers were assumed to have a uniform distribution of uranium and thorium and did not include any types of enriched chemical reservoirs. The geochemical inputs for different regions were taken from [59]. Table 4.3 shows the summary of abundance mass fractions used in the calculation [55]. With the source volume specified, a numerical integration was done over the expected thorium and uranium abundances from defined layers and propagated the geoneutrinos to the detector location based on the production spectra computed in Enomoto’s thesis [24].

4.2.2 Wipperfurth Model

Wipperfurth has undertaken detailed studies of how different global crustal composition models affect the predicted geoneutrino flux. He made a comparison between three different geophysical models, all under the assumption of a Bulk Silicate Earth abundance of the “MidQ,” variety, as detailed in Chapter 2). The three models Wipperfurth implemented were CRUST1.0 [56], CRUST2.0 [57], and LITHO1.0 [58]. The geochemical information for the chemical composition of the overall crust was taken from Huang et al. 2013 [59], specific chemical composition of oceanic layers was taken from White et al. [60], information for the chemical composition of sediments was taken from Plank et al. [61], composition of the continental crust was taken from Rudnick et al. [62]. The mantle is divided into enriched and depleted layers and the chemical composition is extrapolated from the geophysical information known from Preliminary Reference Earth Model [63], and mass balance calculations for U and Th performed by Arevalo et al. 2013 [64] and Wipperfurth et al. 2018 [65].

The MATLAB code created by Wipperfurth divides the Earth into a network of voxels. Each voxel is then assigned a value for the mass and density of rock with uncertainty, as predicted by the different geophysical models listed above. Then the voxel takes in the concentrations of U and Th for the type of rock assigned. In the computation the correlations between these elements and observed rock types are taken into consideration. Each iteration of code samples the inputs based on their allowed uncertainty and correlations. To compute the expected signal, Equation (4.1) is used, although the volume integral is effectively replaced by the volume of each voxel and then the total signal is the sum of all the voxels.

For the computation of the neutrino survival probability, Wipperfurth used a

	CRUST2	CRUST1	LITHO1
Bulk CC (TNU)	$37^{+9.7}_{-8.1}$	$32^{+9.6}_{-7.4}$	$33.8^{+9.6}_{-7.5}$
Total (TNU)	$49^{+9.7}_{-8.1}$	$45.7^{+9.3}_{-7.7}$	$46.8^{+9.4}_{-7.8}$

Table 4.4: Comparison of expected geoneutrino signal (in TNU) from each geophysical crust composition model, from Wipperfurth’s code [66]. The top row is the contribution coming from the continental crust (CC) and the bottom row is the total signal.

neutrino mass splitting of $\Delta m_{21}^2 = 7.53 \times 10^{-5}$ ev 2 . The number of antineutrinos was calculated and propagated for geoneutrino energy increments of 75 keV across the geoneutrino spectrum starting at a threshold energy of 1.8 MeV. The output was given in units of TNU. One of Wipperfurth’s refinements was to incorporate the computation of more statistics closer to the detector, to provide a computationally efficient and accurate prediction for the geoneutrino flux. As the geoneutrino signal has a $1/R^2$ dependency, the closer to the detector a voxel is, the more significant the contribution of that voxel becomes. Therefore the meshing of the voxels was not uniform but implemented in a way that the voxels were larger the further away they were from the detector. The largest voxels had a uniform size up to a distance of around 500 km from the detector, and within that distance the voxel volumes were reduced in steps according to a $1/R^2$ scaling closer in to the detector. This type of re-meshing was necessary to save computational time, and the fluxes were carefully chosen and tested, to confirm that having larger voxels further did not significantly affect the final flux.

4.3 Refined Regional Model

We now turn to the computation of the geoneutrino signal completed by Sammon and the author for use in the SNO+ geoneutrino analysis. The predictions already discussed in Section 4.2 use global geological models. However, as is clear from the geoneutrino signal’s $1/R^2$ dependence on source volume location, which appears inside the integral in Equation (4.1), we are motivated to understand and include the contribution from the crustal composition close to the detector, since this will have a large impact on the predicted geoneutrino signal.

The SNO+ experiment is located at a rather unique geological location. The area around SNOLAB is one of the oldest, and the third largest known impact crater sites, whose creation dates back to the Paleoproterozoic era [67]. A 3-D compositional model of the area around SNO+ detector has been compiled in [68], and is shown in detail in Figure 4.1 and Figure 4.2. The authors of [68] combined data from geochemical sampling [68], seismic geophysical surveys [69], along with data from a magnetic and gravitational/accelerometric survey [70]. As shown in Figure 4.1 the SNO+ regional study was performed only considering Far Field Crust (FCC) and Local Crust (LOC). The rest of the Earth was not included in this study beyond the $6^\circ \times 4^\circ$ region. The LOC was subdivided into Local Lower Crust (LLC), Local Middle Crust (LMC), and Local Upper Crust (LUC). The LUC was then subdivided into the Surrounding Upper Crust (SUC) and the Close Upper Crust (CUC). The CUC, in particular, is of special interest, since it represents the nearest 50×50 km region surrounding Sudbury. The work in [68] revised and extended an earlier geological dataset compiled by Huang et al. in 2014 [71]. This work also created a downloadable 3-D numerical model for U and Th distributions of the studied area, with the nearest

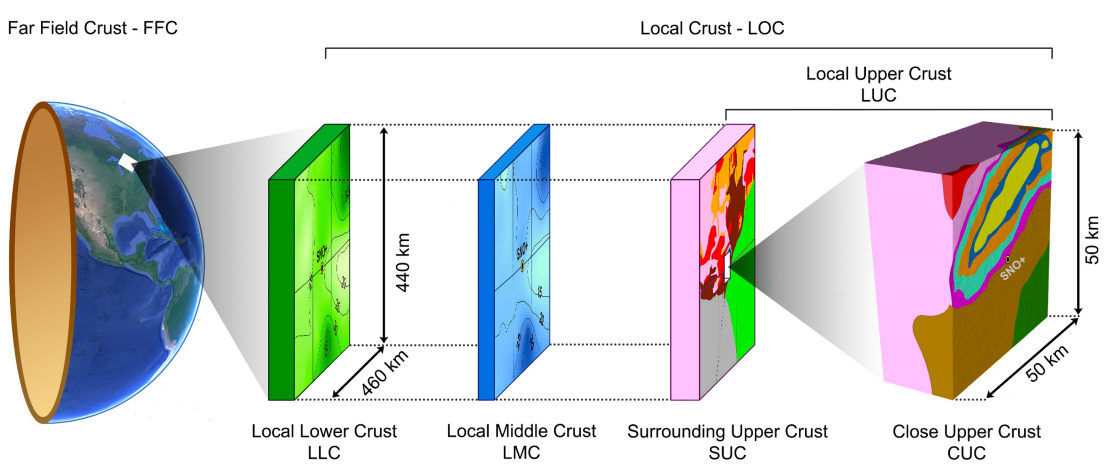


Figure 4.1: The SNO+ regional study completed for our geoneutrino analysis included detailed incorporation of the Far Field Crust (FFC) and Local Crust (LOC). A less detailed Earth model was included for the region beyond the $6^\circ \times 4^\circ$ geocoordinate slice surrounding the Sudbury region, shown above. The LOC was further subdivided into the Local Lower Crust (LLC), Local Middle Crust (LMC), and Local Upper Crust (LUC), and the geology of each of these subregions was incorporated. The LUC was in turn subdivided into the Surrounding Upper Crust (SUC) and the Close Upper Crust (CUC). The CUC represents the nearest 50×50 km region. Figure adapted from [68].

CUC area being much higher resolution than in previous studies.

Table 4.5 shows the results from 15k iterations of the Wipperfurth code [66] that we modified to include high-resolution geological composition models surrounding the detector. The high-resolution model was constructed using the CrustMaker model created by Laura Sammon as part of her work on the lower crustal composition in the Southwestern United States [72], with the addition of upper crust compositional modeling from Strati et al. [68]. The Nearfield lower crust model was derived by using the local USArray data [73] as the seismic input to crustmaker outlined in [72]. Figures 4.3 and 4.4 show the distribution of U and Th in the nearfield crust model at example depths of 1km, 10km, and 30km. Here the colors shown correspond to the

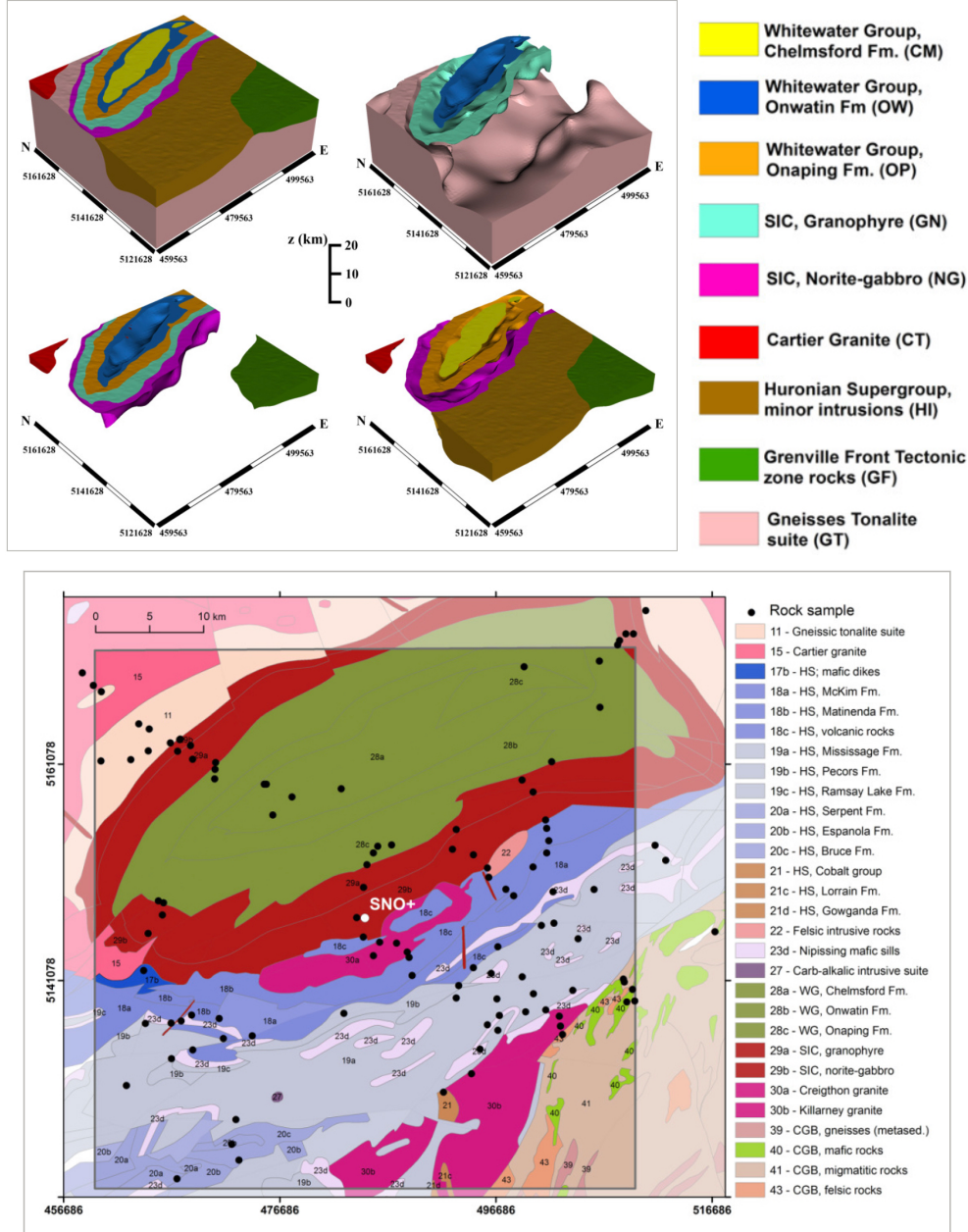


Figure 4.2: A 3-D rendering of the CUC geological model used in this study is shown, with rock types indicated by the color bar on the right. Each panel removes certain rock types to make the 3-D features of each rock type clearer. One geochemical dataset used to construct the 3-D CUC model is shown below. Both figures are adapted from [68].

	U (TNU)	Th (TNU)	Th+U (TNU)
FarField Crust	$13.1^{+2.9}_{-4.3}$	$3.6^{+0.55}_{-0.35}$	$16.8^{+3.3}_{-2.45}$
NearField Crust	$14.4^{+3.05}_{-2.2}$	$4.0^{+0.65}_{-0.4}$	$18.6^{+3.5}_{-2.6}$
Lithospheric Mantle	$1.6^{+1.15}_{-0.45}$	$0.5^{+0.4}_{-0.15}$	$2.1^{+1.55}_{-0.6}$
Total Lithosphere	$29.0^{+7.05}_{-4.75}$	$8.1^{+1.55}_{-0.95}$	$37.4^{+8.35}_{-5.6}$
Depleted Mantle	$3.7^{+0.55}_{-0.55}$	$0.8^{+0.35}_{-0.2}$	$4.6^{+0.95}_{-0.75}$
Enriched Mantle	$3.6^{+1.05}_{-0.85}$	$0.8^{+0.35}_{-0.35}$	$4.3^{+1.45}_{-1.1}$
Grand Total	$36.3^{+8.7}_{-6.15}$	$9.7^{+2.3}_{-1.5}$	$46.2^{+10.8}_{-7.5}$

Table 4.5: Results of fifteen thousand iterations of our modified Wipperfurth MATLAB Monte Carlo simulation code [66], which incorporates three models of the Earth’s Bulk Silicate Region [56, 57, 58]. The Wipperfurth code was extended to include a high-resolution geological composition model around the detector. The high-resolution model was constructed by using the MATLAB CrustMaker package created by Laura Sammon during her research on the lower crustal composition in the Southwestern United States [72]. In addition, the upper crust was modeled using the Strati et al. model of the CUC, detailed in [68].

concentration of U(ppm). The first slice shows the combination of the Strati et al. [68] model from 46-47° latitude, and Sammon et al. for the rest of the slice [72]. The input for 20 km and 30 km slices comes completely from Laura Sammon’s CrustMaker. In general, as crustal depth increases, heat-producing element concentration decreases, though there is wide regional variability. The white star marks the detector location, which is not centered due to 47 degrees latitude being the extent of the USArray [73] at the time. White circles mark the location of seismic stations from the array. Note that abrupt color changes do not represent sharp changes in U concentration. Rather, they are a relic of the sampling rate and interpolation between data points, which

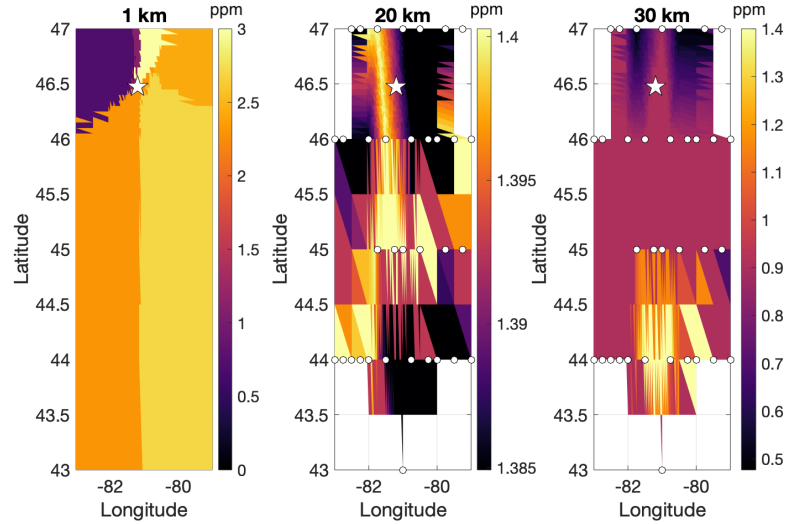


Figure 4.3: The distribution of U in the nearfield crust model at example depths of 1km, 20km, and 30km. Color corresponds to the concentration of U(ppm). The white star marks the detector location (which is not centered due to 47 degrees latitude being the extent of the USArray [73] at the time. White circles mark the location of seismic stations from the array.

was left coarse except in the tile immediately around the detector. Due to the fact that these slices only show the new inputs added with the latest modification of the code, the white areas and beyond the areas of these slices sample the default values from the Wipperfurth MATLAB code.

Figure 4.5 shows the scatter plot generated by running fifteen thousand iterations for the total expected geoneutrino signal from Th and U in TNU for the SNO+ versus the total expected radiogenic power from U+Th in TW. Note that the bottom axis does not account for radiogenic contribution coming from potassium, which would need to be included when comparing to the heat production models.

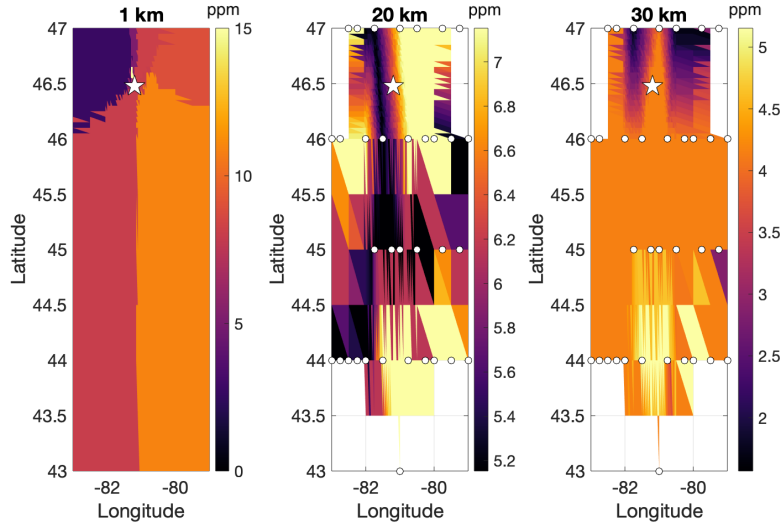


Figure 4.4: The distribution of Th in the nearfield crust model at example depths of 1km, 20km, and 30km. Color corresponds to the concentration of U(ppm). The white star marks the detector location, which is not centered due to 47 degrees latitude being the extent of the USAArray seismic array [73]. White circles mark the location of seismic stations in the array.

4.4 Geoneutrino Signal Prediction Comparison

In this Chapter, we have presented the calculation framework for determining the number of geoneutrino interactions at SNOLAB. The first was a simple global geological model of the Bulk Silicate Earth undertaken by Šrámek. The second came from a more involved numerical MATLAB code designed by Wipperfurth, which was further extended to include more finely detailed modeling of the region around Sudbury in this thesis and [72]. We compare the final results in Tables 4.2, 4.4, and 4.5, in our summary Table 4.6. We see that for all these methods, the predicted TNU geoneutrino signal at SNO+ is around 40–50, with uncertainties of around ± 10 , with the possible exception of the Šrámek result, which predicts a few less signal events for

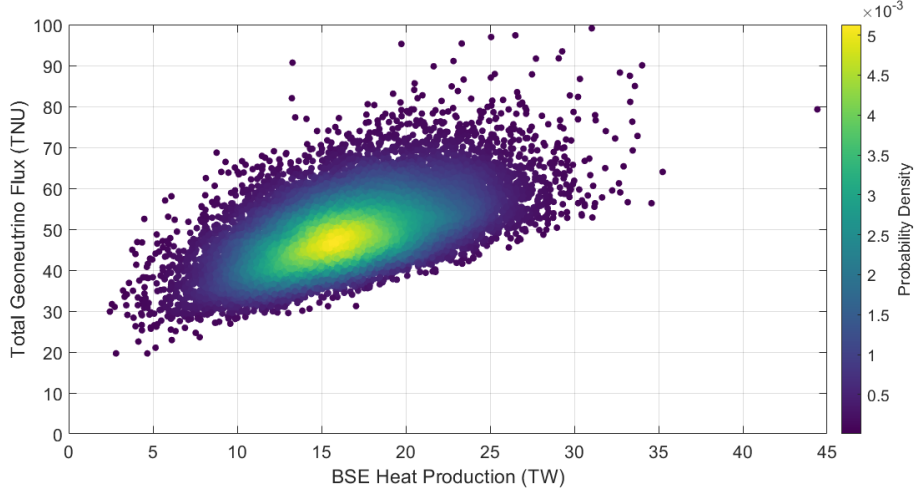


Figure 4.5: The total expected geoneutrino signal in TNU for the SNO+ experiment (y-axis) versus the total U+Th radiogenic power in TW (x-axis). The scatter plot shows a total of fifteen thousand iterations of the modified Wipperfurth MATLAB code developed by Sammon and the author. Each point is one iteration, and the color map represents the point density.

	Sammon & Semenec	Šrámek	Wipperfurth
Total (TNU)	$46.2^{+10.8}_{-7.5}$	43.6 ± 5.8	$46.8^{+9.4}_{-7.8}$

Table 4.6: Comparison of total expected geoneutrino signal (in TNU) from Šrámek MidQ, Wipperfurth LITHO1, and Sammon & Semenec (where these latter models are also MidQ).

a MidQ model. The slight increase in predicted signal events from the local model shown in Table 4.5 may be the result of incorporating a more detailed local geological model.

Having determined the expected number of geoneutrino signal events for a number of different geological models, we now turn to geoneutrino backgrounds and calibration of the SNO+ detector.

Chapter 5

Study of the $^{13}\text{C}(\alpha,\text{n})^{16}\text{O}$ Background for Geoneutrinos

There are a number of background processes that can mimic a geoneutrino inverse beta decay event. These are events that mimic the geoneutrino signal in the SNO+ detector, discussed in Chapter 3, where the positron and neutron produced in an inverse beta decay create prompt gamma rays from positron annihilation, followed by a gamma ray after the neutron is captured on hydrogen, around $200\ \mu\text{s}$ later. In this Chapter we study an inverse beta decay background process, called $^{13}\text{C}(\alpha,\text{n})^{16}\text{O}$ or alpha-n, where an alpha particle is captured on ^{13}C and produces oxygen and a high energy neutron,



where the high energy neutron can create both prompt and delayed mimic signatures that we will cover shortly. This will be a major background for the detection of geoneutrinos.

First, we discuss the variable that quantifies the time separation between the

prompt and delayed events, ΔT . We note that the timing of these events is determined by the SNO+ analysis package using position and time fit functions, and the state of the detector as discussed in Chapter 3. The position and time fitters use raw PMT hit times and hit PMT positions to calculate the most probable position and time of the event. In this work, a scintillator fitter developed by the SNO+ reconstruction group was used for all the MC and data. Here we formally define the timing difference between the prompt and delayed event as

$$\Delta T = t_d - t_p, \quad (5.2)$$

where t_p is the prompt event time and t_d is the delayed event time.

A set of coincident events with $\Delta T \approx 200 \mu\text{s}$ can be produced through the random coincidence of unrelated particle processes occurring in the detector. These backgrounds are minimal and can usually be excluded since they will not have the position, timing, and energy characteristics of an IBD event (see further discussion of this kind of accidental background in Section 6.2.5). However, there are certain backgrounds that mimic the IBD signal very closely.

Besides the background provided by antineutrinos from nuclear reactors nearby SNO+, which produce actual antineutrino inverse beta decay events, the background process from $^{13}\text{C}(\alpha, n)^{16}\text{O}$ events (more commonly referred to as alpha-n events) are the most prominent background for the geoneutrino signal. Throughout this chapter, we will focus on the alpha-n background. Then we will discuss a classifier that aims to distinguish between alpha-n and IBD events, using the differences in residual timing profiles of neutron-induced proton recoils versus IBD prompt events. Furthermore we will present analysis of AmBe neutron calibration source external deployment data,

used for the verification of the proton recoil timing events against the MC simulated proton recoil events. Finally, we briefly discuss the AmBe source in the context of verification of our general knowledge about neutron propagation and capture at SNO+, which is relevant to both alpha-n as well as IBD events.

5.1 The alpha-n Background

The α particles that initiate the alpha-n event defined above, are created by radioactive contaminants inside the detector such as radon ^{222}Rn . There have been many precautions to minimize radon contamination in the SNO+ detector from the mine air at SNOLAB, such as the cover gas discussed in Section 3.2. However small amounts of radon still can still wander their way into the detector, especially during scintillator filling and other maintenance tasks that require access to the detector. If we look at the radon decay chain in Figure 5.1, we see that from the decay of ^{222}Rn there are quite a few α particles being created. With the exception of alpha particles originating from ^{210}Pb and ^{210}Po decay, other alpha particle decays on this chain are produced in decays that have relatively short lifetimes ranging from a few microseconds to a few days [74]. Hence if we detect a large ingress of radon due to some maintenance task or process of scintillator filling, one way to avoid those shorter lifetime background daughter isotopes is to just wait and let them decay away.

However, this strategy does not work for the ^{210}Pb daughters of the ^{222}Rn . The produced ^{210}Pb has a half-life of 22 years, which makes waiting for the background to decay away infeasible, especially if there are repeated small ingresses of radon. So after a radon ingress, once the decay chain reaches ^{210}Pb , the α rate will reduce, but the built up ^{210}Pb will decay more slowly over time, making alphas either directly

(although the branching ratio for direct alpha decay from ^{210}Pb is small and thus practically negligible) or primarily through the alpha decay of ^{210}Po . One particularly troublesome part of ^{210}Po decays, is that its daughter isotope is stable (^{206}Pb), making it impractical to tag and cut this decay from the analysis using a timing coincidence. This can be compared to the alpha decay of ^{214}Po , which is coincident in time with the prior beta decay of ^{214}Bi , making it possible to tag and cut alpha events produced in ^{214}Po decays using coincidence tagging. This $^{214}\text{BiPo}$ coincidence tagging has turned out to be useful for energy calibration which will be described in Chapter 6. Over time during experiment construction, there have been several times when AV was exposed to air, which led to a large amount of ^{210}Pb to be plated out on the surface. This type of contamination can also happen on the surfaces of the scintillator plant. Therefore we expect the contamination of ^{210}Pb radon daughters could be introduced to the bulk scintillator volume from the AV surface, as well as the scintillator processing plant. Fiducial volume cuts can be applied to keep the analysis away from the surface where we expect more alphas, however, the ^{210}Po decay producing α particles and the $^{13}\text{C}(\alpha,\text{n})^{16}\text{O}$ in the bulk scintillator volume need to be well understood.

Figure 5.2 illustrates three processes by which the $^{13}\text{C}(\alpha,\text{n})^{16}\text{O}$ process can imitate the inverse beta decay coincidence signal. We list these below.

1. Proton recoil: The majority of the time, as the neutron produced in $\alpha + ^{13}\text{C} \rightarrow \text{n} + ^{16}\text{O}$ thermalizes, it will scatter with protons. As shown by Mills [76], the mean scatter time for these protons is about 7.5 ± 1.2 ns. Scattered protons will recoil and produce scintillation light, the combined light can be tagged as a prompt event, which then will be followed by the neutron getting captured on hydrogen, resulting in a delayed 2.2 MeV event. This makes $^{13}\text{C}(\alpha,\text{n})^{16}\text{O}$ a

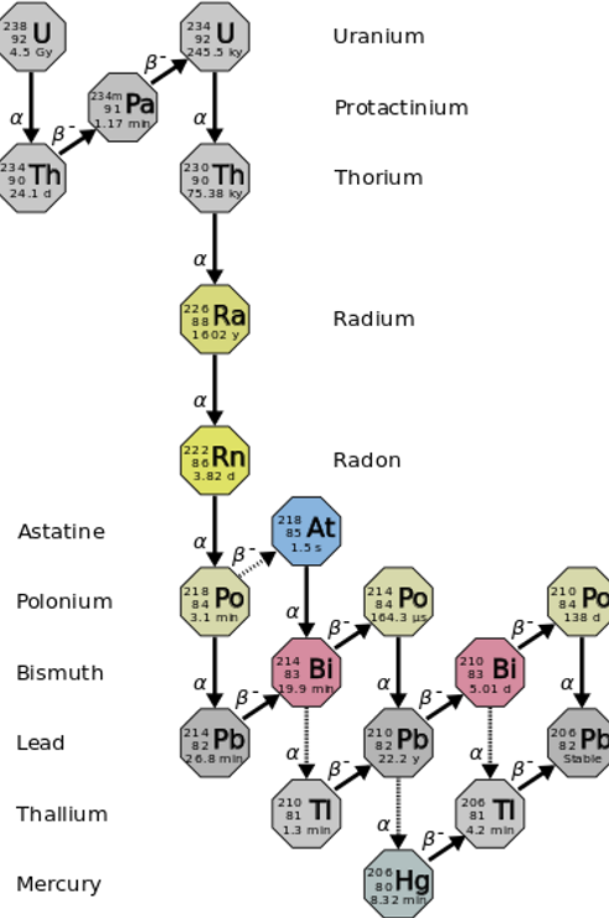


Figure 5.1: The complete ^{238}U decay chain is shown, taken from [75], of which ^{222}Rn is a subset.

nearly perfect IBD coincidence event impostor, since the time for the neutron to thermalize (around 200 μs) will mimic the thermalization time of a neutron produced in IBD.

2. Inelastic scattering: Besides scattering off protons, sometimes neutrons will scatter with ^{12}C . This can excite ^{12}C , and in the process of de-excitation, $^{12}\text{C}^*$ can produce a 4.4 MeV γ which can be tagged as a prompt event. The neutron

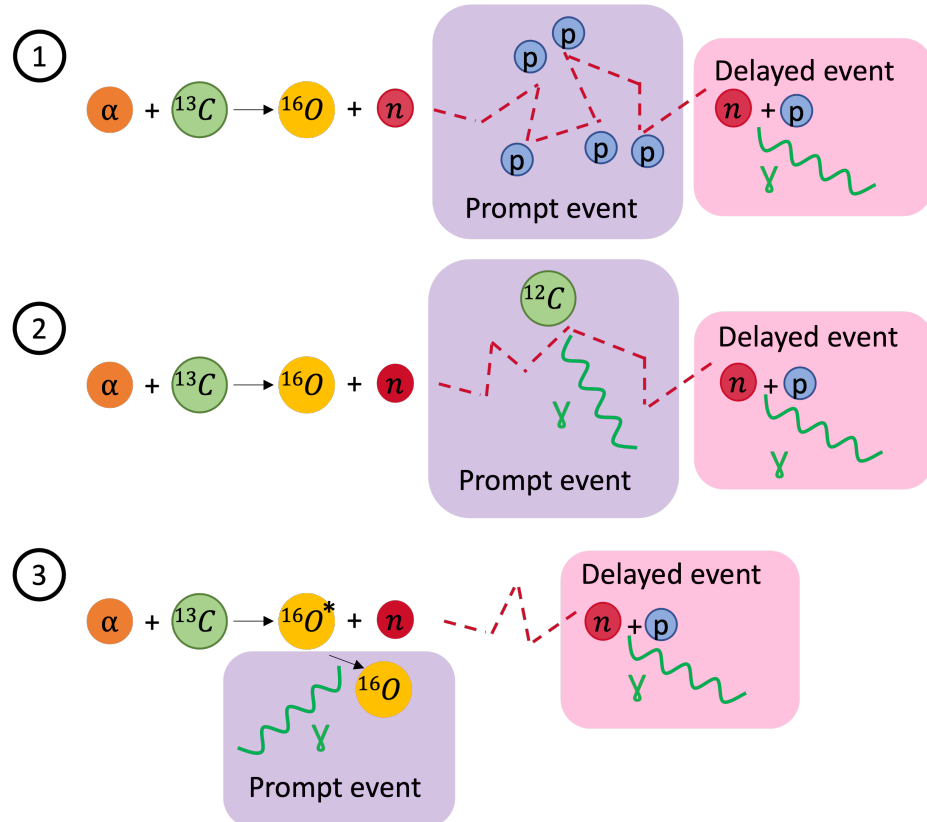


Figure 5.2: Illustration of three processes for how the $^{13}\text{C}(\alpha, \text{n})^{16}\text{O}$ can imitate the inverse beta decay coincidence signal. 1. Proton recoil: the neutron produced scatters off protons. These recoiling protons will produce scintillation light which can be tagged as a prompt event. The neutron is then captured resulting in the delayed event. 2. Inelastic scattering: neutron will scatter off a ^{12}C , which excites ^{12}C and in the process of de-excitation it produces a 4.4 MeV γ which can be tagged as a prompt event. The neutron is then captured on a proton, resulting in the delayed event with the characteristic 2.2 MeV deuterium de-excitation γ following neutron capture. 3. De-excitation: the $^{16}\text{O}^*$ is produced in an excited state and produces a 6.1 MeV γ while de-exciting, which is tagged as a prompt event. Once again the delayed event is provided by neutron capture.

is then captured on a proton, resulting in the delayed event.

3. De-excitation: during the initial α capture the resulting $^{16}\text{O}^*$ can be produced in an excited state. While de-exciting $^{16}\text{O}^*$ produces an 6.1 MeV γ or can also sometimes produce an $e^+ + e^-$ pair which yields around 6.05 MeV total light. Either of these can be tagged as a prompt event. Once again the delayed neutron capture mimics the delayed neutron capture of IBD.

Figure 5.3 shows MC simulations of expected interactions from the $^{13}\text{C}(\alpha, n)^{16}\text{O}$ background in the SNO+ detector, for the scintillator phase, using the same detector state information as used for the data runs later in this thesis. For more discussion of the detector state see Section 6.1. In Section 6.4, the event selection criteria for IBD-like events will be described; for now, we note that the same cuts are applied while looking at these MC $^{13}\text{C}(\alpha, n)^{16}\text{O}$ events. The selected events that matched the energy and timing characteristics of an IBD event are shown. The first plot shows the tagged alpha-n prompt event energy spectra. Here the three described processes described above are clearly visible and enumerated as per their description above. The second plot shows the energy spectra for the tagged delayed event. While the delayed event in the second plot exhibits all the characteristics expected from an IBD delayed event, we note that the prompt processes exhibit a variety of energies, and as will be developed later, also have different timing profiles for the energy they deposit, which can be used as an additional method to reject alpha-n events.

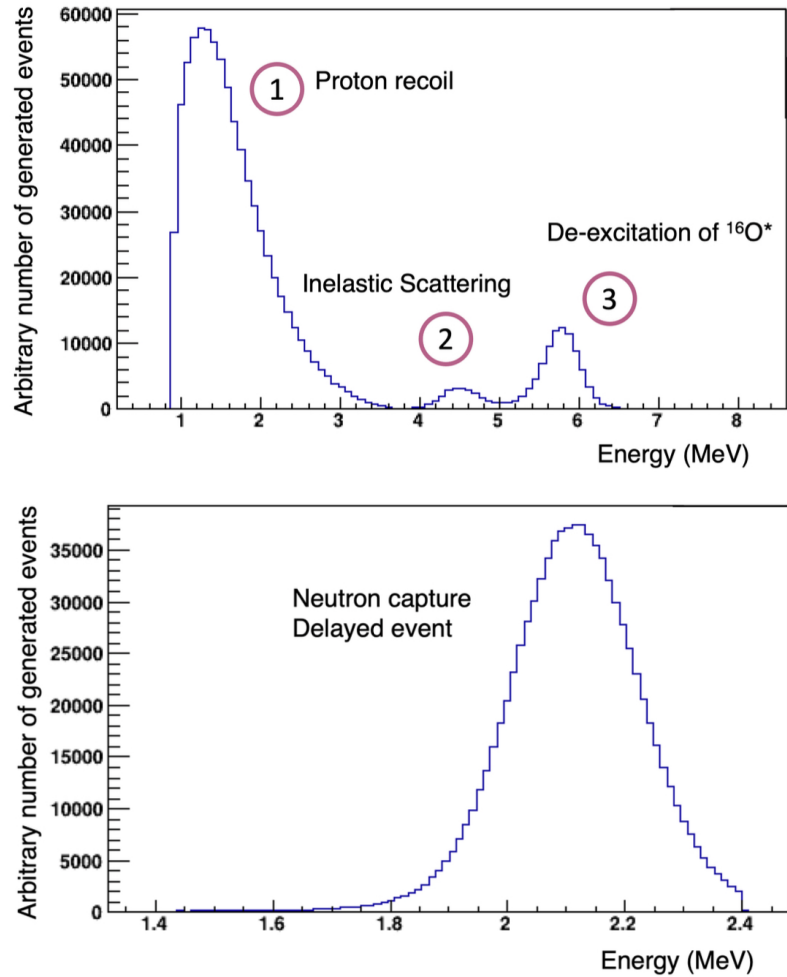


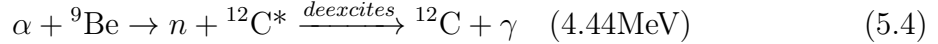
Figure 5.3: In the upper plot, the energies from a MC simulation of the alpha-n background prompt events are shown, coinciding with the “fake” prompt event processes outlined in the text: 1. an alpha-n neutron recoiling with protons creates a prompt event (note the wide spread in deposited energies), 2. the neutron’s inelastic scattering with carbon produces a 4.4 MeV gamma ray during the de-excitation of the carbon, 3. $^{16}\text{O}^*$ produced in the initial alpha-n interaction de-excites and emits either a 6.1 MeV gamma or an electron-positron pair of the same energy. In the bottom plot, the MC simulation energies of the delayed events from alpha-n neutron capture on hydrogen is shown.

5.2 AmBe Neutron Source Calibration

An essential part of antineutrino detection is the calibration of neutron dynamics in the SNO+ detection volume using an AmBe calibration source. The AmBe calibrations source is composed of both ^{241}Am and ^9Be . When ^{241}Am undergoes its α decay, it produces an α that can combine with ^9Be to produce a neutron and ^{12}C .



The neutrons produced in this manner then can be used to calibrate energy, resolution, and detection efficiency, and adjust the MC simulation in terms of position and timing for the neutron capture and scattering in the SNO+ detector. About 70% of the time AmBe will also produce a 4.4 MeV γ from the excited state of carbon,



AmBe is a great source for calibration, since the events shown in Equation (5.4) can be tagged as coincidence events similar to IBD coincidence tagging, where here instead of positron annihilation being coincident with a later neutron capture (as in IBD events), the delayed coincidence comes from the prompt interaction of the gamma and the produced neutron, which as with the antineutrino events will get captured by hydrogen and produce a 2.2 MeV γ . Of course, as detailed in Section 5.1, fast neutrons can also cause proton recoils or inelastic nuclear scattering followed by de-excitation, which can both be mistaken for a prompt IBD event, similarly to $^{13}\text{C}(\alpha, n)^{16}\text{O}$ background events.

5.3 AmBe Calibration Dataset

At SNO+, the AmBe source was designed for the water deployment [77] and was deployed in the external water just outside the acrylic vessel. Figure 5.4 shows AmBe-source coincidence event prompt and delayed event positions, in the acrylic vessel x-y coordinate plane. The z-coordinate for this deployment was set to zero, meaning the source was placed in the midplane of the detector.

Because the AmBe source is outside the acrylic vessel, the number of neutrons making it into the acrylic vessel was reduced. In the case of such an external deployment, IBD-like coincidence events will occur in the detector for about 10% of the total AmBe events. In addition, we note that the reconstruction of the event near the acrylic vessel is significantly degraded compared to reconstruction if the source was deployed in the middle of the acrylic vessel. This occurs because the energy reconstruction is based on the total number of photons emitted by the scintillator (or water in some cases) during the event. The number of triggered PMTs (nhits) in the event is the way we determine the number of photons emitted, which is proportional to the energy deposited in the scintillator. In the case where the event happened close to the AV a loss of nhits happens due to the detector geometry. Nevertheless, AmBe still provided ample statistics with enough events that can make it deeper into fiducial volume to be well reconstructed, and the selection cuts were tuned so that the coincidence pairs that were selected were mostly pure AmBe events. We provide an accounting of all the AmBe dataset cuts in Table 5.1. The AmBe datasets used in this analysis are from external calibration runs in May 2022 (runs 300960-300987), August 2022 (runs 303516-303545), and February 2023 (runs 308653-308688). The bulk of analysis presented here is based on August data which has an approximate

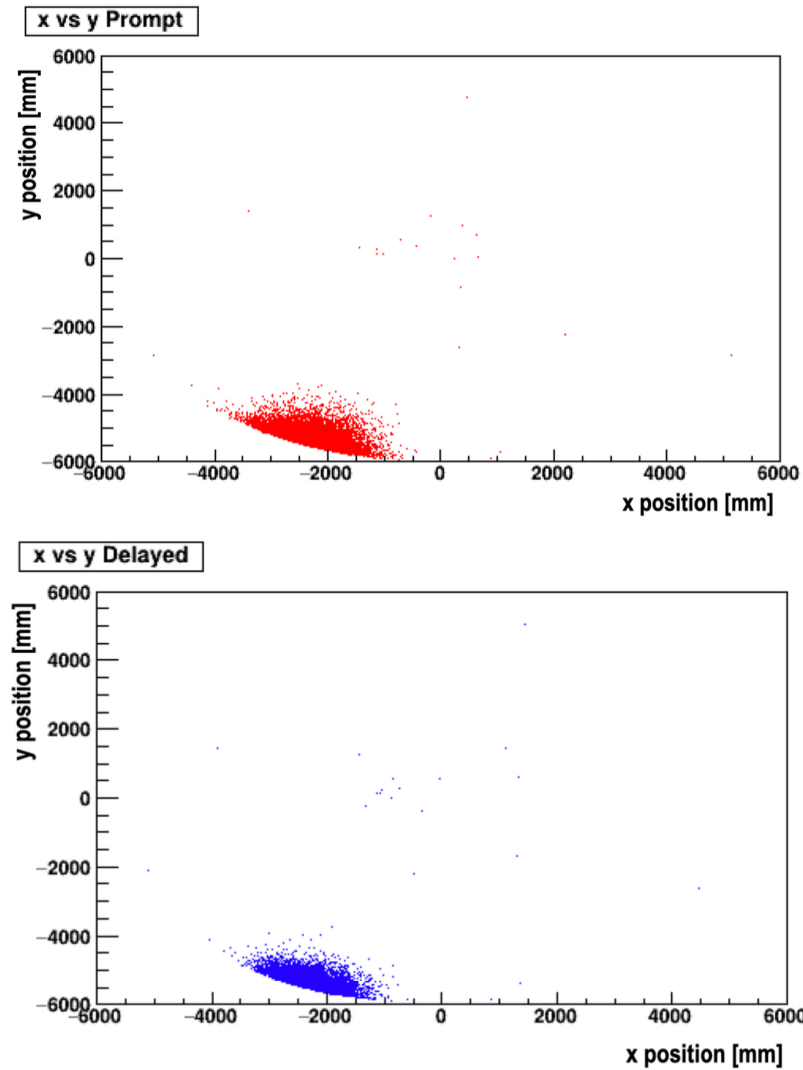


Figure 5.4: AmBe external deployment coincidence event prompt (top) and delayed (bottom) event positions in the acrylic vessel, given in x-y coordinates. No fiducial volume cuts were applied to these coincidence events, for illustration purposes. Both figures extend to AV volume, which is 6 m. These plots demonstrate that most interactions from the AmBe calibration source occurred at the edge of the SNO+ detector. This will be useful to keep in mind when examining the AmBe timing anomaly discussed below.

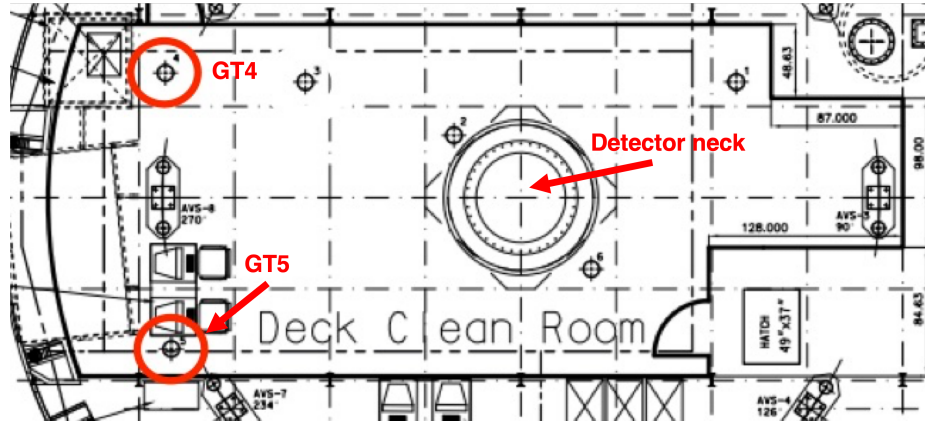


Figure 5.5: Schematic showing the top down view of SNO+ Deck Clean Room (DCR). Indicated in red are the calibration source deployment guide tube locations relative to the detector neck position.

Parameter	Cut Applied
Prompt Energy (MeV)	$0.2 < E < 10$
Delayed Energy (MeV)	$2.1 < E < 2.6$
ΔT (ns)	$400 < \Delta T < 500000$
ΔR (m)	$\Delta R < 1.0$
Fiducial volume (m)	$2.5 < R < 5.8$
FitValid	True

Table 5.1: Summary of the AmBe coincidence selection cuts applied to calibration data.

total duration of 19 hours. The source was deployed externally using guide tubes (GT4 and GT5), as shown in Figure 5.5. May and August's datasets were obtained with source deployed via GT5, $(x, y) = (-586.11, -252.41)$ cm, resulting in a radial distance from the center of the detector to be 6.38 m. February deployment was via GT4, $(x, y) = (-586.11, -207.96)$ cm, resulting in a radius of 6.21 m.

Figure 5.6 shows the prompt coincidence event energies from the AmBe August 2022 external deployment data, with the coincident event selection cuts applied as shown in Table 5.1. The shaded green region covers energies where most of the

expected proton recoils would be, where this process proceeds in the same manner as for alpha-n neutron interactions with protons. The shaded red area shows where neutron capture on protons is being tagged as prompt events. This is expected since the flux of neutrons from the AmBe source is large enough that two subsequent neutron captures could accidentally coincide within the few hundred-microsecond selection window. The yellow shaded area contains the 4.4 MeV γ peak that is emitted by excited carbon in the AmBe source. All of these features are expected to be seen in AmBe calibration data. Figure 5.7 shows the delayed coincidence event energies from the same dataset, however, to illustrate the whole distribution here the delayed energy cut was extended to $1.4 < E < 2.9$ MeV.

5.4 AmBe ΔT Feature

While investigating AmBe data, our analysis uncovered an anomalous feature in the timing difference between the prompt and delayed events. The author noticed some dependence on the prompt event energies, where the feature was more pronounced for coincidence events with somewhat higher energies. The anomaly here is that while we expect the distribution of ΔT times to fall exponentially for the AmBe neutrons, instead we see fewer events than an exponential distribution would predict for ΔT times around 100 μ s.

In Figure 5.8 AmBe ΔT distributions between prompt and delayed events are shown for a number of AmBe calibration runs, where the prompt energies have been restricted to $3.8 < E_p < 5.1$ MeV, since we found that this is a range of energies where there are a very noticeable number of missing events around $\Delta T = 100$ microseconds.

The deficit of events is being actively investigated since AmBe data is a primary

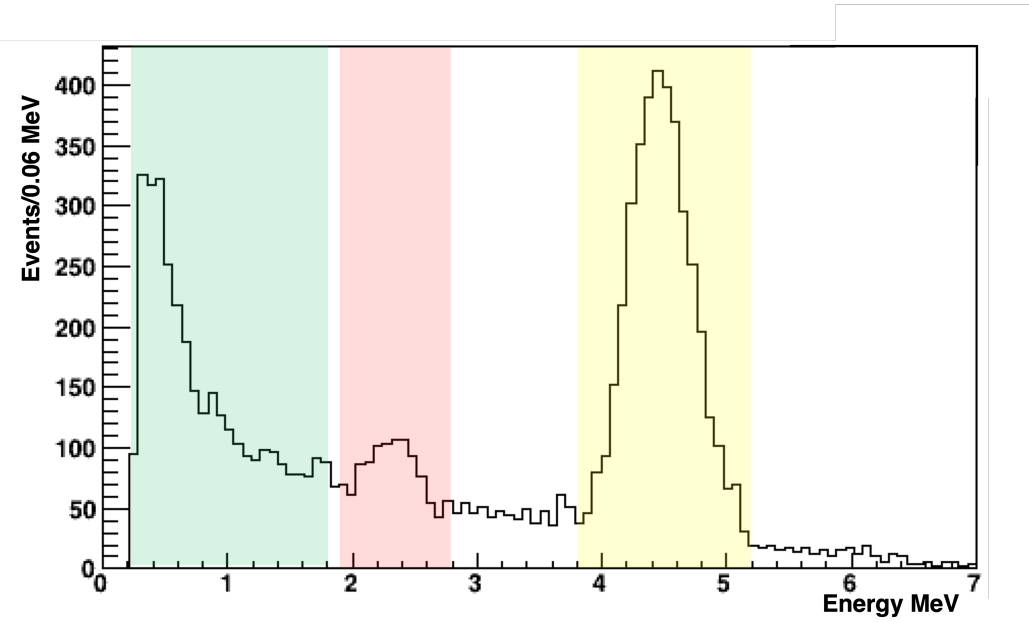


Figure 5.6: Prompt coincidence event energies from AmBe external deployment data, after coincidence cuts are applied as given in Table 5.1. These are similar cuts that are also applied to select for the antineutrino inverse beta decay interaction. The shaded green is the energy area where most of the proton recoils are expected to be since these produce around 0.5-2 MeV prompt events (through the same interactions detailed for alpha-n neutrons in Section 5.1). The shaded red area shows that some neutrons captured on hydrogen are being tagged as prompt events as there is an evident bump at the characteristic 2.2 MeV gamma energy that is emitted when a proton is captured on hydrogen. The yellow shaded area contains the 4.4 MeV γ peak which is emitted in some AmBe events from excited carbon produced in the AmBe reaction.

source of calibration for neutron capture and scattering processes at SNO+. While it is still too early to say exactly what is causing the deficit of AmBe calibration coincident events around the $100 \mu\text{s}$ time bin, here we will briefly discuss one idea for what could be causing the gap in timing data. In order to create a coincidence event, AmBe neutrons need to travel through the water shield around the SNO+ detector, since the AmBe source was deployed in water just outside the AV of SNO+. The

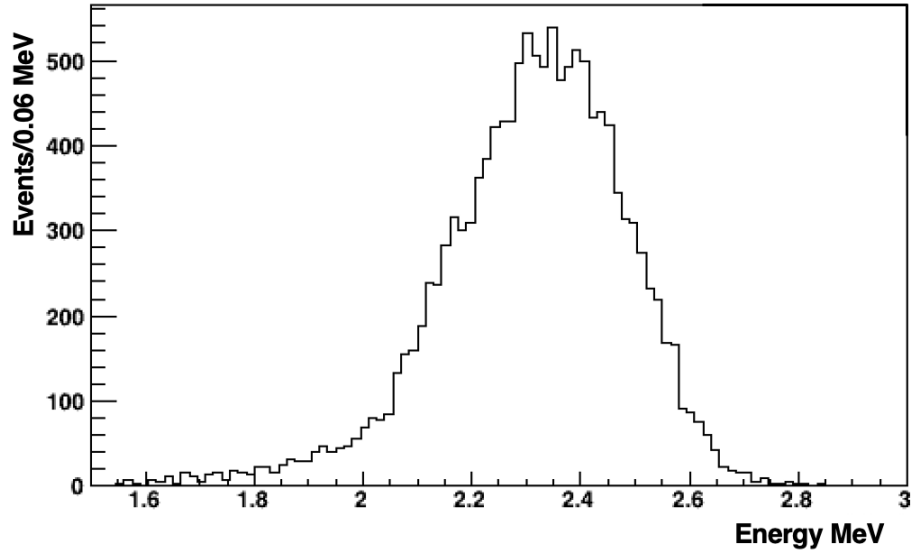


Figure 5.7: Delayed coincidence event energy spectrum from AmBe August 2022 external deployment data.

main idea is that we see two separate time distributions. One is from the neutrons that capture on the water outside the AV, and the produced gammas travel inside the AV where they get tagged. The second distribution comes with a delay in time from the neutrons that make it inside the AV and then get captured. It is possible that variation in the diffusion time for these neutrons, and changes in this variation as a function of energy (and corresponding fast neutron diffusion lengths), may also impact of the shifted AmBe event distribution at $100 \mu\text{s}$ coincidence times.

One idea to model this anomaly came from SNO+ collaborator Ryan Bayes, who was the lead for AmBe external deployment. First, he verified the effect the author found in the data. Then he had a hypothesis that the GEANT-based MC might not be modeling the diffusion lengths of neutrons traversing through water into the scintillator correctly. When running the GEANT simulation he noticed that neutrons

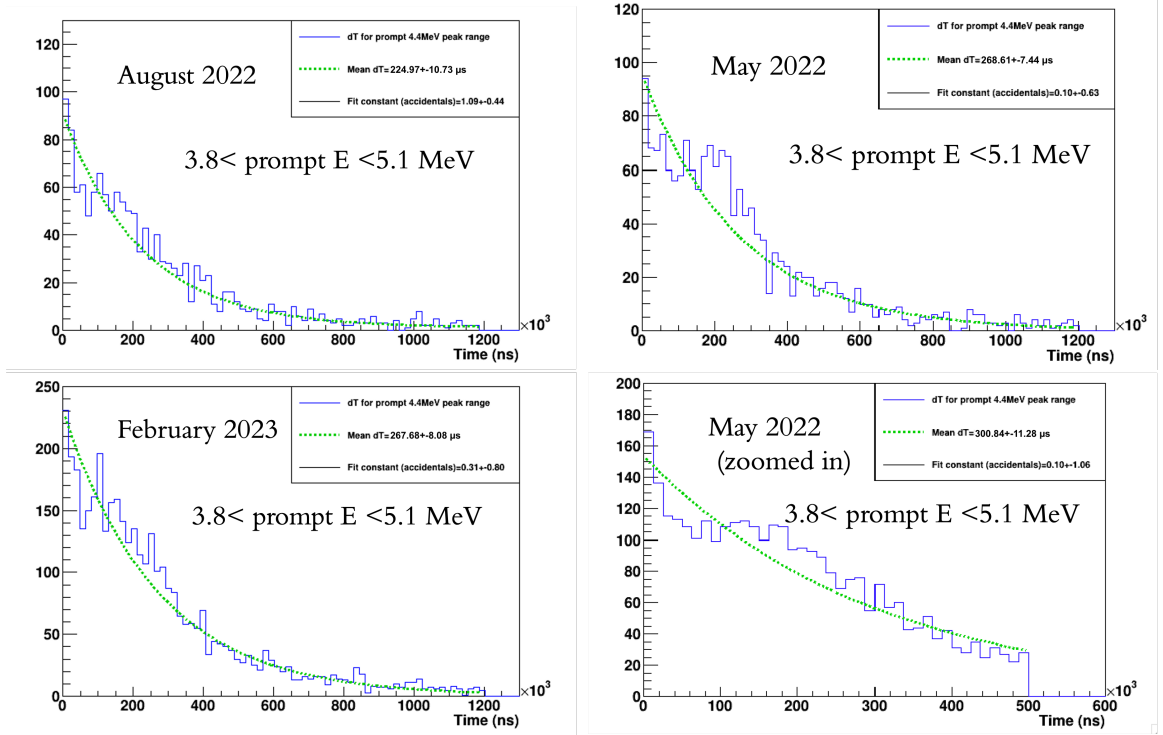


Figure 5.8: The time separation ΔT between prompt and delayed event pairs is shown, where this data has been cut to emphasize prompt energies around 4.4 MeV (the cut made was $3.8 < E_p < 5.1$ MeV). Here we note that in each run, a visible deficit of events is apparent at a time difference of around $100\mu s$. This effect has been noted in three separate AmBe source deployment datasets from August 2022, May 2022, and February 2023.

tend to capture faster and reach the scintillator volume less than 1% of the time, which does not seem to agree with what we see in the data. One possibility is that GEANT simulations assume a shorter diffusion length than it should. He noted that for fast neutrons of ($K_n > 0.5$ MeV) the diffusion length is around 5.75 cm, whereas for thermal ($K_n < 0.25$ MeV) neutrons the length is 2.88 cm in water (where Bayes took these values from [78]). So for the population of tagged neutrons that were captured in the scintillator, the capture time might be delayed, compared to the MC simulation, because these neutrons would have to travel a bit further before they

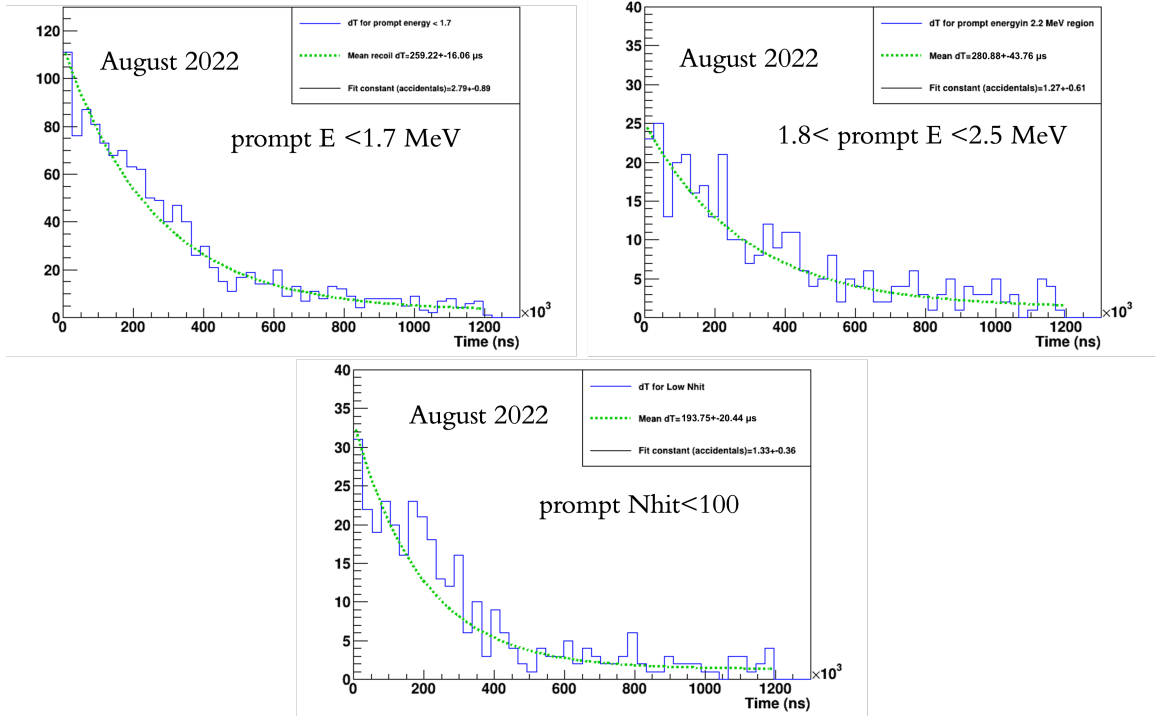


Figure 5.9: The coincident event time separation ΔT between prompt and delayed event pairs is shown. Figures made for the August 2022 dataset, cut at different prompt energy regions according to figure 5.6. As well as a check on a very low energy region, by using a cut on nhits to be below a 100.

reach "thermal" energies at which they get captured. Bayes made a toy MC that simulated what the delay time distribution would look like, if we randomly sampled initial neutron velocity vectors, and then required several neutron scatters before capture, and recorded neutrons that capture in scintillator. This code estimates the position and timing of the neutron captures after three fast neutron diffusion lengths and one thermal diffusion length, drawing from a Gaussian distribution around the expected diffusion lengths, then computing delay times for neutrons that end their diffusion in the AV, after moving through 21 cm of water.

We will now further investigate this idea of time distribution dependence on diffusion lengths. We will extend Bayes's toy MC treatment by explicitly computing the fast neutron diffusion lengths for a range of fast neutron energies, for which we see the AmBe anomaly, and then present a similar toy MC distribution, adding together the contribution from this range of initial fast neutron energies.

Figure 5.10 shows the measured AmBe neutron energy spectra [79]. Three regions represent the neutrons produced depending on the carbon nuclei state. 1. ^{12}C was in second excited state. 2. ^{12}C was in 1st excited state. 3. ^{12}C was in ground state. It is important to note that only the first excited state ^{12}C will emit the signature 4.4 MeV γ as described earlier in equation 5.4. Because we tag the AmBe coincidence events using a 4.4 MeV γ , the main range of neutron energies for our tagged events will be from around 3 to 5 MeV.

In Figure 5.11, we see the neutron scattering and absorption cross sections across a range of energies for hydrogen, oxygen, and carbon. We note that the cross section for scattering with carbon and oxygen varies a lot around energies of 3 to 5 MeV. We can see that the diffusion length of the neutrons will be in proportion to the mean free path of the neutrons through the water (made of hydrogen and oxygen) and the scintillator (made of hydrogen and carbon), where the mean free path will go like $1/n\sigma$ for an elemental density n and a neutron cross section on that element σ . Using the scattering cross sections from 5.11, we can produce a fast neutron diffusion length plot 5.12 using the equation

$$L_{\text{diffusion}} = \frac{1}{n_{\text{O}}\sigma_{\text{O}} + n_{\text{H}}\sigma_{\text{H}}}. \quad (5.5)$$

We extend Bayes's toy MC model of neutron time distributions as follows. We

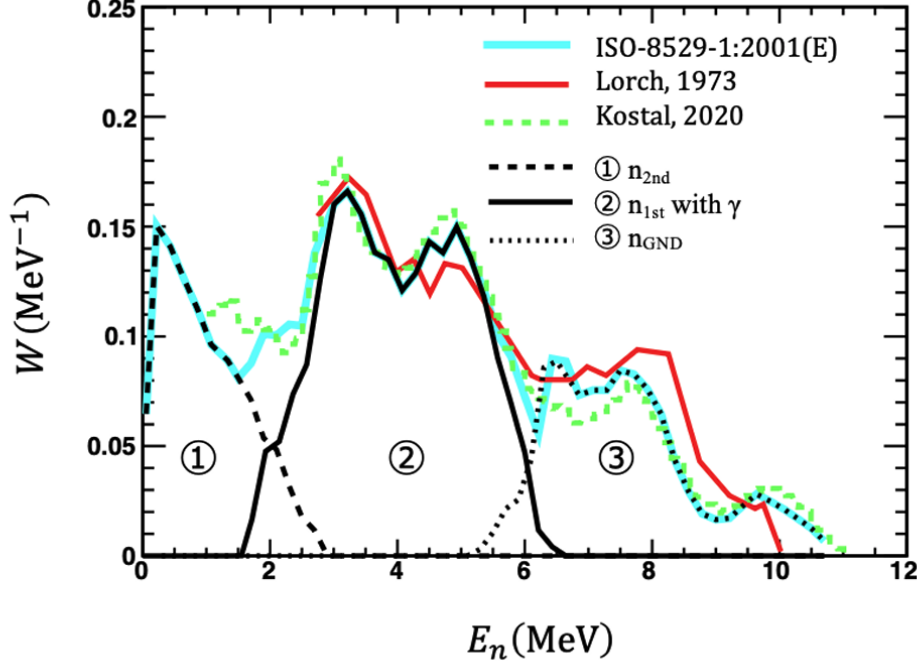


Figure 5.10: Measured AmBe neutron energy spectra. Three regions represent the neutrons produced depending on the carbon nuclei state. 1. ^{12}C was in second excited state. 2. ^{12}C was in 1st excited state. 3. ^{12}C was in ground state. [79]

set AV radius to 6 m, and the source location at 21 cm from the AV, to match the location at which the source was originally deployed. Then we initialize fast neutrons with randomly assigned initial velocity vectors, with a speed appropriately computed for each neutron energy. We then randomly sample over fast neutron and thermal neutron diffusion lengths, and compute a final position and time delay using these diffusion lengths and velocity vectors. Specifically, we initialize three populations of neutrons with energies 3, 4, 5 MeV (corresponding to relevant energies in Figure 5.10), with corresponding fast neutron diffusion lengths of 52, 42, 74 mm, as shown in Figure 5.12. Just as in Bayes toy MC we required several neutron scatters before capture.

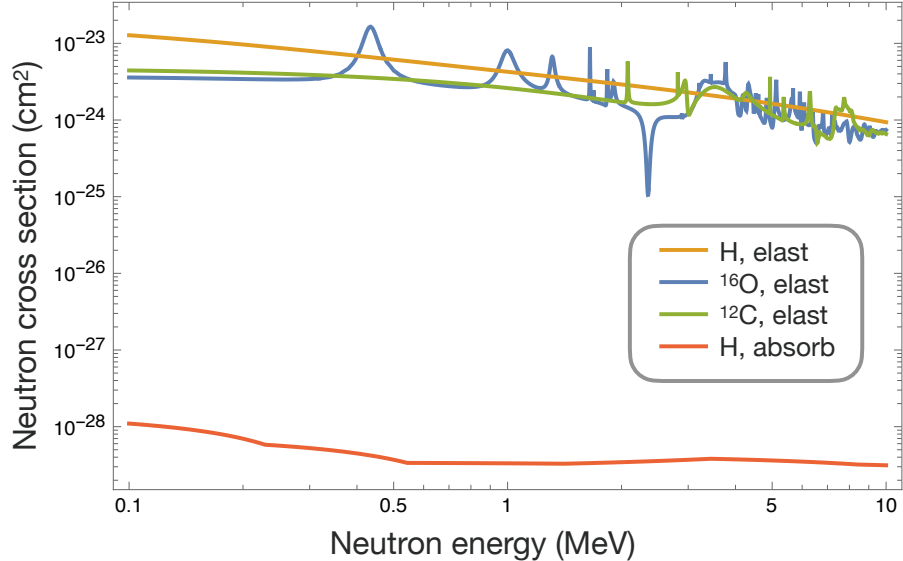


Figure 5.11: The absorption and elastic scattering cross sections for neutrons of varying energies are shown, where cross sections for this plot were obtained from [80]. It is apparent that the scattering cross section neutrons on carbon and oxygen have resonances in the MeV energy region that is of interest for AmBe calibration. These cross sections are used to compute fast neutron diffusion lengths for the toy MC results presented in Figure 5.13. Further studies of this timing feature are underway.

Then we check if event made it to the AV and calculate the time. Figure 5.13 shows the result of our modified toy MC result. For each neutron energy, we see a shift in the resulting timing distribution. Put together, these distributions look similar to the anomalous shape of AmBe delayed event time distribution seen in the data. Hence, one possible cause for the ΔT shape in the data is the fact that the source has been deployed in water outside the scintillator volume and we are seeing two distributions of neutrons: 1) a distribution of fast neutrons that are delayed while scattering in water, as modeled above, 2) a distribution of neutrons that get captured quickly.

This and other ideas for the cause of the AmBe coincident timing "anomaly" are currently being explored. The next steps in the investigation include looking in detail

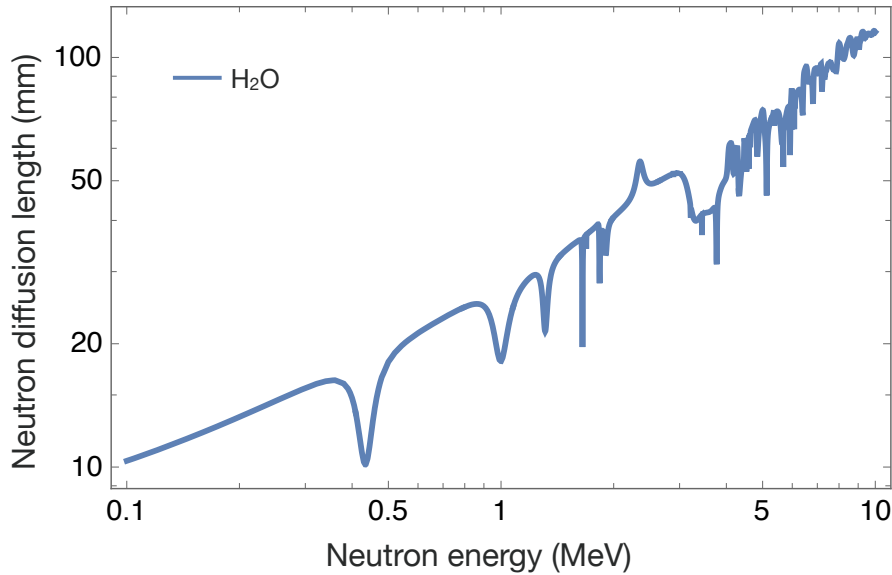


Figure 5.12: Neutron diffusion length in water versus the neutron energy in MeV, using cross sections shown in 5.11.

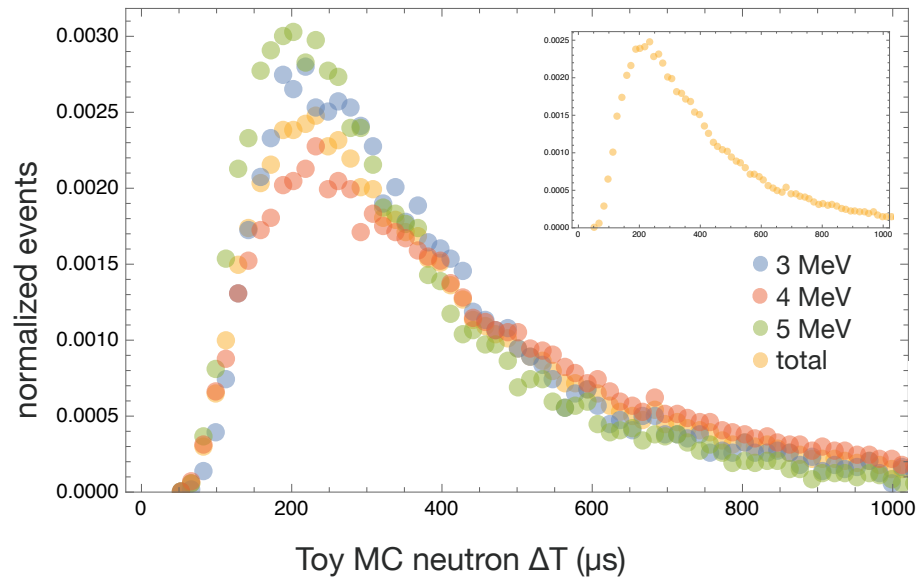


Figure 5.13: The result of the toy MC showing the shift in the neutron capture time for 3, 4, and 5 MeV neutrons.

at the computations and assumptions for neutron diffusion length in water in the GEANT codebase used in our simulations.

5.5 alpha-n IBD classifier

The AlphaNReactorIBD classifier is a code that was developed by Charlie Mills [81], to discriminate between alpha-n backgrounds and signal inverse beta decay antineutrino events. We have already discussed in the previous Sections that the $^{13}\text{C}(\alpha,\text{n})^{16}\text{O}$ background can create prompt events that mimic the annihilation of a positron produced in a signal IBD event. However, there is an observable difference between some alpha-n events and IBD events. Turning to the discussion in Section 5.1 and especially reviewing Figure 5.2, we can conclude that one of the three prompt processes that mimics positron annihilation, should have some measurable differences from positron annihilation. The main difference is that a neutron is relatively slow so while recoiling against multiple protons (process 1 in Figure 5.2) that generates a prompt signal will not necessarily produce photons all at the same location in the detector, since the neutron will often recoil against protons in locations that are more separated in time than a γ ray that Compton scatters at different sites. This difference shows up in the timing of the arrival of the photons at PMTs in SNO+. Also, the scintillation pulse shape from recoiling protons is slower than for electron-like energy depositions from the IBD prompt event. The net result is a different overall time distribution of the detected photons.

There is a convenient tool defined in the SNO+ analysis chain that measures the difference in photon arrival times and patterns compared to expectations for each event, and this variable could also be thought of as measuring how well any amount of

energy deposited on multiple PMTs is reconstructed back to a single location, along with the intrinsic time profile of the emission of scintillation light. This is called the timing residual. The timing residual is not necessarily a measure of how well the event is reconstructed, but it provides information on the residual time of the photon, which comes from the reconstruction of the scintillation pulse shape. Even very well-reconstructed events will have a time residual due to the scintillation pulse shape. The time residual is defined for each photon hit at each PMT. For a given event that has a reconstructed event time t_{fit} , each PMT hit will have a timing residual defined as

$$t_{res} = t_{PMT} - t_{TOF} - t_{fit}, \quad (5.6)$$

where the time of the photon hitting the PMT is t_{PMT} and the time of photon propagation from the reconstructed event vertex to the PMT is t_{TOF} . The time residual thus reveals the intrinsic scintillation pulse shape and in addition, for events that occur at different locations (like multiple recoils off protons), we should expect the scatter in this timing residual to be larger, since the time residual is only based on the event being reconstructed as having happened at a single location.

The AlphaNReactorIBD classifier code uses a log likelihood parameter based on the timing residual, which is defined for a set of Nhits in a given event as

$$\log(\mathcal{L}_{class}) = \sum_{i=1}^{Nhits} \log(P_{class}(t_{res}^i)), \quad (5.7)$$

where the probability of t_{res} being measured by a PMT is given by $P_{class}(t_{res}^i)$, here *class* can be IBD or AlphaN events. The values for this are constructed in terms of a probability density function (PDF) for each class of event; these are determined by

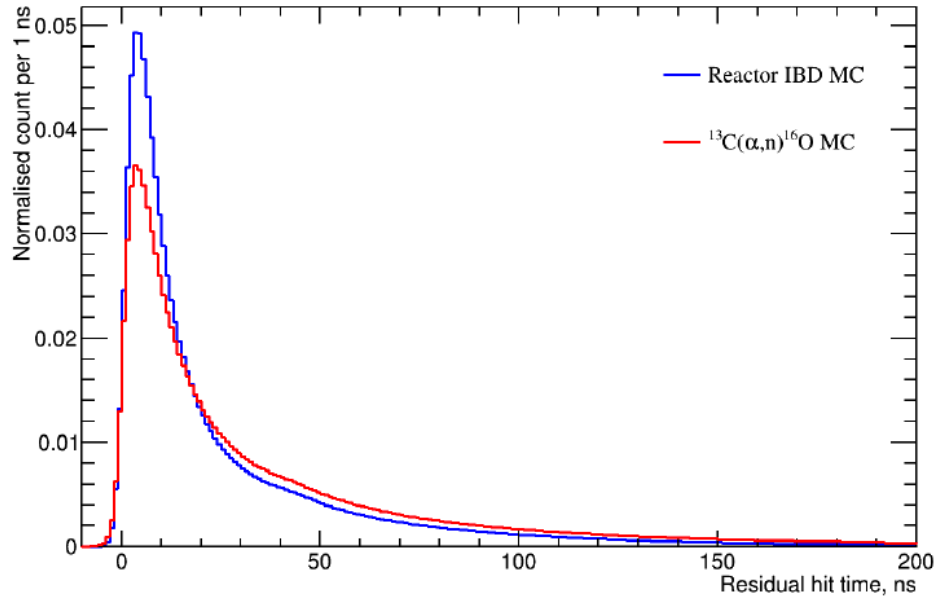


Figure 5.14: The alpha-n and IBD time residual pdfs created by Charlie Mills for the scintillator phase [76]. We can see that for $^{13}\text{C}(\alpha,\text{n})^{16}\text{O}$ the distribution has a broader peak and tail which can be explained by multiple proton scatters over a longer timescale than that of γ energy deposition for prompt IBD events.

Monte Carlo, and where possible tested against calibration data.

Figure 5.14 shows the time residual pdfs for the scintillator phase created by Charlie Mills [76]. It can be seen that the time residual distribution for alpha-n events is broader. This is due to the broader time over which the number of protons are scattered, as well as the proton recoil scintillation pulse shape being slower, compared to that of the γ prompt event for the IBD.

With the preliminary discussion concluded, we are ready to define the AlphaNReactorIBD classifier parameter. Monte Carlo simulations of alpha-n events and IBD events are used to define PDFs for an $\alpha - n$ and an *IBD* probability function in

RAT as shown in Figure 5.14. Then the IBD vs alpha-n classifier parameter for the log-likelihood of the timing residual parameter is defined as the log likelihood ratio:

$$\Delta \log(\mathcal{L}) = \log \left(\frac{\mathcal{L}_{\text{IBD}}}{\mathcal{L}_{\text{on}}} \right) \quad (5.8)$$

From here on we will often refer to this as the classifier result or the IBD classifier value.

5.6 Proton Recoil Classifier Calibration

We have discussed how the $^{13}\text{C}(\alpha, n)^{16}\text{N}$ interactions are one of the largest backgrounds for the antineutrino search. The prompt event can be mistaken for recoiling protons, and this will especially be the portion of the background we are looking to cut out by using the IBD classifier. Actually, this is the biggest motivation for making a likelihood classifier, to exclude residual profiles of recoil proton coincidence events from genuine IBD coincidence events, as explained in Section 5.5. Therefore we need to study carefully the proton recoil spectrum and make sure its timing residual in our Monte Carlo simulations matches the timing residual in calibration data. The best source of recoiling proton IBD-mimic events we have is the AmBe calibration source, since this will create some lower energy neutrons that scatter with protons to make a prompt-like event. Therefore, we will want to select for AmBe calibration events that have prompt events created by recoiling protons, since this will be especially informative for designing and putting in place a log likelihood classifier like the one described above.

To study how the timing of proton recoil events match Monte Carlo, an additional energy cut was applied to the AmBe calibration data of $E_p < 1.7$ MeV to ensure that

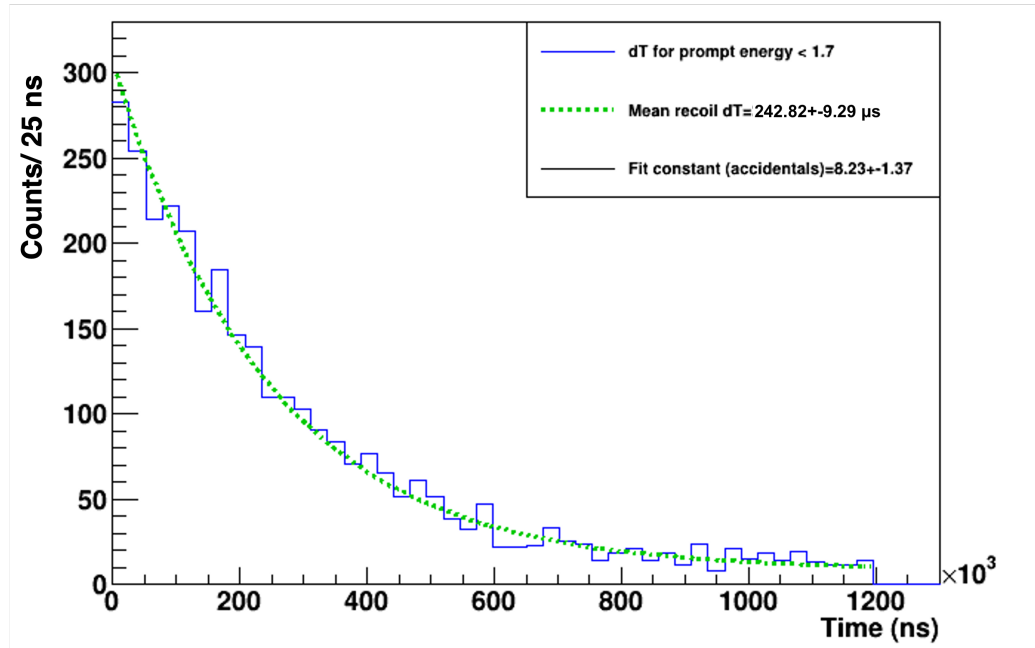


Figure 5.15: Time difference between the prompt and delayed proton recoil coincidence event from AmBe external deployment data, where this data has been cut so that the prompt event has an energy $E_p < 1.7$ MeV, below which most coincidence events should have prompt events from proton recoils. The blue line gives the data histogram as measured from the AmBe source and the green dashed line shows an exponential fit.

proton recoil events dominated the events selected. First, we should check that the low energy AmBe events are behaving as expected, and do not exhibit the as-yet unexplained timing behavior observed in higher energy (with likely inelastic interaction prompt events) AmBe coincidence events discussed in Section 5.4. Figure 5.15 shows the time difference between the prompt proton recoil event and a tagged neutron event. The blue line represents the data histogram and the green dashed line shows the exponential fit. The tagged coincidence ΔT distribution for the proton recoil energy region appears to match with the expected neutron capture time.

With this preliminary check of the ΔT distribution for $E_p < 1.7$ MeV AmBe

concluded, we now turn to a comparison of time residual distribution for AmBe proton recoil events as compared to the distribution generated by Monte Carlo.

In Figure 5.16 we show an example $P_{\text{class}}(t_{\text{res}}^i)$ distribution, including the normalized probability for the timing residual, both for the AmBe data collected in the August calibration run, and for an AmBe MC simulation that matched the detector conditions and settings during the period of detector calibration. We have also plotted the residual difference in probability distributions between these two residuals. We see that there could be a better match between Monte Carlo and data. The variation existing at the tail end of the distribution might be improved by adjusting future iterations of the simulation to better match observed AmBe neutron propagation in the detector. Despite the observed disagreement, for now, we are going to test the existing classifier as it is on a subset of tagged IBD candidate events. Even though it still needs calibration and re-tuning, for the purposes of this thesis analysis and to prepare for future work, it is interesting to see how the classifier performs in its current state.

5.7 IBD Classifier Result

With our IBD classifier defined, and preliminary investigation of the timing residuals concluded, for both AmBe calibration data and Monte Carlo events, we are ready to investigate how the IBD classifier can be applied to a geoneutrino IBD search, and whether using the classifier will result in a more statistically significant measurement of the geoneutrino signal events at SNO+.

At the outset of this discussion, it will be useful to say that we will *not* be using the IBD classifier in our final analysis of SNO+ geoneutrino events, detailed in Chapter

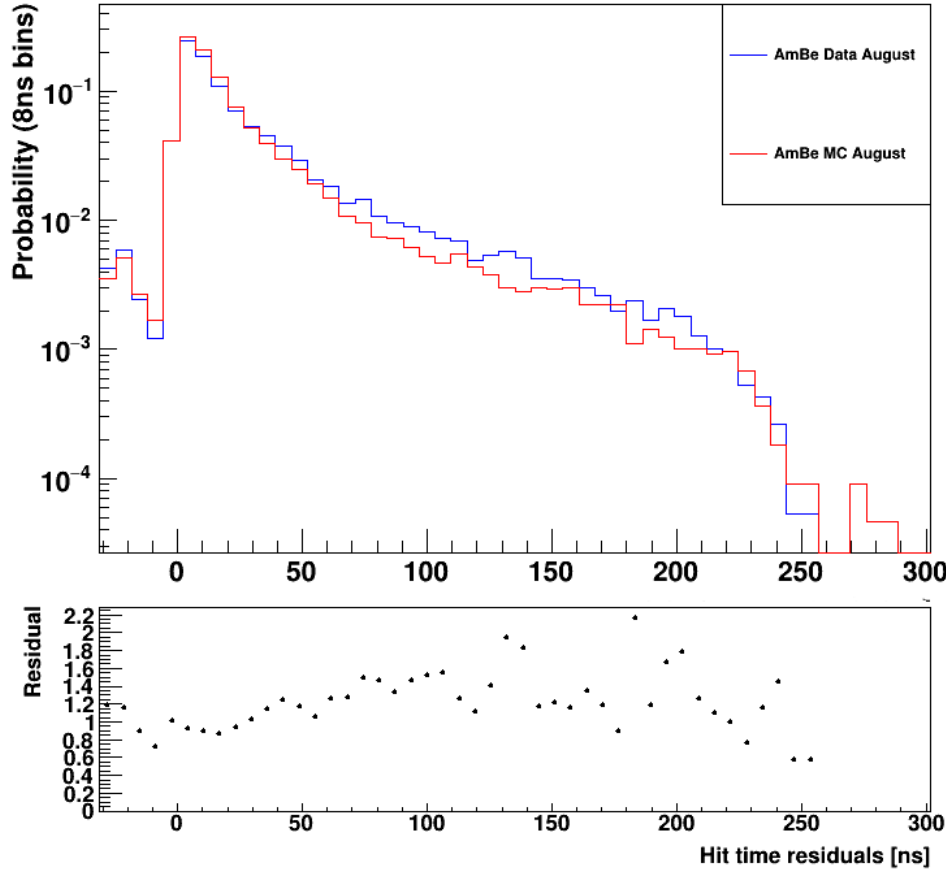


Figure 5.16: The top plot shows the proton recoil time residual probability distribution functions, normalized, with a comparison between August AmBe external deployment data and the MC simulation for detector settings and state during the same period, where the AmBe data was selected to have mostly proton recoil prompt events by applying a cut $E_p < 1.7$ MeV to prompt events. The probability shown on the y-axis is the same probability function that defines the log-likelihood probability parameter in Equation (5.7), which itself is used in the alpha-n versus IBD classifier tested in this section. The MC was produced with RAT version 7.0.9. The lower box shows the residuals of the timing residual PDFs, between the simulation and data.

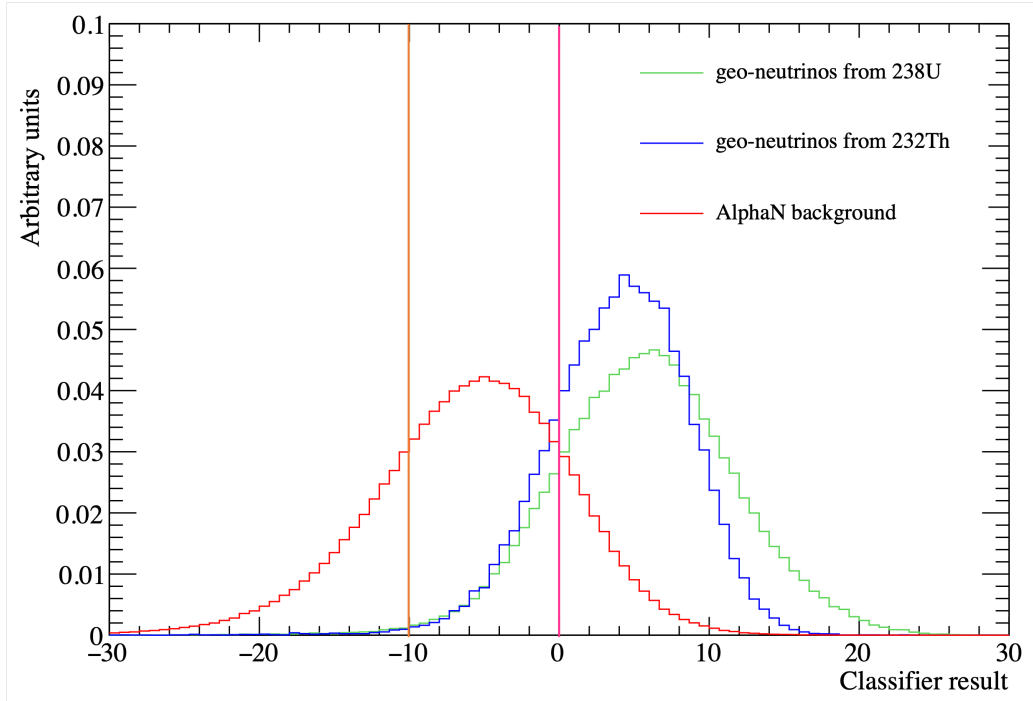


Figure 5.17: The classifier result values are shown for Monte Carlo simulations of α -n and the geoneutrino signals. The lines at -10 (orange) and at 0 (pink) will define the later explored cuts to determine the expected efficiency sacrifice after cuts of classifier result value $CR > -10$ and $CR > 0$ are applied to the full analysis of IBD antineutrino data at SNO+.

6. Our conclusion here will be that cutting on the IBD classifier result value degrades the statistical significance of our geoneutrino results, for the IBD classifier in its present form. Therefore, here we are putting off giving a detailed accounting of all the run parameters, Monte Carlo settings, and especially the cuts applied in this Section, since these are all described in Chapter 6. Here instead we will examine how the IBD classifier performs in its current state, when applied to both Monte Carlo signal/background events, and when applied to the SNO+ data analysis framework that is presented in full detail, without the IBD classifier, in Chapter 6.

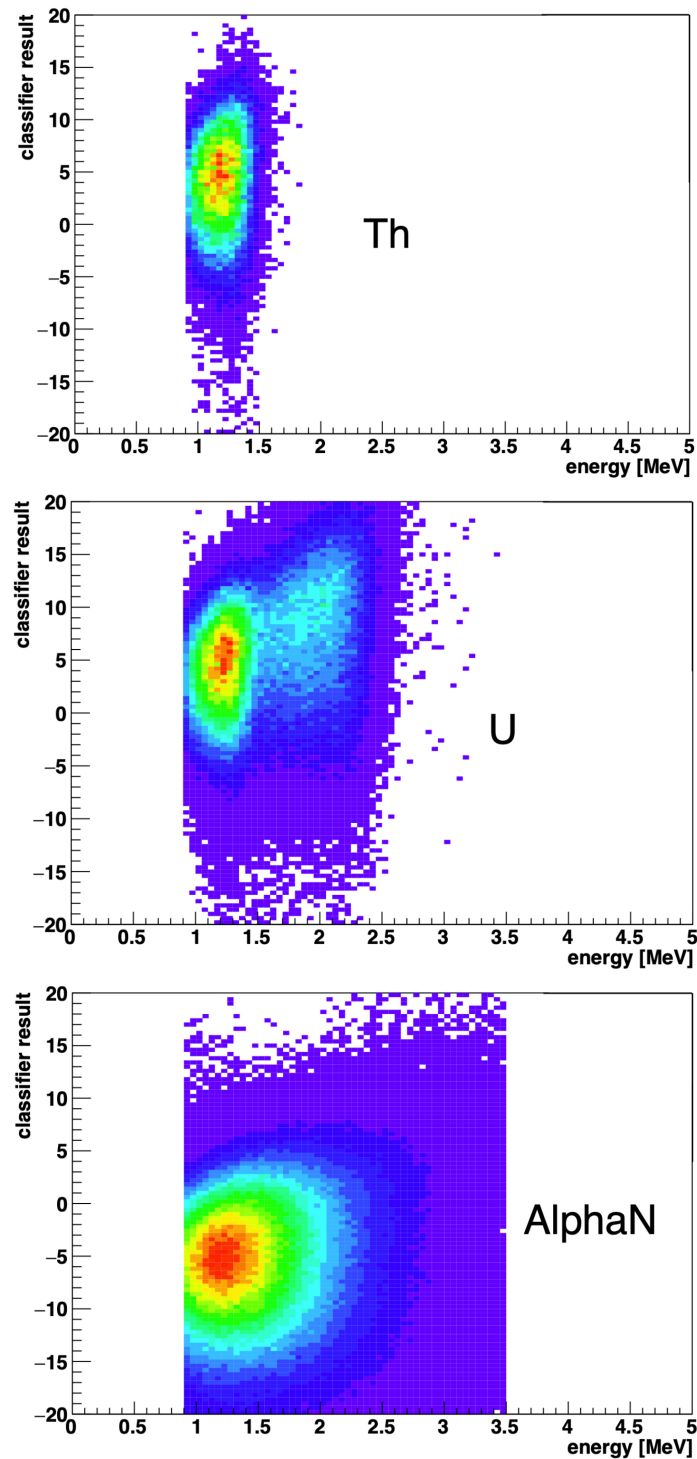


Figure 5.18: Same as figure 5.17 except the classifier result values are shown in a 2-D plot showing coincidence event prompt energies, for MC productions of alpha-n, along with thorium and uranium geoneutrinos. Event density is mapped with a color scale that increases from purple to red. The classifier value has some energy dependence with a notable increase in classifier result for higher energy uranium geoneutrino events.

	Efficiency at -10 cut	Efficiency at 0 cut
U	0.992 ± 0.002	0.835 ± 0.002
Th	0.993 ± 0.005	0.805 ± 0.004
A	0.7505 ± 0.0008	0.1797 ± 0.0003
R	0.993 ± 0.001	0.860 ± 0.001

Table 5.2: The expected efficiency of the MC simulated signal and background statistics for the two proposed classifier cuts, $CR > -10, 0$ where the MC simulated classifier result values are shown in Figures 5.17 and 5.18. In order, the efficiencies for cut events are shown for uranium, thorium, alpha-n, and reactor Monte Carlo data.

To begin, we examine the Monte Carlo obtained classifier result for signal geoneutrinos coming from both uranium and thorium, along with the Monte Carlo classifier result for alpha-n background events. These are obtained for the same detector conditions specified in Chapter 6.

Figure 5.17 shows the timing residual IBD classifier result values, for the distribution of alpha-n background events and geoneutrino events, from both uranium and thorium. Some illustrative IBD classifier cuts one might attempt to use in order to minimize the alpha-n background are indicated, specifically at timing residual classifier result (Equation (5.8)) values $CR > 0, -10$. The same Monte Carlo distributions are shown also in Figure 5.18, but in a 2-D density map so that both the event energies and classifier values can be seen for the distribution of geoneutrino and alpha-n MC events. We can see a slight trend looking at uranium distribution that discrimination worsens at lower energy. We note that the classifier is not nhit normalized, and this effect might be due to the fact that there are fewer photons at lower energies.

We now turn to our expected IBD classifier efficiencies as determined using the Monte Carlo distributions shown in Figure 5.19. The efficiencies obtained after applying IBD classifier result value cuts of $CR > 0$ and $CR > -10$ to the Monte Carlo

data shown in Figures 5.17 and 5.18 (along with reactor MC data that we have not shown for simplicity), are given in Table 5.2. Errors were computed using a Poisson estimate [82].

At face value, the Monte Carlo efficiency results for the IBD classifier shown in Table 5.2 would seem to strongly support implementing one of these cuts in the SNO+ geoneutrino analysis. However, we have found that applying these cuts degrades the statistical significance of the final analysis. The IBD classifier cuts shown in Figure 5.17 and Table 5.2 were tested on an initial SNO+ IBD data subset which had 51 candidate events. The expected number of events after these cuts are applied, according to the Monte Carlo simulations, would be 47.2 (9.9 geo, 24 reactor, 12.5 alphaN) for the $CR > -10$ cut and 33.8 (8.3 geo, 21.5 reactor, 4 alphaN) for the $CR > 0$ cut. We see in Figure 5.19 that the total number of events surviving these cuts are 39 and 23 events, respectively. From the fit lines in the figure we can clearly see that, instead of removing alphaN events we seem to sacrifice geoneutrino events, which is especially visible in the second fit where we cut at 0. For the zero cut, we result in a fit which gives us only alphaN and reactor events. So the classifier cut, removes more events than expected, resulting in a fit that removes the desired geoneutrino events. We conclude that it is likely the IBD classifier could be improved for the geoneutrino search, through re-examination of the Monte Carlo simulation chain, especially for low energy IBD events with energies associated with proton recoil prompt events. One of the possibilities of a bad performance of the classifier for the current data is that the classifier PDFs need to be coordinated with new optics, which have changed since the original pdfs were created, because of the addition of PPO. Therefore it is important to adjust the proton recoil MC time residual profiles

to match the data taken using AmBe calibration source as we have demonstrated the poor agreement between the current data and the MC simulation. Improvements and recoordination of the classifier for the next iteration of data processing have been undertaken by SNO+ collaborator James Page. He is looking into making the adjustments to account for changing optics, as well as adjustments to the PDFs used for the likelihood ratio calculation.

In this Chapter, we studied the $^{13}\text{C}(\alpha,\text{n})^{16}\text{O}$ background at SNO+, along with AmBe calibration data, which is the primary calibration data used to explore the response of the SNO+ detector to IBD antineutrino events, but also especially alpha-n backgrounds, which will be very similar to neutrons the AmBe source produces. After studying AmBe calibration data, noting an interesting deficit of AmBe events around $\Delta T = 100$ microseconds for coincident events with 4 MeV prompt energies, we verified that lower energy AmBe events relevant for calibration of proton recoil prompt event alpha-n backgrounds followed the expected ΔT distribution. The use of an IBD timing residual log likelihood classifier variable to improve alpha-n background rejection was studied, and it was found that the event selection efficiencies predicted from Monte Carlo simulation do not match efficiencies found when applying IBD timing residual classifier cuts to data. We concluded that more calibration of the classifier and Monte Carlo simulations at low energies may be necessary in order to effectively use the IBD classifier in future geoneutrino studies. For future work the deployment of AmBe source at various locations could be useful to create proton recoil time residual pdfs at different locations. This way we could check if there is an effect on the distributions depending on the position, as event reconstruction can be affected by detector geometry as we have discussed previously. The MC simulation

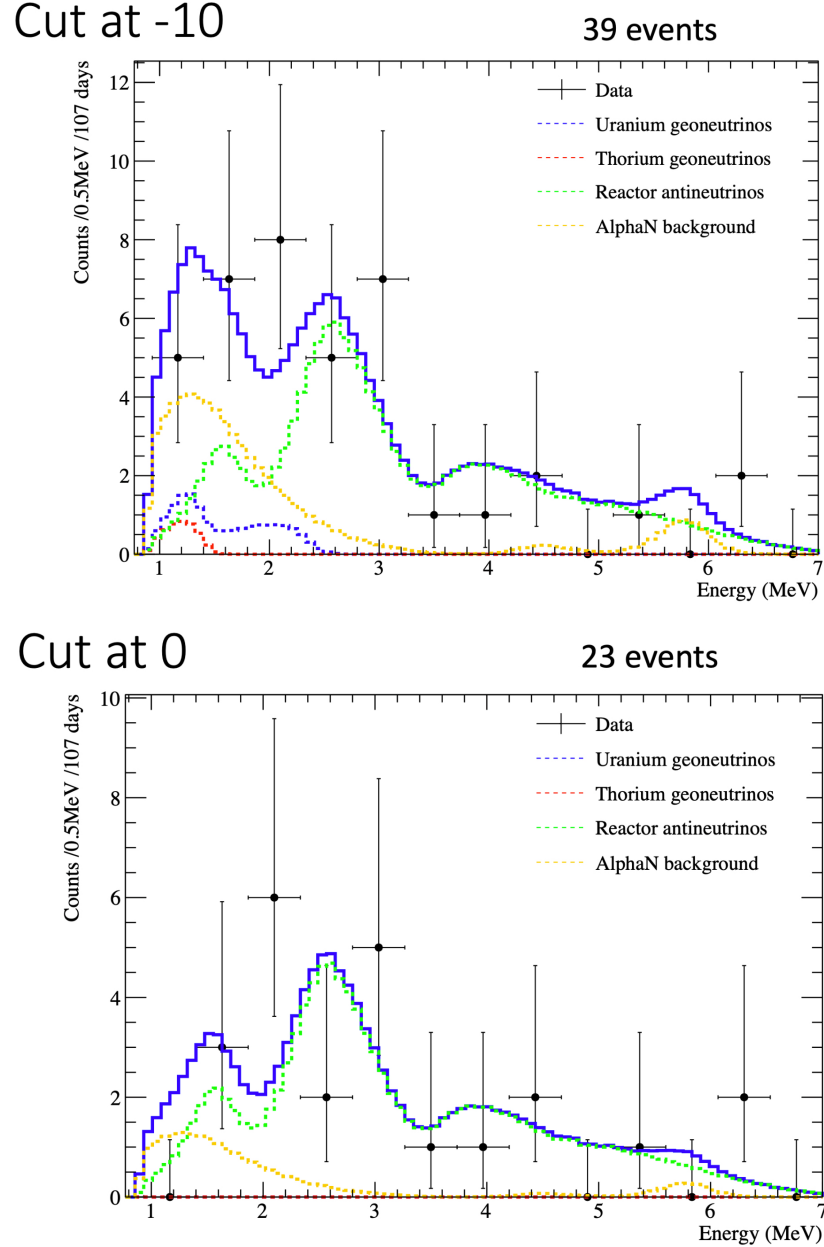


Figure 5.19: Best fit fluxes are shown for geoneutrinos, reactor antineutrinos, and alpha-n backgrounds, after a classifier result value cut of $CV > -10$ and $CV > 0$ is applied to 107 days of data. See Equation (5.8) for the classifier definition. For a full accounting of the cuts and data analysis presented here, see Chapter 6. The expected signal efficiency for both IBD classifier values shown, -10 and 0 , are well below the efficiency predicted from Monte Carlo simulations shown in Table 5.2.

of proton recoils and their time residual profiles then need to be adjusted to match the calibration data with the tuned time residuals applied as new pdfs for the IBD alphaN classifier. We now proceed to the main result of this thesis, the search for geoneutrinos at SNO+.

Chapter 6

The Geoneutrino Search at the SNO+ Experiment

This Chapter presents the main result of this thesis, the search for geoneutrino events at the SNO+ experiment, using 123 days of SNO+ data collected from 2022-2023. The first evidence for a geoneutrino signal at SNO+ is demonstrated. After introducing the dataset, we detail relevant backgrounds, provide a full account of event selection and the coincidence tagging algorithm, and finally, present likelihood fits, from which we determine that there is evidence for a geoneutrino flux at SNO+

6.1 SNO+ Geoneutrino Dataset Selection

We begin with a review of data handling procedures at the SNO+ experiment. To ensure the data used in the analysis is high quality and trustworthy, all data runs first go through quality checks performed by the run selection team. A run is defined as an hour-long segment of data with a unique run ID and contains information related to the detector's status, alongside the data taken. Each run goes through a set of checks to determine the quality of the run and gets assigned a quality label such as "gold", "silver", or "bronze".

Table 6.1 summarizes the broad criteria of assigning physics runs to a specific

	Gold	Silver	Bronze
Run type	Physics	Physics	Physics
Minimum run length	30 min	30 min	15 min
Number of crates	All ON	Maximum of 1 OFF	Maximum 2 OFF
Minimum PMT coverage	70%	70%	70%
Minimum panel coverage	80%	75%	70%
OWLs	ON	ON	ON

Table 6.1: An abbreviated list of run selection criteria for “gold”, “silver”, and “bronze” run lists.

quality label, however, there are about 50 individual checks to determine if the data is suitable for analysis. The checks range from verifying the absence of electronics malfunctions, PMT breakdowns, loss in data during transfer from a data buffer failure, interruptions to the network, and even the noise created in the DAQ and detector when personnel enter the detector deck to perform a maintenance task.

The dataset used for the analysis in this thesis will be taken only from “full scintillator fill” runs, and is further limited to selecting only from the “gold run” data quality list. The set that is analyzed contains runs from the 300000 – 307612 run range, which spans from April 29th, 2022 to January 9th, 2023. The time duration of these runs is 123 days and 14 hours. As cuts are applied to remove backgrounds detailed below, this effective runtime will be reduced to 110.8 days. Data cleaning will also have a relatively small lifetime correction compared to the already applied cuts; it is not included in this analysis but would need to be included in further work.

6.1.1 Event Reconstruction

To reconstruct the position, time, and energy of events SNO+ applies multiple fitter algorithms. These are adapted and changed depending on the phase of the experiment and the status of the detector. For example, the water phase has water fitters, which

focus on reconstructing the event using Cherenkov light, whereas the scintillator phase has scintillator fitters, which focus on the scintillation light. Event fitters take note of the detector state, for example, by accounting for periods of data taking where one or more crates were missing.

First, the events are fit for the initial time and position. Time and position are reconstructed using the timing information of triggered PMTs and the order in which they are triggered. Using the photon arrival times the position can be reconstructed. For example, the PMTs that are closer to the event get triggered before the PMTs that are further away from the event. The SNO+ RAT includes LightPath fitter which calculates the arrival times using straight path trajectories from the point source to the PMTs. Then a likelihood is calculated and compared to the MC modelled PDF, and the fitter finds the most likely position and time of the event vertex.

Energy is reconstructed from the number of triggered PMTs (NHit). NHits is defined as the number of PMTs that crossed the trigger threshold in an event and have their time and charge information read out. In a similar fashion, the MC is produced to see how NHits scale for different energy events. Generally, the scaling is expected to be approximately linear. However, linearity weakens at higher energies, because of the PMT readout. Specifically, if PMTs have multiple photons incident upon them, and register multiple hits are counted as just one NHit. The charge information could in principle recover this multi-photon information, however, SNO+ does not tend to use the charge information. Instead, the main energy fitter called EnergyRThetaFunctional applies a correction factor to NHits, trying to account for the multi-hit photons in the event. In addition, depending on the position of the event, due to detector geometry, photons can get reflected, scattered, or attenuated.

These processes affect the energy reconstruction and additional corrections need to be applied for certain datasets. In the next subsection, we'll discuss the correction which was applied for the geoneutrino analysis.

6.1.2 Position Dependent Energy Correction

As previously mentioned the agreement between data and simulation for reconstructed energy at the center of the scintillator volume is better than near the edge of the AV. Our antineutrino analysis relies on being able to place energy cuts when selecting coincidence events. We also require accurately measured energy values, since we use the measured prompt energy spectra in our final fit of geoneutrino, alpha-n, and reactor events. One way to avoid the issue of poor energy resolution near the edge of the AV would be to reduce the fiducial volume. However, due to low statistics in our geoneutrino analysis, we need as large a volume as possible.

Since we would like to use the entire SNO+ volume including the edge of the AV, it would be best to directly calibrate energy reconstruction by placing a calibration source like AmBe inside the SNO+ detector. Thus far, such a source has not been deployed. Despite this, SNO+ has used tagged $^{214}\text{BiPo}$ events for energy calibration, taking advantage of the data periods where Rn ingress resulted in sufficient rates. These events were used to calculate energy correction factors for the AV up to a 5.7 m radius. The calculation involved creating tagged ^{214}Bi energy distributions sampled over discrete volumes inside the detector, then comparing these distributions with the MC of $^{214}\text{BiPo}$ events. From the measured $^{214}\text{BiPo}$ energy distributions, a scaling factor as a function of position was developed, which can be applied to all reconstructed energies in simulation and data. The original energy scaling for a

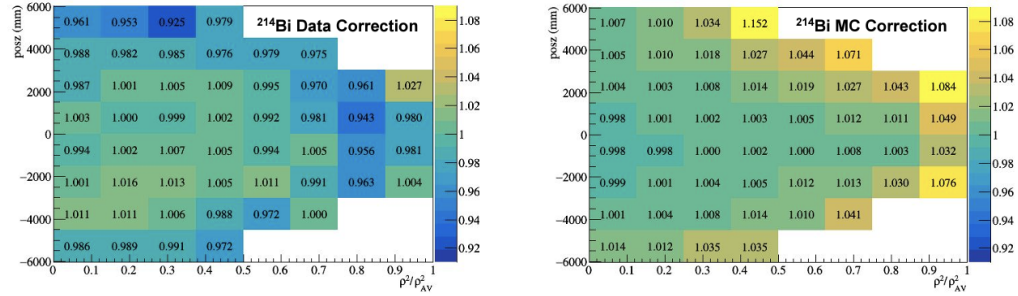


Figure 6.1: Energy correction using ^{214}Bi Po tagged events. Binned correction map for tagged ^{214}Bi events. The left panel shows the correction map that can be applied to data, and the right panel shows the correction for the MC events [84].

partially filled scintillator was developed by Iwan Morton-Blake [83], then adapted to full fill scintillator volume by Anthony Zumbo [84]. Figure 6.1 shows the binned correction map for tagged ^{214}Bi events. The left panel shows the correction map that can be applied to data, and the right panel shows the correction for MC events. This energy correction map was applied to the geoneutrino analysis in this thesis. A good illustration of the effect of the correction can be seen in Figure 6.2, where the correction was applied to AmBe data, and compared to simulation. The left panel shows reconstructed AmBe energy peaks before the correction, compared to MC, and the right panel shows the reconstructed energy peaks after the correction was applied.

6.1.3 Target Protons

Before proceeding to a discussion of backgrounds, we compute the expected number of target protons in the SNO+ experiment. As discussed in Section 3.3 the antineutrinos which we detect through the IBD process interact with protons (aka hydrogen). Therefore we have to know the number of target protons available at the SNO+ fiducial volume. For this we have to know the composition and the density of the liquid

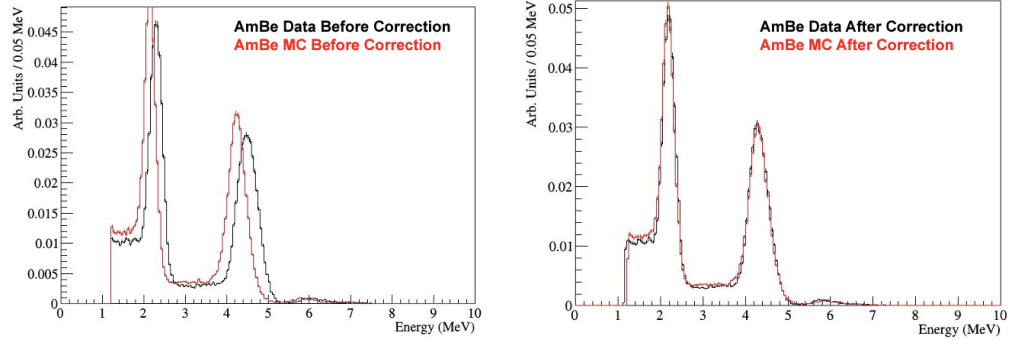


Figure 6.2: The before (left) and after (right) of applying energy correction to AmBe data for events at $5.2 < R < 5.7$ m. Figure made by Tanner Kaptanoglu.

scintillator. The majority (99.8%) of the current SNO+ volume is currently filled with linear alkylbenzene (LAB) [85], which has a chemical formula



where the final component of this formula counts the number of carbon atoms attached to the benzene. The remaining 0.2% of the SNO+ volume is filled with PPO fluor, which has a chemical formula



In more detail, the chemical composition of the linear alkylbenzene at SNO+ has been assessed to 0.1% precision by CEPSA Quimica for carbon chain numbers $n = 9 - 14$ [85, 86]. Specifically, LAB with $n = 9 - 13$ carbon chains were found to compose fractions (frac_n) of the LAB mixture,

$$(n, \text{frac}_n) = (9, 0.009), (10, 0.181), (11, 0.456), (12, 0.303), (13, 0.051) \quad (6.3)$$

in the LAB mix assessment [86]. Cross-checks on these values, obtained by assessing the combined fraction of $n = 9$ and $n = 10$ LAB (and other similar combinations), agreed with individual measurements being accurate at the 0.1% level [86]. The temperature of the cavity was kept at a temperature of 13°C, at which temperature it has been determined that the density of the LAB in SNO+ is $\rho_{LAB} = 0.865 \pm 0.001$ g/cm³, while for these values the total density of PPO fluor and LAB is $\rho_{LAB+PPO} = 0.867 \pm 0.001$ g/cm³ [85].

To compute the number of protons in hydrogen atoms in SNO+, for use in the computation of inverse beta decay interactions, we multiply the acrylic vessel volume (a sphere with radius R_{AV} of 6 meters) by the density, and appropriately weight for each LAB n chain group using the fractions above. For each fractional LAB component with n chains, the number of protons is

$$N_{\text{protons}} = \frac{(2n + 6)m_H \times \text{frac}_n}{(n + 6)m_C + (2n + 6)m_H} \times \frac{4\pi\rho_{LAB}R_{AV}^3 N_{Av}}{3m_H}, \quad (6.4)$$

where $m_C = 12.00$ amu and $m_H = 1.00784$ amu, N_{Av} is Avogadro's number. We add the protons from the PPO fluor using a similar calculation. Using the above uncertainties on the LAB + PPO density and the 0.1% uncertainty on each LAB component to compute a total uncertainty, we find that the number of protons is $N_{\text{protons}} = 5.700(\pm 0.014) \times 10^{31}$.

6.2 SNO+ Antineutrino IBD Backgrounds

In this section we detail backgrounds and the cuts used to reduce backgrounds for geological antineutrino inverse beta decay detection at SNO+.

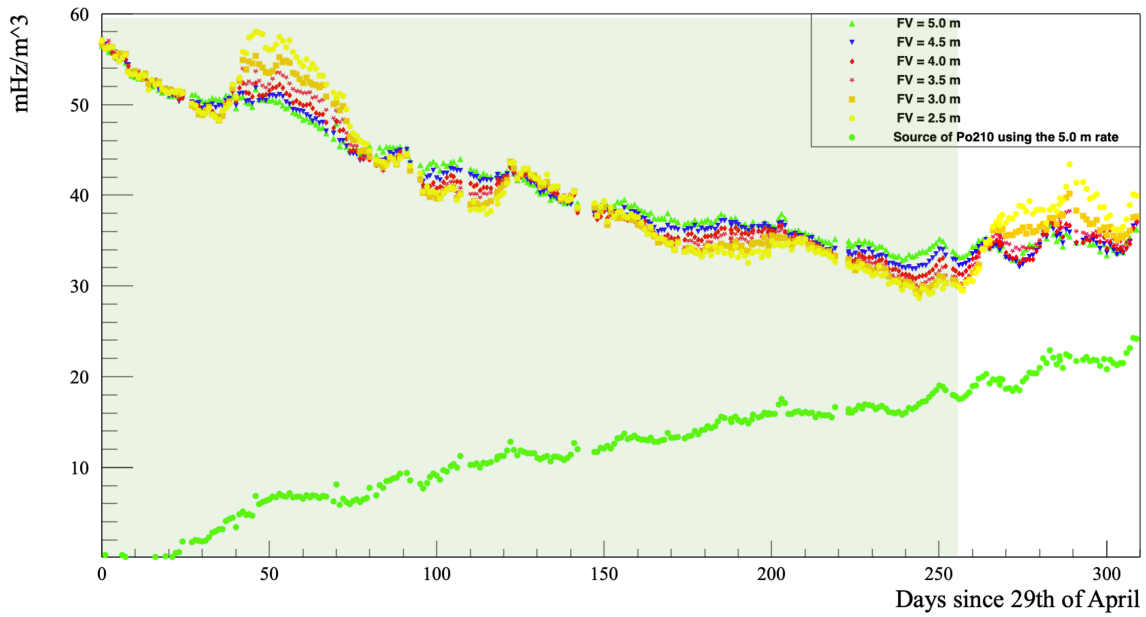


Figure 6.3: The measured ^{210}Po rate within detector fiducial over the data taking period from 29/04/22 to 5/3/23 (shaded in green). Each rate measurement shown above is normalized to a fiducial volume for the run, as indicated. Figure by V.Lozza, created as part of an internal SNO+ document.

6.2.1 Alpha-N

As discussed in Chapter 5, $^{13}\text{C}(\alpha, \text{n})^{16}\text{O}$ is one of the most troublesome backgrounds for antineutrino detection. The expected number of alpha-n events can be calculated from the measured ^{210}Po rate, since as shown in Section 5.1 and explained in Chapter 5, ^{210}Po will be the most prevalent source of alpha-n backgrounds to IBD in the SNO+ detector.

Figure 6.3 shows the measured ^{210}Po rate at different fiducial volume (FV) levels for the period of 29/04/22 to 5/3/23. The ^{210}Po rate was measured by Serena Ricceto by fitting observed events at the energy of ^{210}Po decay. The expected rate can be calculated using equation 6.5, where R_{210Po} is the fiducial polonium decay rate in

units of [event/h/m³],

$$N(\alpha, n) = R_{^{210}Po} \times A(\alpha, n) \times T, \quad (6.5)$$

and the quantity $A(\alpha, n)$ defines the neutron yield in a medium, with T being the time duration of interest. From the data presented in Figure 6.3 we have determined the ^{210}Po rate to be $45 \pm 15 \text{ mHz}/\text{m}^3 = 162 \pm 54 \text{ events/h/m}^3$, by taking the average value for the time period used in our geoneutrino search dataset, as outlined in Section 6.1, and setting a generous uncertainty to the lowest and highest values of the rate within the time period. The fiducial volume for our data analysis is $V_{R=5.7 \text{ m}} = 776 \text{ m}^3$. Daya Bay measured the $A(\alpha, n)$ rate induced by a given polonium rate to be $(5.75 \pm 0.41) \times 10^{-8} \text{ neutron}/\alpha$ [87]. We use this to determine the alpha-n rate at SNO+ by converting according to the relative abundances of ^{13}C in Daya Bay as compared to SNO+. The Daya Bay scintillator has ^{13}C density of $3.84 \times 10^{20} \text{ cm}^{-3}$ [88]. Adjusting for the different ^{13}C density of the SNO+ liquid scintillator of $4.19 \times 10^{20} \text{ cm}^{-3}$ [89], we arrive at the total alpha-n yield per polonium decay at the SNO+ experiment,

$$A(\alpha, n) = (6.27 \pm 0.44) \times 10^{-8} \text{ neutron}/\alpha. \quad (6.6)$$

The duration of the dataset used in the analysis is $T = 2659$ hours. Taken together, these values imply the total alpha-n background event expectation should be $N(\alpha, n) = 21.4 \pm 8.5$ events. Using the IBD analysis cuts on our alpha-n Monte Carlo, which will be detailed in Section 6.3, we find the expected efficiency for detecting alpha-n events, not including the fiducial volume cut, is $81.190(\pm 0.083)\%$. We note that the fiducial volume was already accounted for in the expectation calculation

provided above. Applying the Monte Carlo-determined detection efficiency,

$$N(\alpha, n) = 17.4 \pm 5.2 \text{ events}, \quad (6.7)$$

where this is the final alpha-n background expectation after IBD antineutrino analysis selection cuts are applied, as will be described in Section 6.5.

6.2.2 Atmospheric Neutrinos

Atmospheric neutrinos are created from the decay of particles produced in the atmosphere through cosmic-ray interactions. These neutrinos usually fall into a higher energy range than the expected signal region investigated in this thesis [90]. However, of some relevance to our antineutrino inverse beta decay analysis, atmospheric neutrinos can interact with the scintillator through neutral current and charged current interactions with ^1H , ^{12}C and, ^{13}C . Some of these interactions will produce neutrons, which can mimic the prompt and delayed signal, in much the same way a neutron produced in an alpha-n interaction can mimic the prompt and delayed signal, details in Chapter 5.

Calculations and predictions of the atmospheric neutrino events falling within antineutrino coincidence cuts in the partial fill phase were conducted and presented by Cindy Lin in the SNO+ internal document [91]. The calculations were made using the GENIE neutrino Monte Carlo generator [92]. The total expected number of events per year for partial fill scintillator volume was $(1.5 \pm 4.1) \times 10^{-2}$, which is orders of magnitude below the expected signal and other backgrounds for the geoneutrino IBD analysis, therefore this background is treated as negligible for the IBD analysis presented in this thesis.

6.2.3 Reactor Antineutrinos

Significant numbers of antineutrinos are produced in radioactive decays occurring in nuclear reactors, resulting from the fission processes in nuclear fuel. The primary isotopes in the nuclear fuel that produce antineutrinos are ^{235}U , ^{238}U , ^{239}Pu , and ^{241}Pu . Fission from these isotopes produces a series of beta decays. The energy spectrum of the emitted antineutrinos differs for each decaying isotope and has a corresponding different thermal power released per decay. To account for the total energy spectrum at SNO+, we need to obtain the relative fuel composition of the reactor cores for different reactor types and produce a weighted sum of the contributions. For the prediction of the reactor antineutrino rate at SNO+, we use the same method as Huber & Mueller model to calculate the total antineutrino spectrum depending on the time evolution of reactor thermal power output and fission fraction of the fuel isotopes as described in [93]. A part of this calculation uses the Huber & Schwetz model to describe the antineutrino emission for a given isotope per unit energy given as

$$n(E_{\bar{\nu}}) = P_{th} \sum_i^{N_{isotopes}} \frac{f_i n_i}{\epsilon_i}, \quad (6.8)$$

where P_{th} is the thermal power, f_i is the fuel isotope i fission fraction, ϵ_i is the energy emission per fission, n_i is the number of antineutrinos per fission per unit energy.

Due to the fact that fuel composition is different for different types of nuclear reactors, the SNO+ RAT considers three main designs:

- PHWR - pressurized heavy water reactors
- PWR - pressurized water reactors

Design	^{235}U	^{238}U	^{239}Pu	^{241}Pu
PHWR	0.52	0.05	0.42	0.01
PWR	0.568	0.078	0.297	0.057
BWR	0.568	0.078	0.297	0.057

Table 6.2: The fuel isotope fission fractions for the modeled reactor designs in RAT. Representative fission fraction data for PWR and BWR was taken from [94] and data for PHWR were given in private SNO+ communication with Atomic Energy of Canada (AECL) in 2013.

- BWR - boiling water reactors

All other reactor designs that are not one of the three mentioned are modeled in SNO+ code as PWR reactors. Table 6.2 shows the relative fission fraction of each isotope amount in the fuel for different reactor types. Data for PWR and BWR are representative fission fractions from [94] and data for PHWR fission fractions were given in private SNO+ communication with Atomic Energy of Canada (AECL) in 2013. PHWR reactors are typically re-fueled continuously resulting in steady-state fission fractions given in Table 6.2.

The SNO+ RAT Reactor tool computes the IBD event rate for each core using the information of the designed power output, energy emitted per fission, distance from the detector, emitted antineutrino spectrum, and IBD cross section, then integrates over a database of all nuclear reactor cores around SNO+ using the Huber & Schwetz model, Equation 6.8. To populate the database of nuclear reactor cores, the RAT reactor scaling tool uses the REACTOR_STATUS tables which are updated regularly using the electrical power from the Independent Electricity System Operator, Generator Output Capability Month Report [95] and the thermal power from International Atomic Energy Agency, Power Reactor Information System database [96] to calculate the scaling factor, which is then used to rescale the reactor antineutrino MC

rate output. This produces the number of antineutrinos for each core, which depends on the specific time value the simulation is called, corresponding to the reactor core power at the called time. If there is a reactor shutdown or some other change in the closest reactor core power outputs, this is accounted for in the REACTOR_STATUS tables.

The antineutrino flux at SNO+ is dominated by the three nearest reactors at the Bruce, Darlington, and Pickering power plants. Approximately 60% of the flux comes from these nearest reactors. They are all Canada Deuterium Uranium (CANDU) reactors, which are a PHWR design type. Figure 6.4 shows the expected antineutrino spectrum for each CANDU reactor fuel isotope, as well as the total sum of the isotopes.

The oscillation parameters of $\Delta m_{21}^2 = 7.53 \times 10^{-5} \text{ eV}^2$ and $\sin^2 2\Theta_{12} = 0.861$ [98] are usually used as a default value for prediction and for SNO+ RAT event simulation. One scientific goal of the SNO+ experiment is to use reactor spectrum measurements to obtain an independent measurement of the neutrino mass mixing parameter Δm_{21}^2 .

Figure 6.5 shows the simulation of the expected antineutrino spectrum at the SNO+ experiment, focusing particularly on reactor contributions.

For the geoneutrino analysis that follows in Section 6.5, we will fit the reactor spectrum, since reactors make a much larger contribution to the total antineutrino spectrum than the geoneutrinos. In order to test whether fixing the Δm_{21}^2 to its measured value will affect our fits, we examine here how the shape of the reactor energy spectra changes with Δm_{21}^2 , and later we will present fits with two different values for Δm_{21}^2 . For comparison with the fit later described in this thesis Section 6.5, here we present two separate probability density functions (PDFs), which have been

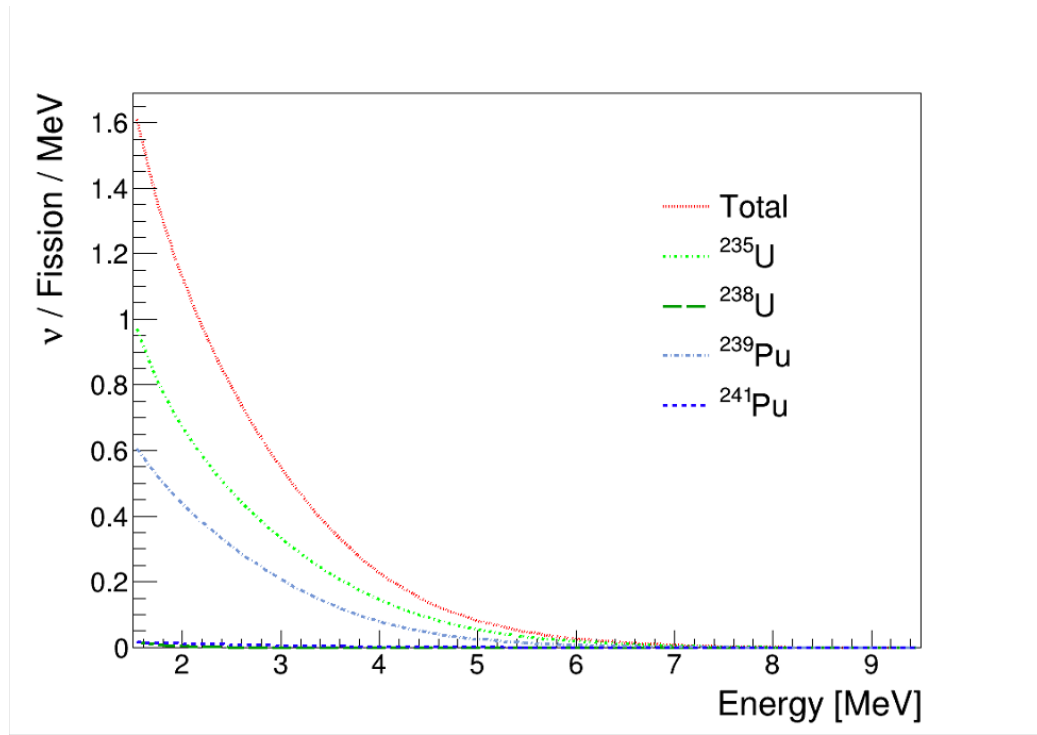


Figure 6.4: Energy spectra of the emitted antineutrinos from each isotope of CANDU nuclear fuel accounting for the fission fractions presented in Table 6.2. These are combined with a detailed reactor Monte Carlo code to predict the total reactor antineutrino rate versus energy plot shown in Figure 6.5. Figure from [97].

produced by modifying the default settings in the RAT reactor oscillation tool. The value of $\Delta m_{21}^2 = 5.0 \times 10^{-5}$ eV² was chosen to produce the second PDF, to see how the spectral shape changed as compared to the $\Delta m_{21}^2 = 7.53 \times 10^{-5}$ eV² value preferred by global fits [20]. The value of $\Delta m_{21}^2 = 5.0 \times 10^{-5}$ eV² was chosen because some solar neutrino oscillation fits prefer a fit closer to five as can be seen in Super-Kamiokande solar fits [99]. Figure 6.6 shows how this variation of the parameter changes the overall shape of the spectrum, as presented in a PDF of resultant antineutrino energies. We create these two PDFs to be able to check how the different fixed Δm^2 parameter values in the fit affect the extracted geoneutrino rate.

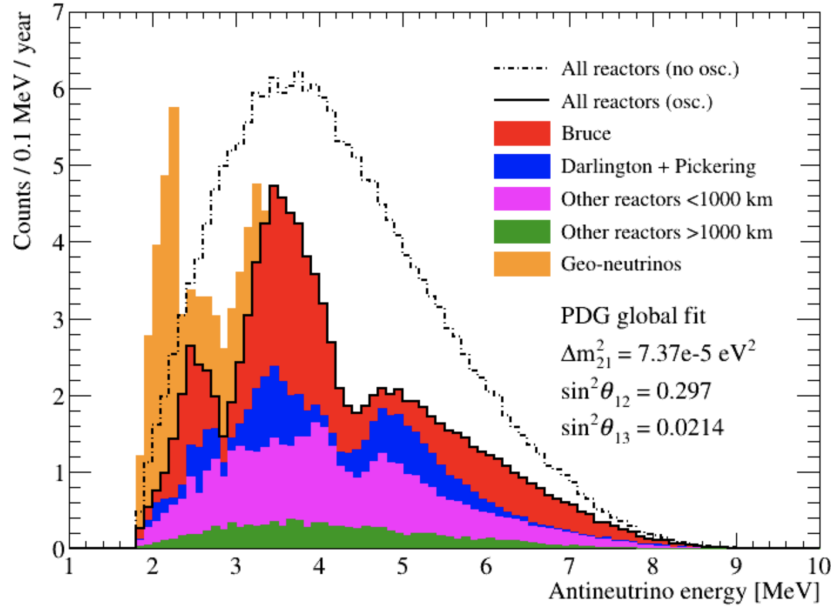


Figure 6.5: The MC simulation of expected antineutrino spectrum for SNO+, particularly focusing on showing individual reactor contributions. Here the geoneutrino rate is arbitrary and used for illustration purposes. Shown are the contributions from the nearest reactors compared to the reactors further away from the experiment site. Plot made by Stefan Nae from an internal SNO+ document.

Although the rate of reactor antineutrinos will not be one of the quantities determined in the final fit presented in this analysis, we will not claim to be measuring the reactor antineutrino rate here, nor are we fitting the oscillation parameters, since alongside this analysis there is a dedicated parallel analysis measuring reactor neutrinos. Nevertheless, we need to fit the reactor rate to extract the geoneutrino rate. For that reason we cannot constrain the reactor rate in the fit, only the oscillation parameters. Just as a cross check, we have computed a signal prediction estimate using the Monte Carlo production campaign that was undertaken in SNO+ for reactor antineutrino IBD events. This official MC production campaign simulated 30000 times the

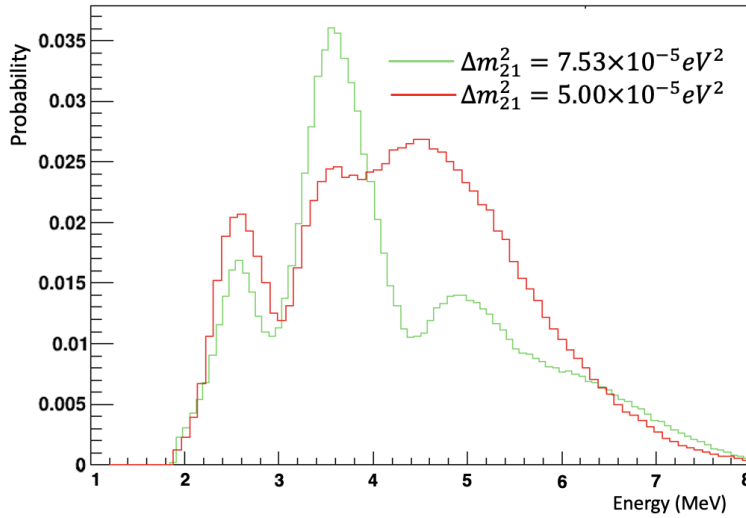


Figure 6.6: The probability density functions of the prompt event energy spectrum from the reactor antineutrino prediction at SNO+ using different Δm_{21}^2 values. This can be compared to the two different geoneutrino IBD fit results presented in Section 6.5, which use these PDFs to determine how the fit changes with variation of Δm_{21}^2 .

expected reactor neutrino flux for the run range of this thesis analysis, incorporating nominal reactor power. The higher statistics were simulated to get better PDFs for the fit of the signal. The RAT-TOOLS scaling code [100] takes into account the actual reactor powers from publicly available databases [95] [96] as well as oscillates the flux accounting to the distances of the list of reactors using $\Delta m_{21}^2 = 7.53 \times 10^{-5} \text{ eV}^2$, [98] as a default value. The official simulation was undertaken using the same 124 days of data detailed in Section 6.1. Using the MC campaign expectation and appropriately adjusting for the 110.8 day runtime after cuts presented in Section 6.5, the expected rate before applying the IBD event cut efficiency is ~ 29.8 events. The IBD cut efficiency is $80.9 \pm 1.1\%$, which results in a final expectation of around ~ 24.1 reactor antineutrino events for the IBD geoneutrino analysis of this thesis.

6.2.4 Muon/High-NHit Veto and Multiplicity Cut

The interactions between cosmic ray muons and nuclei in the scintillator can produce neutrons and unstable isotopes [101], which could contribute IBD-like events in the SNO+ detector.

- ${}^9\text{Li}$ and ${}^8\text{He}$: These are a few of the nuclei produced by passing muons that emit neutrons after β decay. The emitted neutron has the possibility of creating a signal mimicking the IBD coincidence signal, where for example the β can be tagged as prompt and the neutron could be tagged as a delayed event.



The half-life for ${}^9\text{Li}$ is about 0.18 s, with a $\beta + n$ branching fraction of 51%. The half-life for ${}^8\text{He}$ is about 0.12 s, with $\beta + n$ branching fraction of 15% [101].

- ${}^{18}\text{O}(n,n+p){}^{17}\text{N}$: Muons can induce this interaction while traveling through the external water volume. The produced ${}^{17}\text{N}$ can also undergo $\beta + n$ decay. The lifetime for this interaction is 4.17 s [102]. The produced neutron can make its way into the main acrylic vessel volume and become captured, mimicking an IBD event. These events were studied during the water phase of the experiment. Most if not all of these events are taken care of by applying a fiducial volume cut.
- Neutrons: Muons traveling through scintillator volume can produce bursts of neutrons. These neutrons occur in rapid succession and can be mistaken as IBD

coincidence events. During the analysis, after cutting the IBD candidates that followed a tagged muon event the author identified pairs of events that have prompt and delayed energies around 2.2 MeV and were close in time $\Delta T < 10$ microseconds.

To avoid these types of backgrounds a “High NHit” veto was developed. A candidate pair of prompt and delayed events were rejected if they occurred within 20 seconds of an event that exceeded 2500 NHits. There were 55492 events above 2500 NHit within the data set used for analysis in this thesis, specified in Section 6.1. This High NHit veto resulted in 12 days and 20 hours being cut, leaving the runtime for the final dataset to be 110 days and 19 hours. After this cut was applied, it was verified that the neutron follower background identified previously was removed.

Another cut used to remove cosmic ray muon backgrounds is the multiplicity cut. This cut attempts to flag coincidence pairs due to multiple neutrons. The cut flags the candidate pair if there is any other energetic event with $E > 0.4$ MeV that occurred within 2 meters of the detected coincidence pair and 2 ms before and after the delayed event. The $E > 0.4$ MeV energy was chosen in order to incorporate backgrounds from fast neutron scattered protons, discussed in Section 5.1. As detailed in the next section, this multiplicity cut was applied at the very end, after all, other cuts were applied and did not flag any tagged candidate event pairs as occurring too near a third candidate event. While this cut was not responsible for removing any background processes so far, it provided a nice check in the effectiveness of the other cuts applied to remove backgrounds with multiple neutrons.

6.2.5 Accidental Events

When tagging IBD coincidence events, there is a possibility that two physically uncorrelated events from non-antineutrino processes will occur within the chosen coincidence cuts on energy, time, and space. Such event pairs could look accidentally like an IBD coincidence event. One way to estimate the rate of these accidental events is to use the same selection cuts as are used for the candidate events but with an extended ΔT time window. This allows us to estimate how often events would occur close enough to one another in space, and with the correct energies, to mimic the IBD signature through pure accident. To determine the accidental rate, the same cuts as detailed in the next Section in Table 6.3 were used, but the ΔT was extended to $1.2 - 12$ ms, a time which is 13.5 times longer than the original time cut. In this time window, 2 coincidence pairs were found across the entire dataset, implying a predicted accidental rate of 0.15 ± 0.20 events within the IBD antineutrino dataset. This rate is negligible compared to previously discussed backgrounds.

6.3 Event Selection

This section details the process of event selection for the geoneutrino analysis at SNO+, as calibrated using AmBe data and Monte Carlo simulations.

6.3.1 Prompt and Delayed Event Distance Correlation

For signal IBD coincidence events produced through an antineutrino interaction, the distance between the prompt positron annihilation event and the delayed neutron absorption event can be assumed to be given by the neutron thermal diffusion length and the 2.2 MeV γ travel distance in the SNO+ detector. As already discussed in

Section 3.3, at the site of the antineutrino interaction with a proton, the positron and neutron get created at the same location, and the positron travels a minimal distance before annihilating. Therefore, the reconstructed position of the prompt event should be very close to the starting position of the neutron. The position correlation cut was determined using MC simulation of the geoneutrinos (see Figure 6.7). Neutron delta R distributions from AmBe events, discussed in section 5.3 seem to support this. A cut of $\Delta R < 1.5$ m was made, which effectively selects all simulated geoneutrino MC events shown in Figure 6.7. The efficiency of the cut applied to U and Th geoneutrino data was calculated to be $99.33(\pm 0.28)\%$.

6.3.2 Prompt and Delayed event Time Correlation

The time between the prompt and delayed events in the IBD reaction can be described as a mean neutron lifetime in the scintillator. From the creation of positron and neutron, the prompt event sets time $t = 0$. The time difference is expected to follow an exponential distribution as in equation 6.11, where τ is neutron mean capture time.

$$N(\Delta T) \propto e^{-\frac{\Delta T}{\tau}} \quad (6.11)$$

The Monte Carlo neutron mean capture time was fitted to $\tau \sim 204\mu\text{s}$, which is consistent with expectation compared to KamLAND [103], another experiment that searched for geoneutrinos in the scintillator. Figure 6.8 shows the time difference between prompt and delayed events from thorium and uranium geoneutrino Monte Carlo simulation. The coincidence cut for ΔT was chosen as $400 < \Delta T < 800000$ ns, where the lower cut on time is in part motivated by the timescale set by the SNO+ trigger gate event width. Following a SNO+ triggered event, there is a subsequent 420

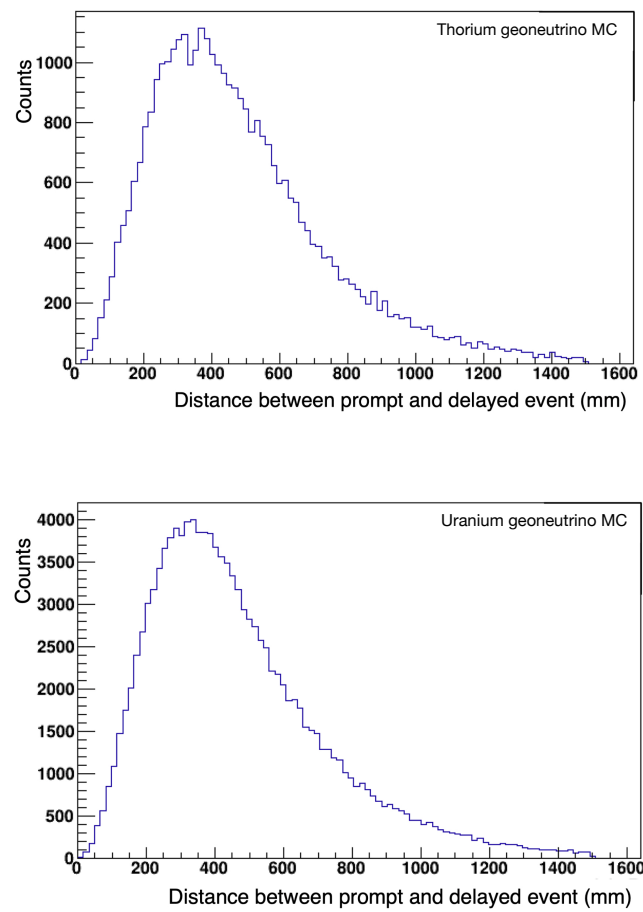


Figure 6.7: Distance between the prompt and delayed event (ΔR) distributions from thorium (top) and uranium (bottom). Data is obtained from the official Monte Carlo production simulations of geoneutrino IBD events in the SNO+ detector. Simulated events get uniformly distributed in the AV volume.

ns dead time during which the global trigger cannot fire. Cutting out this timeframe assures that no fake electronic noise and other DAQ-associated effects would be tagged as delayed event following the prompt event. The upper cut on the ΔT comes from a Monte Carlo determination of a reasonable timeframe within which a neutron in an IBD event would diffuse and be captured (as seen in Figure 6.8. The efficiency of the ΔT cut was calculated for IBD Monte Carlo to be $97.58(\pm 0.28)\%$.

6.3.3 Analysis cuts for IBD selection

With preliminary analysis of all backgrounds and signal Monte Carlo event characteristics concluded, we are ready to present the cuts used for IBD coincidence event selection in the geoneutrino search at SNO+. The cuts are listed in Table 6.3. These cuts were tested using Partial fill phase data and also on MC-generated events. The combined efficiency of the cuts for IBD antineutrino detection from MC simulation was determined to be $80.87(\pm 0.23)\%$ and for $^{13}\text{C}(\alpha, \text{n})^{16}\text{O}$ background events, $71.203 \pm 0.075\%$.

For both IBD antineutrino detection and the $^{13}\text{C}(\alpha, \text{n})^{16}\text{N}$ background, the fiducial volume cut was the predominant factor driving the event selection efficiency. In both cases, the volume cut removed a bit over 10% of events. Integrating over a larger volume was found to be less statistically advantageous, as the $^{13}\text{C}(\alpha, \text{n})^{16}\text{O}$ background increased substantially very near the acrylic vessel surface. In the end, an $R_{FV} = 5.7$ m fiducial volume was used in this analysis. To check whether this 5.7 m radius fiducial volume was being overcrowded by alpha-n events coming in from the acrylic vessel surface, we tested the effect of implementing an $R_{FV} = 5.5$ m radius fiducial volume and determined whether making this cut reduced alpha-n

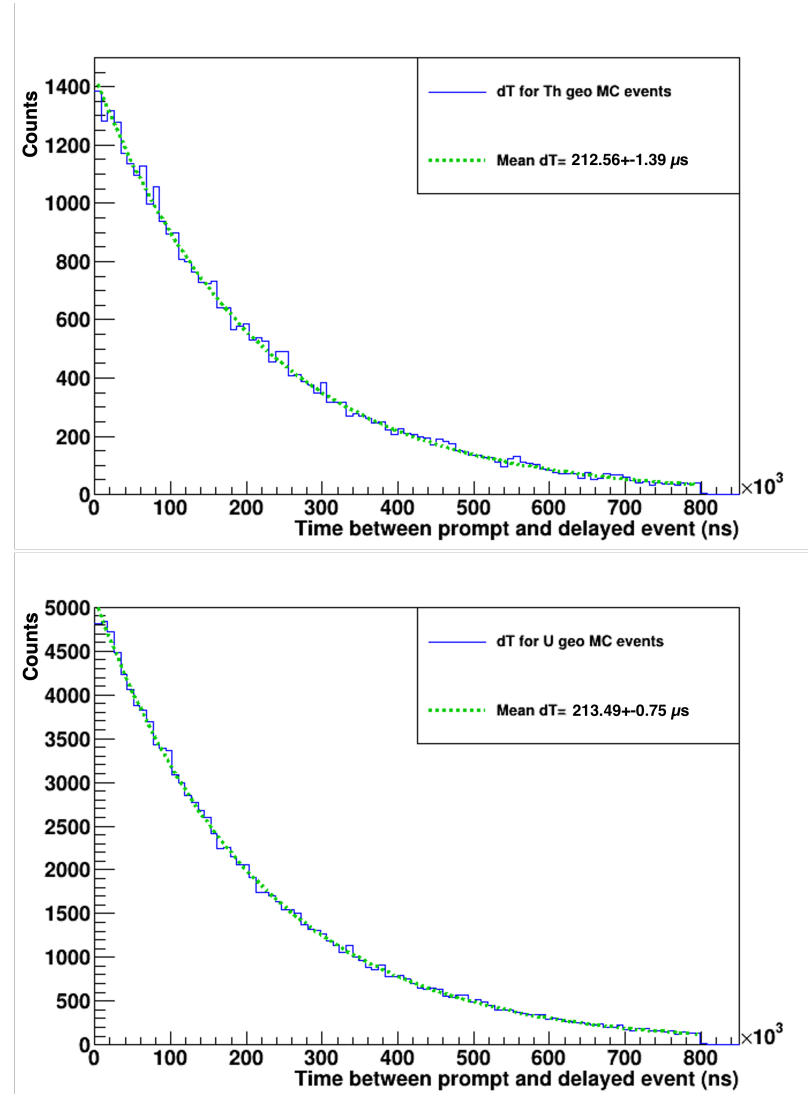


Figure 6.8: Time between the prompt and delayed event (ΔT) distributions from thorium (top) and uranium (bottom). Data is obtained from Monte Carlo simulations of geoneutrino IBD events in the SNO+ detector.

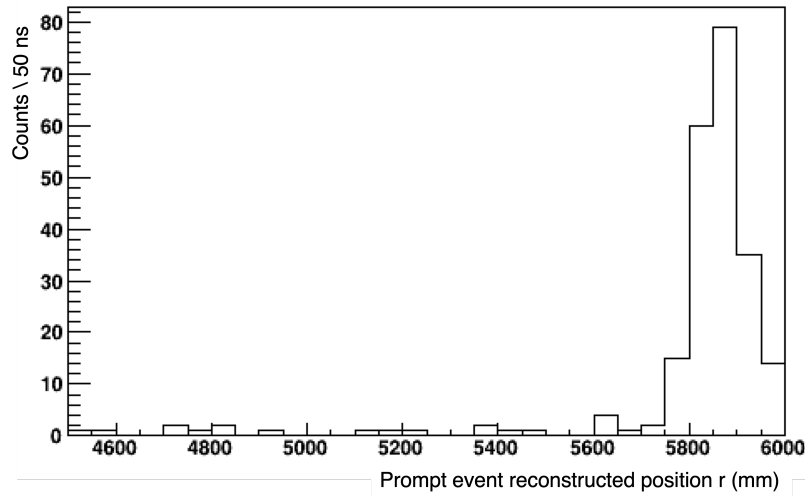


Figure 6.9: Tagged coincidence counts versus the prompt event reconstructed radial position from the AV center. Here we see positions ranging from 4.5 m to 6 m, to illustrate the choice of 5.7 m FV volume cut.

events. Comparing the rate of alpha-n events in these two fiducial volumes, we found no significant AV surface $^{13}\text{C}(\alpha, n)^{16}\text{O}$ contamination compared to the expected bulk scintillator contamination levels. Figure 6.9 shows the tagged coincidence event rate versus the prompt event radial position from the AV centre. We investigate the 4.5 m to 6 m range to validate the choice of 5.7 m FV cut. We can clearly see the spike in event rate beyond 5.7 m, which can be attributed to the AV surface $^{13}\text{C}(\alpha, n)^{16}\text{O}$ contamination.

6.4 Coincidence Tagging Algorithm

A custom code was developed to find pairs of coincident events in the IBD dataset, while also correctly implementing the cuts listed in the prior section. In this section, a simplified version of this code is presented, to explain the logic of the coincidence selection algorithm.

Parameter Cuts	Cut Applied	IBD Cumul. Effic.	α -n Cumul. Effic.
Nhits (#/event)	Nhit > 60	99.11 (± 0.27)%	95.91 (± 0.09)%
Prompt Energy (MeV)	0.9 < E < 8	98.35 (± 0.27)%	87.78 (± 0.09)%
Delayed Energy (MeV)	1.8 < E < 2.4	94.62 (± 0.26)%	84.06 (± 0.09)%
ΔR (m)	$\Delta R < 1.5$	94.00 (± 0.26)%	83.17 (± 0.08)%
ΔT (μ s)	0.4 < ΔT < 800	91.71 (± 0.26)%	81.19 (± 0.08)%
Fiducial volume (m)	R < 5.7	80.87 (± 0.23)%	71.20 (± 0.08)%
Additional Cuts		Cut Applied	–
FitValid	True	–	–
Data Cleaning mask	applied	–	–
Muon High Nhit > 2500	cut 20 s after	–	–

Table 6.3: Summary of the antineutrino candidate coincidence selection cuts applied to data ntuples for the geoneutrino IBD antineutrino analysis of this thesis. The cumulative efficiency for parameter cuts applied to official production MC geoneutrino IBD and alpha-n events is shown. Cuts shown at the bottom are the data cleaning mask, the Muon High Nhit cut which was applied to data, and the FitValid precut discussed in the text. The total parameter cut efficiency for the alpha-n MC event sample was $71.203(\pm 0.075)\%$ and for the IBD events was $80.87(\pm 0.23)\%$.

All triggered events are written out sequentially in time and have an associated time signature assigned to them, as well as a Global Trigger ID (GTID). The GTID makes it easy to identify a specific event and access all the other stored information, including reconstructed values, such as energy deposit and vertex location. The collected data sets are extremely large and the RAT ROOT files are first processed into ROOT ntuple files. The raw root files have much more information than is used. This information is retained to aid calibration work and verbose tracking reconstruction. For example, in the case of timing residual plots discussed in section 5.6, the raw root files were used. Ntuples store only vital information needed for a specific analysis, and such files are easier to access and take up less space in the local computing clusters.

The ROOT code developed for the geoneutrino search for this thesis is designed to work on SNO+ data ntuples.

6.4.1 Coincidence Algorithm Classes

The code contains two custom classes

1. Prompt Candidate: If the detected event matches prompt event criteria, detailed information about the event is stored in vector format using a function to store the candidate information. The code then iterates forward in time looking for a delayed event candidate, If no delayed event candidate is found it calls a function to erase the information stored in the vector and begins looking for another prompt candidate.
2. Coincidence: If a prompt candidate is stored by the candidate class and a delayed candidate is found to match all the coincidence criteria, the information for prompt and delayed candidates is written out into one larger vector and stored as a pair.

6.4.2 Coincidence Algorithm Functions

The main functions employed in the coincidence event algorithm are:

1. FindCandidate: As the main code iterates over detected events, this function collects time and position information to be stored alongside the already stored prompt candidate information vector. The spatial correlation between any two candidate prompt and delayed events is calculated using the reconstructed event

position:

$$\Delta x = x - x_{\text{prompt}} \quad (6.12)$$

$$\Delta y = y - y_{\text{prompt}} \quad (6.13)$$

$$\Delta z = z - z_{\text{prompt}} \quad (6.14)$$

$$\Delta R = \sqrt{\Delta x^2 + \Delta y^2 + \Delta z^2} \quad (6.15)$$

The ΔR and ΔT cuts are then checked against the coincidence criteria and if they are met it returns the index to the vector of the prompt event to indicate that information has to be saved. If the candidate is not found then the function returns as invalid, which starts a new search.

2. PerformCuts: The main function that loops over all events and calls classes and functions for the coincidence search. First, it sets the required branch addresses for the variables needed to be called from the ntuple and creates new custom branches for the coincidence information to be stored, which can be written out later. Then the main set of nested loops and conditional statements begin. Pseudocode that follows the basic structure of our PerformCuts function is given below:

```

for each indexed entry Event(i) do
    if Event(i) has a valid fit then
        if Event(i) passes data cleaning flag then
            if Event(i) has  $n_{\text{hit}} > 60$  then
                -Reset z-position variable to Event(i) location
                -Calculate radial position using Event(i) coords

```

-Calculate Event(i) time, converting 50Mhz clock counts to ns

for Each saved positron Candidate(i), remove Candidates with times outside allowed ΔT **do** \triangleright *This is skipped if there are no positron event candidates.*

-Rescale the Event(i) energy using the run calibration histogram

-Check for a delayed event candidate among Events beyond entry Event(i) \triangleright *This initiates an Event search with checks similar to all preceding steps.*

if A candidate delayed DEvent(i) is found **then**

- Store the Event(i) and DEvent(i) as IBD prompt and delayed information
- Call EraseCandidate Event(i) to remove the prompt candidate \triangleright *This avoids double counting prompt candidates as the code runs through events.*

else

if No prompt candidate was found beyond Event(i) **then**

- Check among events entries *before* Event(i) and determine if Event(i) is a delayed event with a valid preceding prompt event

If a prompt and delayed event pair meet all selection criteria, the above algorithm will save this as a new ntuple, within which each entry is a coincidence event pair, with both the prompt and delayed event information saved for each coincidence event pair. We now briefly detail a few more algorithms responsible for the final processing

of the stored coincidence event pairs.

Muon Veto Processing. After the PerformCuts procedure is finished, another algorithm is applied to the set of saved coincidence pairs. This second pass takes in a file of all the tagged muon (high Nhit) events, extracts all the muon veto times, and stores it in a vector. Then it reads in the coincidence pair time information and detects if any of the IBD candidates occurred within the 20 seconds following the tagged muon veto time. If the event is within that time it is discarded. For all other coincidence events, this algorithm calculates the time difference to the nearest prior muon veto occurrence and saves that for later review and reference. This part of the code also adds a fiducial volume cut and can implement stricter cuts than those applied in the PerformCuts phase, if stricter cuts are needed.

Multiplicity Cuts. There is a final script that applies a multiplicity cut. This script is run on the initial data files and detects if there was any event with an energy $E > 0.4$ MeV that occurred within 2 meters and 2ms of the detected coincidence pair. If any such event is found, that coincidence pair is flagged as a possible background event, since this means it could be an event produced by a shower of muons, resulting from an atmospheric neutrino or a cosmic ray muon, which might have been missed by the muon veto cut.

6.5 Geoneutrino Flux Result

Having completed all the preliminary explanations of data cleaning, backgrounds, and analysis methods, we are ready to present the IBD coincidence search for geoneutrinos at SNO+. The coincidence analysis was performed for the 110.8 days worth of “gold” quality data as discussed in Section 6.1. After all cuts were applied, there were

55 candidate events in the final tally. These events then were fitted using RooFit toolkit [104]. Four probability density functions of prompt event energy distributions were created using MC production, which used the input for the detector state for each run in the dataset. Using these PDFs, an extended maximum likelihood fit was implemented with two constraints.

The first external constraint applied to the fit was on the expected alpha-n rate. The author found that varying the alpha-n rate changed the fit for geoneutrinos substantially, as the main contribution to the geoneutrino IBD signal lies in a similar energy range as the alpha-n background, as discussed at great length in Chapter 5. Hence, an expected rate of $N(\alpha, n) = 17.4 \pm 5.2$ was used as a constraint in the fit, as obtained in Section 6.2.1. In the context of the likelihood fit used in this analysis, an “external constraint” means that the fit was allowed to float the parameter beyond the uncertainty of the expected value provided, but with a statistical penalty weighted by the uncertainty.

The second external constraint was the U/Th geoneutrino ratio. This value comes from the geological refractory element ratio measurement, as appropriately adapted to match the ratio at which the uranium and thorium geoneutrino spectra would be detected at SNO+, as discussed in Chapter 4. This ratio was computed to be $U_{geonu}/Th_{geonu} = 3.7 \pm 1.3$ for the SNO+ detector. The values for calculation were taken from signal expectation values in Table 4.5, and uncertainty was propagated using the larger error values for U and Th total TNU at the last row of the table.

Only the above two values were constrained as these are the only two values that have been determined externally. However, the U/Th ratio is an expectation from BSE models and not a hard constraint. With more statistics, we would hope to float

the ratio value and measure the fluxes of U and Th geoneutrinos separately. The geoneutrino and reactor neutrino rates were left to float entirely.

The script to fit the data was tested using the ensemble method. A thousand pseudo-experiments were generated by random Gaussian sampling around the mean expected values of the rates of signals and backgrounds and by constructing fake data histograms. The input mean values for the Gaussian distributions for geoneutrinos were taken from MidQ model expected rate, 11.0 ± 3.3 for uranium and 3.0 ± 1.7 for thorium. The mean value used for reactors was 25 ± 5 , and for alphaN 17.0 ± 4.2 . Then all the pseudo-experiment data was fitted and the generated input parameter yield, fitted yield, and the fitted error were saved to compute the pull. We define pull as the fitted yield minus the input yield all divided by the error in the fitted yield. Then the pull distributions were plotted for each fit parameter and can be seen in Figures 6.10. From the pull distributions, we can see that the means of each distribution are generally close to zero, as well as the root mean square (RMS) values are close to 1, which demonstrates that the fit is well-behaved. Another notable thing is that in the alphaN distribution, we do see a slight skew to the negative, which informs us that the fit tends to underestimate this background. While the uranium and reactor pull distributions are slightly skewed to the positive, which implies that while the alphaN rate tends to fit lower it provides us with larger values for uranium and reactor antineutrinos. This means that having a strong external constraint on alphaN background is extremely important to the fit.

For the reactor mass splitting parameter Δm_{21}^2 there were two separate PDFs made to accommodate different choices for the mass splitting parameter, see Section 6.2.3. These separate fits were performed to see how changing this parameter would

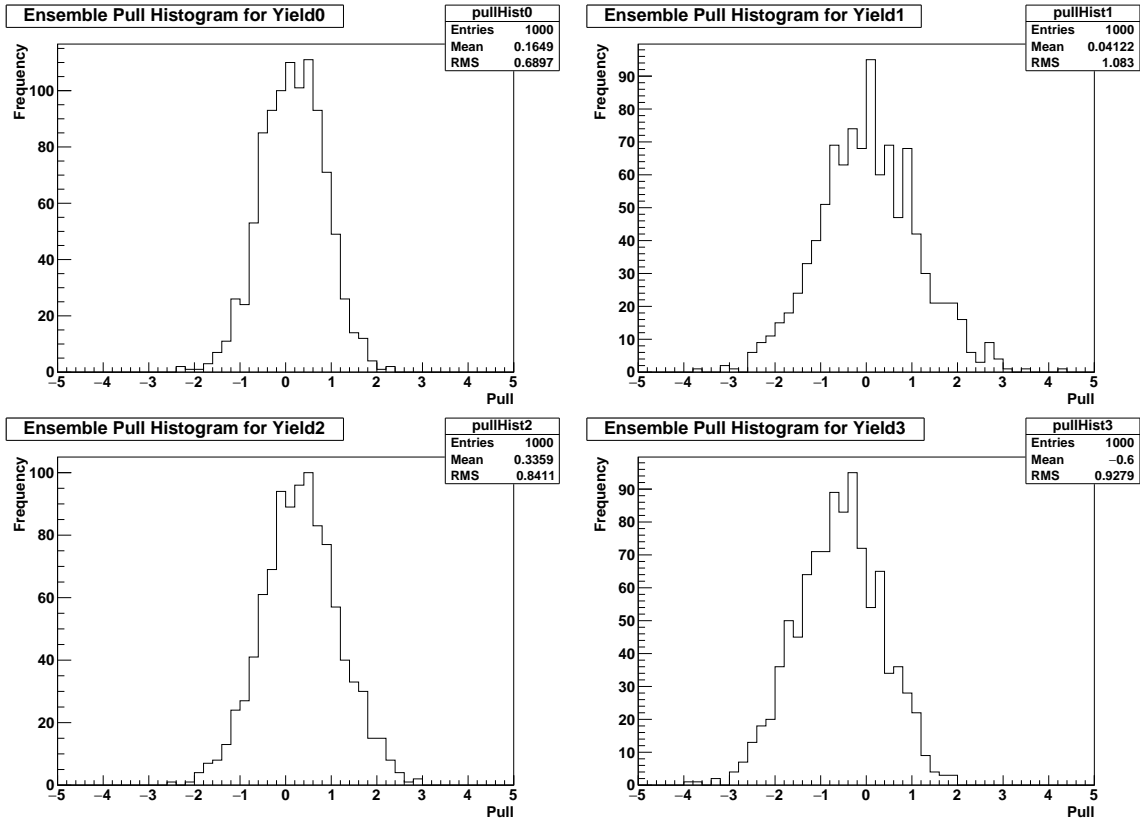


Figure 6.10: The pull distributions for each parameter from the ensemble test with 1000 pseudo-experiments. Here yield0, yield1, yield2, and yield3 correspond to uranium and thorium geoneutrinos, reactor antineutrinos, and alphaN background respectively.

impact the geoneutrino signal result.

- The first fit was performed with $\Delta m_{21}^2 = 7.53 \times 10^{-5} \text{ eV}^2$ and $\sin^2 2\Theta_{12} = 0.861$, which is the global fit measured value for this neutrino mass splitting squared parameter, dominated by the KamLAND reactor oscillation measurement [98]. Table 6.4 and Figure 6.11 show the results of this fit. This is the main result of this thesis that we will discuss shortly. The fit parameter correlation matrix is shown in Table 6.5 and Figure 6.13. We can see that uranium and thorium geoneutrinos are positively correlated and there is a negative correlation between

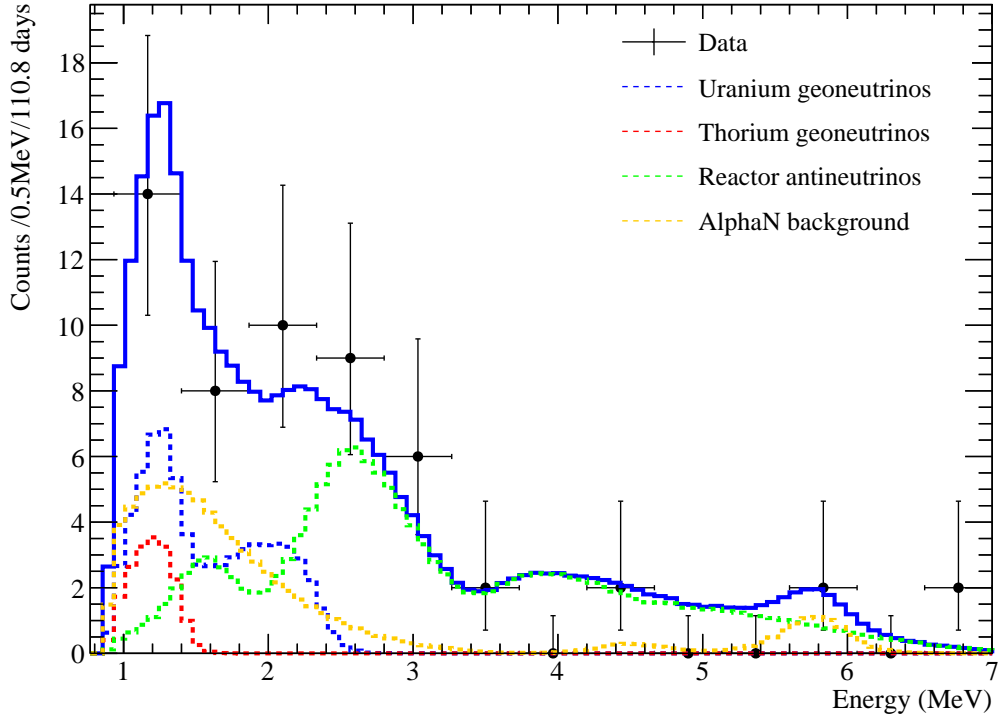


Figure 6.11: The prompt energy (MeV) of 55 IBD coincidence candidate events selected from 110.8 days of SNO+ “gold” run full scintillator fill data. An extended maximum likelihood fit was performed using four probability density functions generated using run-specific MC production. The thorium produced geoneutrino PDF can be seen in red and uranium geoneutrinos are shown in blue. The reactor PDF (green) was generated using $\Delta m_{21}^2 = 7.53 \times 10^{-5} \text{ eV}^2$. The alpha-n PDF (yellow) measured rate of $N(\alpha, n) = 17.4 \pm 5.2$ was used as an external constraint, along with the second external constraint on the uranium to thorium ratio, $U_{\text{geonu}}/\text{Th}_{\text{geonu}} = 3.7 \pm 1.3$. Fit result values can be seen in Table 6.4.

alphaN and uranium geoneutrino signals.

- The second fit was performed using a neutrino mass splitting parameter $\Delta m_{21}^2 = 5.00 \times 10^{-5} \text{ eV}^2$. This value is the value preferred by solar neutrino data [99] [105]. We have purposefully picked this low value to study how the fit is affected if neutrino oscillation parameters are varied. We find that our fit changes only

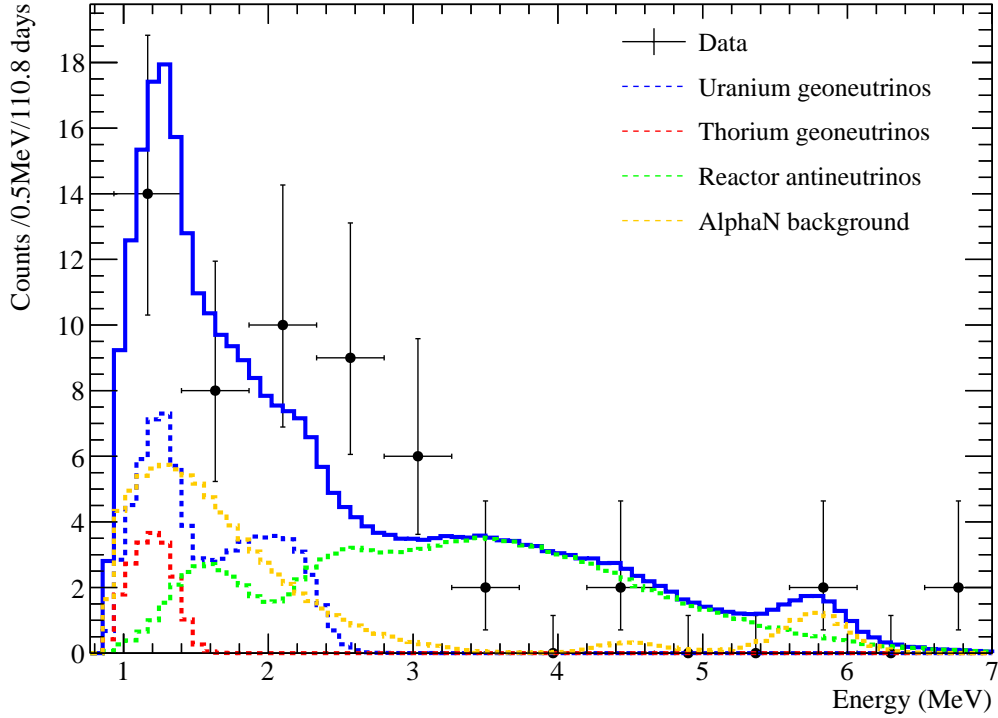


Figure 6.12: Same as Figure 6.11, which is the main result of this analysis, but in this fit we have tested the effect of setting $\Delta m_{21}^2 = 5.00 \times 10^{-5} \text{ eV}^2$. Fit result values can be seen in Table 6.6.

component	best fit
uranium geoneutrino	12.1 ± 4.7
thorium geoneutrino	3.1 ± 1.5
Reactor antineutrino	26.8 ± 6.1
Alpha-N	14.5 ± 4.5
$U_{\text{geonu}}/Th_{\text{geonu}}$	3.8 ± 2.4
χ^2/ndof	0.429

Table 6.4: Fit values for the 55 IBD coincidence candidate events selected from 110.8 days of SNO+ “gold” run full scintillator fill data. An extended maximum likelihood fit was performed using four probability density functions generated using run-specific MC production. The reactor PDF for this fit was generated using $\Delta m_{21}^2 = 7.53 \times 10^{-5} \text{ eV}^2$ [98]. The fit had two external constraints discussed in the text: $N(\alpha, n) = 17.4 \pm 5.2$, $U_{\text{geonu}}/Th_{\text{geonu}} = 3.74 \pm 1.3$.

Parameter	yieldA	yieldR	yieldTh	yieldU
yieldA	1.000	-0.178	-0.284	-0.390
yieldR	-0.178	1.000	-0.052	-0.118
yieldTh	-0.284	-0.052	1.000	0.506
yieldU	-0.390	-0.118	0.506	1.000

Table 6.5: Fit parameter correlation matrix corresponding to the fit result described in Table 6.4. YieldA, yieldR, yieldTh, and yieldU correspond to alphaN, reactor antineutrinos, thorium, and uranium geoneutrinos respectively.

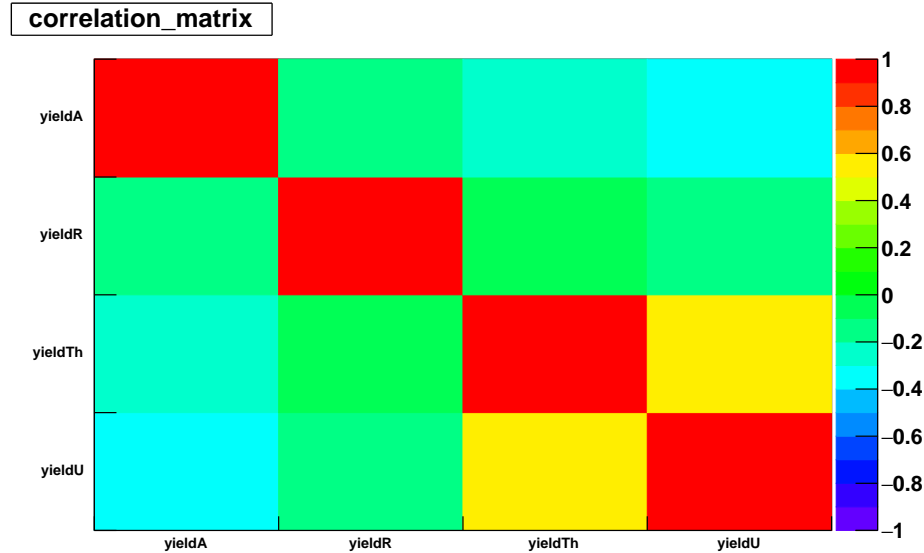


Figure 6.13: 2D histogram of fit parameter correlation matrix corresponding to the Table 6.5. YieldA, yieldR, yieldTh, and yieldU correspond to alphaN, reactor antineutrinos, thorium, and uranium geoneutrinos respectively.

component	best fit
uranium geoneutrino	12.7 ± 4.7
thorium geoneutrino	3.2 ± 1.5
reactor antineutrino	24.0 ± 5.9
Alpha-N	15.9 ± 4.4
U_{geonu}/Th_{geonu}	4.0 ± 2.4
$\chi^2/ndof$	0.803

Table 6.6: Same as Table 6.4, but the reactor PDF was generated using $\Delta m_{21}^2 = 5.00 \times 10^{-5} \text{ eV}^2$.

a small amount, by +4.6% with this change in Δm_{21}^2 (the χ^2 value is also a bit worse). Table 6.6 and Figure 6.12 show the results of this fit.

From the fit result shown in Table 6.4 we see that the total number of geoneutrinos measured is 15.2 ± 4.9 . We will want to convert this to units of Terrestrial Neutrino Units (TNU) defined in Chapter 4, which for convenience we restate here: 1 TNU = 1 event per year per 10^{32} protons with 100% acceptance efficiency. The dataset and cuts we have applied include 110.8 days of exposure, an $80.87 \pm 0.23\%$ efficiency factor, and a total number of protons $N_{\text{protons}} = 5.700(\pm 0.014) \times 10^{31}$. Converting our number of measured geoneutrinos to TNU results in the following value for 110.8 days of full scintillator fill at the SNO+ experiment,

$$109 \pm 35 \text{ TNU}. \quad (6.16)$$

The central value of this result is higher than our model expectations presented in Table 4.5, but accounting for the uncertainty, is well within 2σ expectations of the local geological model constructed in this thesis. In the concluding Chapter 7, there is an extended discussion of the implications of this geoneutrino measurement, and a comparison to past geoneutrino measurements at Kamland and Borexino.

Before concluding this Chapter, now that we have completed the first geoneutrino analysis at SNO+, it will be useful to examine the measured distributions of our 55 IBD coincidence events and compare these to Monte Carlo expectations, to see if our MC analysis matches IBD coincidence data.

In Figure 6.14, we plot the distribution of ΔT against the number IBD coincidence events. Our fit to data suggests a mean neutron diffusion time of $\Delta T = 179 \pm 63 \mu\text{s}$, which is within the expectation of around $200 \mu\text{s}$.

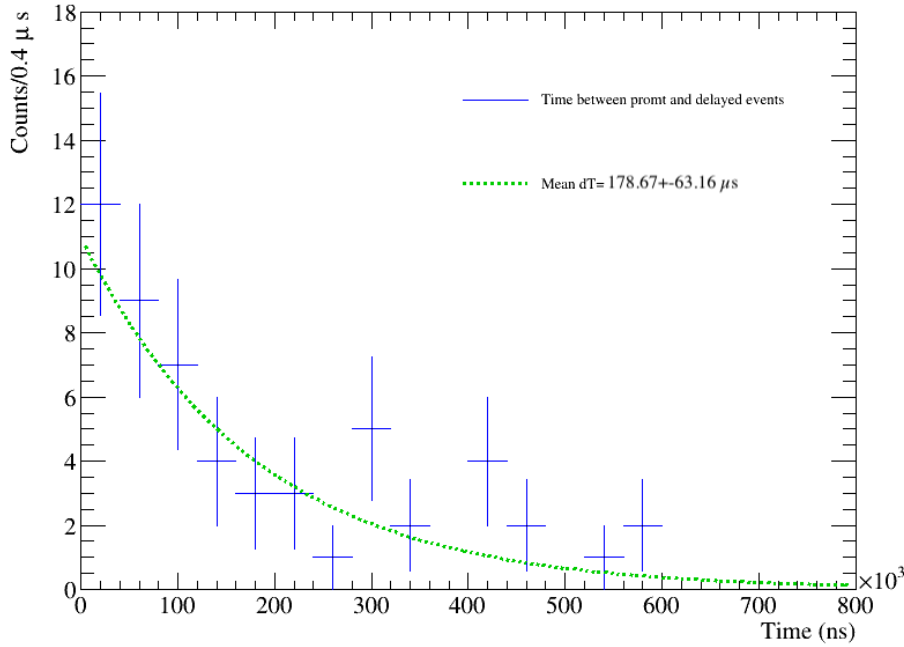


Figure 6.14: Time between prompt and delayed events of the observed coincidence pairs fitted to an exponential. The mean time for neutron capture in SNO+ scintillator is expected to be around $200 \mu s$ and the fit here gives a mean $\Delta T = 179 \pm 63 \mu s$, which is within the expectation.

Next, we examine the delayed energy distribution of our 55 IBD coincidence events and compare these to the Monte Carlo expectation for the energy measured in the SNO+ detector when a neutron is captured on a proton. In Figure 6.15, the energy of our 55 IBD coincidence events is plotted alongside a uranium geoneutrino Monte Carlo delayed event energy histogram, that has been normalized to have 55 events for ease of comparison. We see that the MC spectrum matches the data.

Finally, we examine the distance measured between the delayed and prompt events in the SNO+ detector for our 55 IBD coincidence events, and compare these to the Monte Carlo expectation for the distance between delayed and prompt events in Monte Carlo simulations. Figure 6.16 shows the comparison between MC IBD

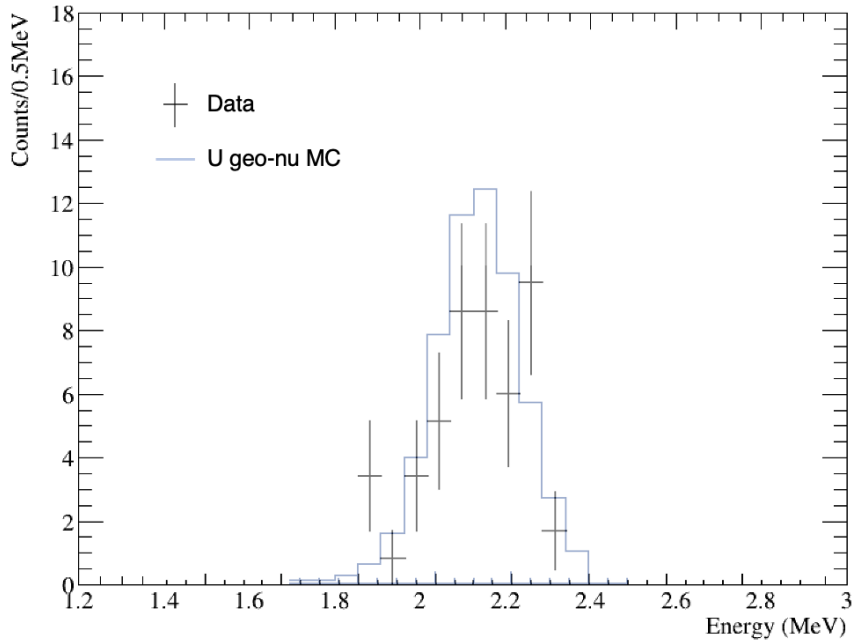


Figure 6.15: Delayed event reconstructed energy for the 55 IBD coincidence events in our full fit analysis presented in Table 6.4. Uranium geoneutrino Monte Carlo simulation data, normalized to 55 events, is overlaid for comparison.

and measured prompt-delay distances. For genuine antineutrino signal events, this distance will be determined by the distance between the site where the positron deposited energy and annihilated with an electron, and the reconstructed site and time at which the 2.2 MeV gamma produced by the captured neutron is detected. Again we find the 55 IBD coincidence event measurements match a Monte Carlo uranium IBD simulation of the prompt-delay separation.

In the next and final Chapter of this thesis, we present a summary and discussion of the SNO+ 110.8 day exposure geoneutrino measurement.

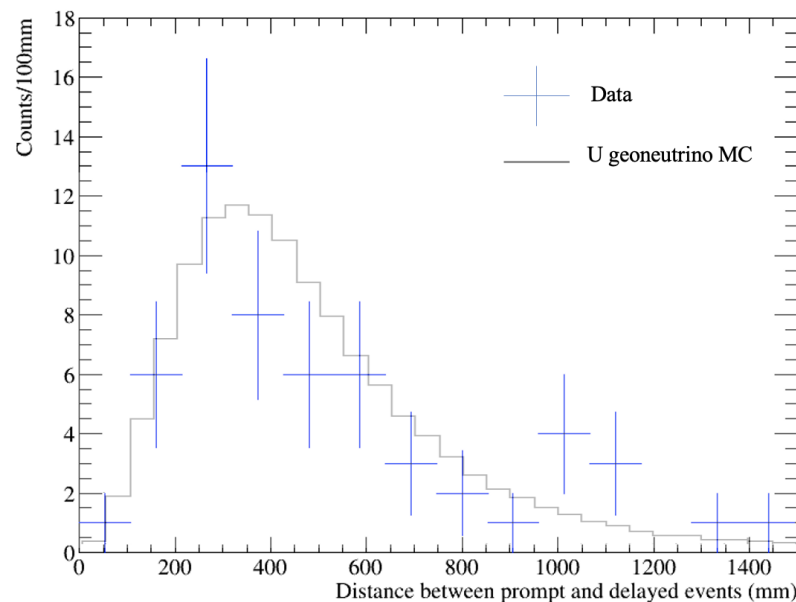


Figure 6.16: Distance between the prompt and delayed events for the 55 IBD coincidence events in our full fit analysis presented in Table 6.4. Uranium geoneutrino Monte Carlo simulation data, normalized to 55 events, is overlaid for comparison.

Chapter 7

Summary and Discussion

7.1 Summary

This thesis has developed and presented the first measurement of geoneutrinos at the SNO+ experiment. Chapter 1 introduced the basic principles of neutrino oscillation, and inverse beta decay events from antineutrinos in detectors, and discussed the expected spectra for uranium and thorium geoneutrinos at a liquid scintillator experiment. The geological principles underlying primordial and radiogenic heat flow from the Earth and the Bulk Silicate Earth Model were reviewed in Chapter 2, with emphasis on the implications of geoneutrino measurements for distinguishing between LowQ, MidQ, and HighQ Bulk Silicate Earth models. Chapter 3 provided details about the SNO+ experiment and SNO+ detector, including the phases of the experiment, detector characteristics, data handling, and analysis software. The detection of antineutrinos using IBD events at SNO+ and the IBD cross section were laid out in this Chapter. In Chapter 4, the modeling of the expected geoneutrino signal at the SNO+ was described using three increasingly sophisticated methods. In particular,

the “refined regional model” for the geoneutrino flux at SNO+ was finalized and compared to prior models. Chapter 5 provided an account of alpha-n backgrounds, which are the dominant background at SNO+ for IBD antineutrino detection. The use of a log-likelihood classifier for IBD coincidence events was tested on the geoneutrino dataset and certain interesting features of the AmBe calibration data were pointed out for future exploration. Finally, Chapter 6 presented the first search for geoneutrinos at the SNO+ experiment. A total of 110.8 days of run data were fit using log-likelihood PDFs, including a fit to backgrounds from reactor antineutrinos and alpha-n events, and 15.2 ± 4.9 geoneutrino events were measured, corresponding to 109 ± 35 Terrestrial Neutrino Units (TNU).

7.2 Overview of Previous Geoneutrino Measurements and Discussion

In order to put the geoneutrino measurement above into proper context, we turn to past geoneutrino measurements at other experiments. Prior to SNO+, geoneutrinos have been measured the KamLAND [17] and Borexino [106] experiments.

- KamLAND is a 1 ktonne liquid scintillator detector located in the Kamioka Underground Laboratory in Japan. Figure 7.1 shows a schematic drawing of the detector. Within the detector is a 13 meter diameter transparent nylon balloon filled with liquid scintillator, seated inside the buffer oil to hold the weight of liquid scintillator, as well as to shield the fiducial volume from γ rays. Surrounding that there is an 18 meter diameter stainless steel tank that houses around 1300 PMTs to detect the scintillation light. Another layer of the outer detector is filled with around 3 tonnes of pure water acting as additional shielding and muon veto volume.

- Borexino is a 0.3 ktonne liquid scintillator detector located in the Gran Sasso laboratory in Italy. The detector has around 2000 PMTs, and the liquid scintillator is contained in a large nylon balloon around 8.5 meters in diameter. Surrounding that there is a buffer region inside the stainless steel tank of 13.7 meter diameter, which houses the PMTs. All of that is surrounded by a layer of water which acts as a shield from backgrounds, as well as a volume for muon veto.

These detectors are similar in many ways. However, in terms of geoneutrino detection, their geological setting is rather different. Borexino's global position results in a large geological contribution from the continental crust. KamLAND is set in Japan, where there is a larger portion of oceanic crust surrounding the detector. Having geoneutrino measurements from these different geological settings provides for nicely complementary datasets. Another difference is each detector's ability to remove nuclear reactor neutrino backgrounds. KamLAND was primarily built for the purpose of detecting reactor neutrinos, whereas Borexino was built with a focus on scattering events from solar neutrinos. KamLAND had quite a large reactor neutrino signal compared to Borexino¹, which has its nearest reactor located 400km away in Slovenia.

In 2005 the first experimental observation of geoneutrinos was obtained by KamLAND [108]. At that time, KamLAND measured the low energy antineutrino spectrum shown in Figure 7.3, finding a total number of 25^{+19}_{-18} candidate geoneutrino events.

In 2011 Borexino presented their first observation of the geoneutrino flux [109];

¹However, after the Sendai Earthquake and in 2011, many nuclear power plants near KamLAND were taken offline, and the reactor background at KamLAND is much lower now [107].

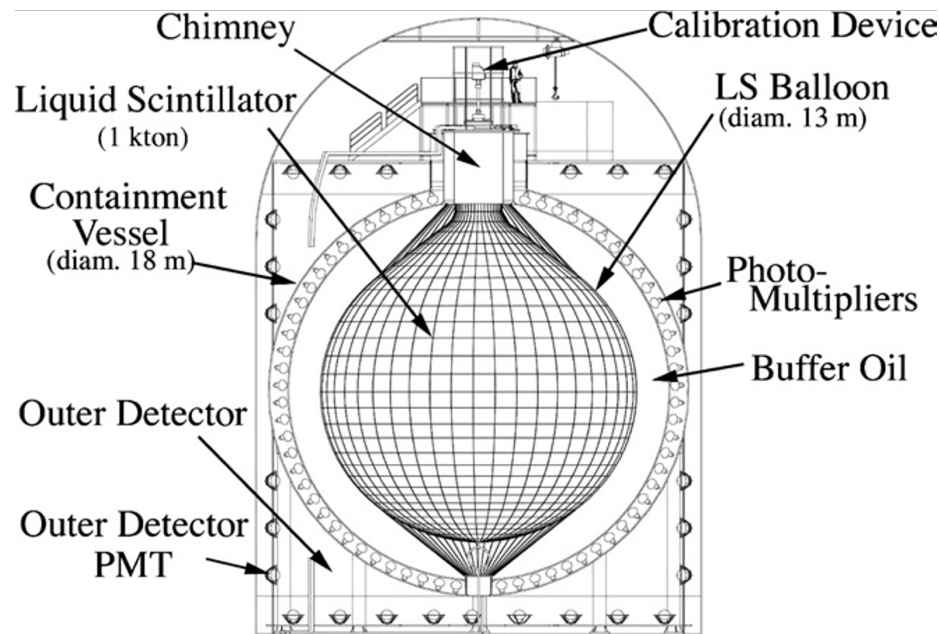


Figure 7.1: Schematic drawing of the KamLAND detector[17].

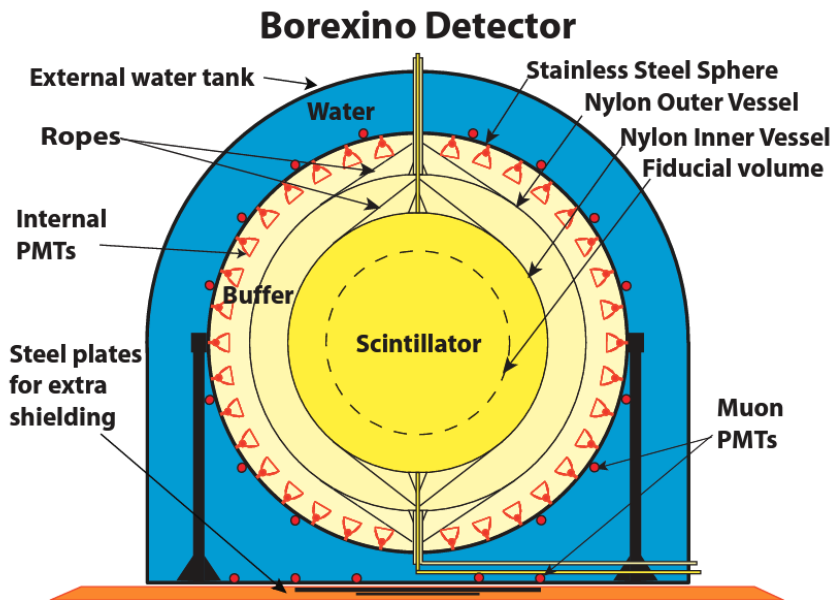


Figure 7.2: Schematic drawing of the Borexino detector [106].

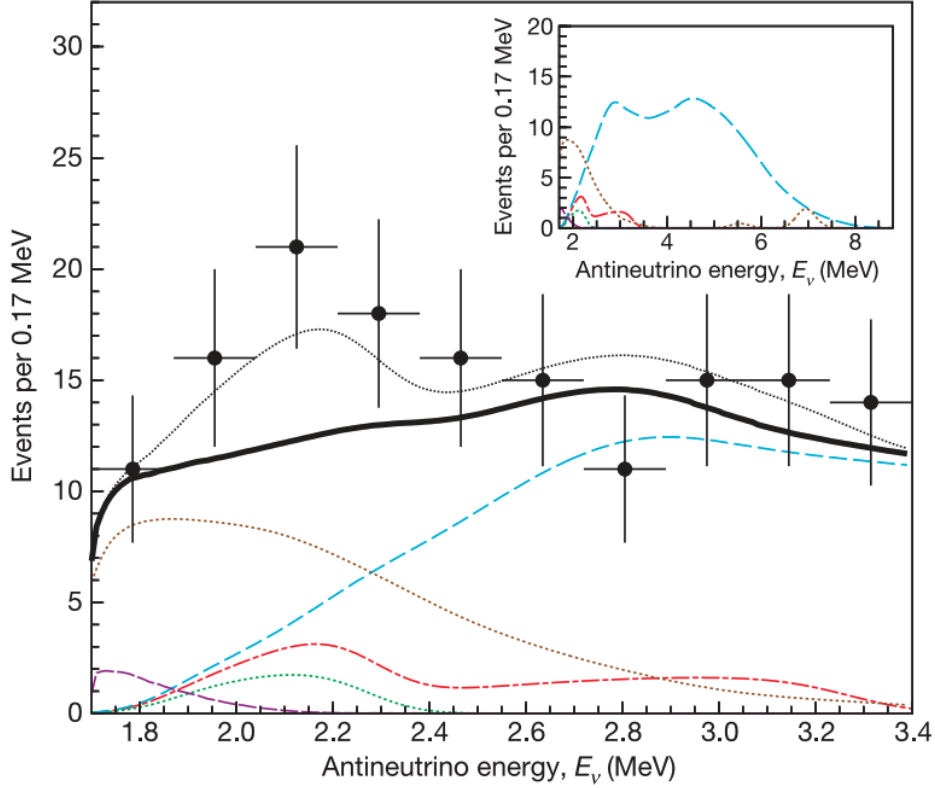


Figure 7.3: First ever measured antineutrino energy spectrum, taken at KamLAND. The main panel shows the data points with the total expectation given in the thin black dotted line. The total expected spectrum is shown without the geoneutrino signal as a thick black line. The expected ^{238}U and ^{232}Th signals are shown in a dot-dashed red line and dotted green line respectively. The brown dotted line shows the alpha-n background. [108]

they reported finding $9.9_{-3.4}^{+4.1}$ candidate geoneutrino events, shown in Figure 7.4.

The latest geoneutrino measurements come from KamLAND in 2022 [26] and Borexino in 2020 [25]. Figure 7.5 shows the spectral prompt event fit of 154 candidate events for a lifetime of 3263 days (Dec 9, 2007 - Apr 28, 2019). As can be seen in the blue dashed line, they have combined the U and Th spectra together, where the

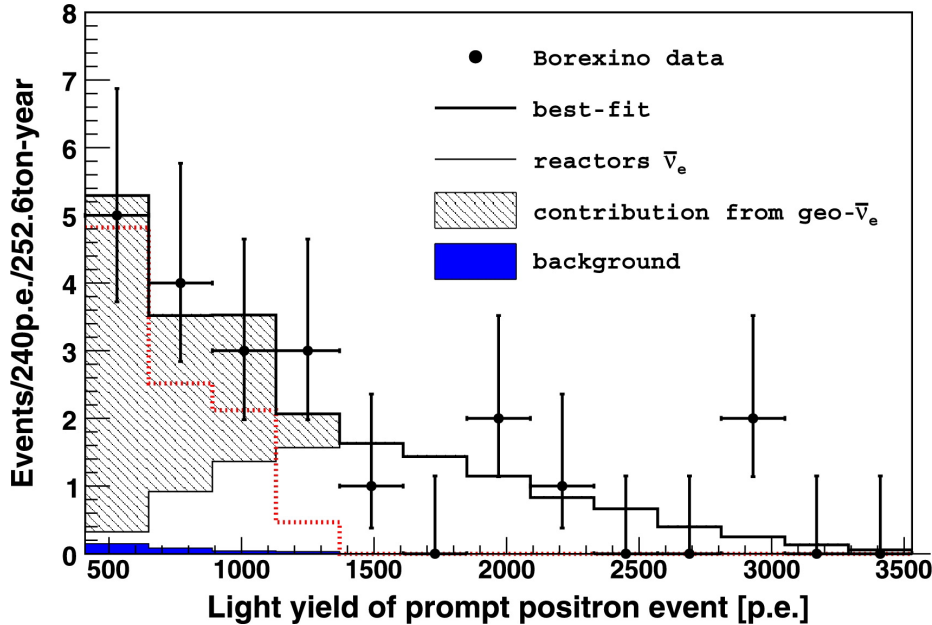


Figure 7.4: Light yield prompt event spectrum from 21 candidate events. The geoneutrino contribution is shown in the darker etched area. [109]

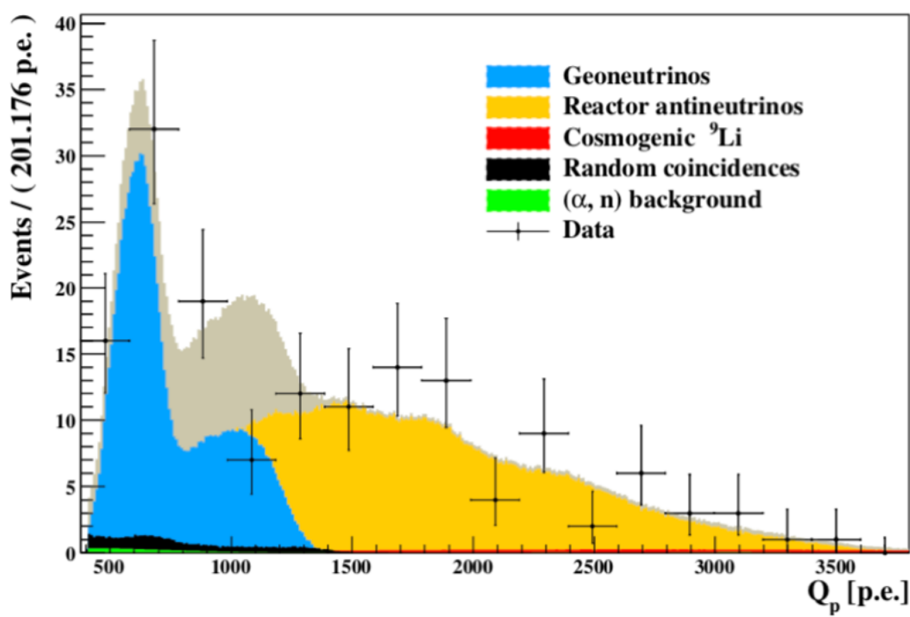


Figure 7.5: Light yield spectral plot of Borexino 154 prompt IBD candidate events. In blue geoneutrinos are shown for a fixed ratio of Th/U = 3.9. Reactor neutrinos are shown in yellow. [25]

abundance of these was fit with a fixed Th/U ratio of 3.9. The reactor neutrino background is represented in yellow, while the amplitude of the reactor neutrino spectra was kept free in this fit, with no constraints applied. Non-antineutrino backgrounds were fit with some constraints applied after the expected background levels were assessed. It is apparent that the result in Figure 7.5 had a very small contribution from non-antineutrino backgrounds, which the author of this thesis finds extremely impressive. Their best-fit result for geoneutrino events from this dataset is $54^{+18.3\%}_{-17.2\%}$ events. This uncertainty was largely dominated by statistics.

Figure 7.6 shows three periods of taken data at Kamland. The data was split into three periods due to gaps in time during which the detector underwent refurbishments. Hence for each dataset the detector status changed, and also in the third dataset, a very notable decrease in reactor neutrino flux is apparent since nearby reactors were shut down after the March 2011 Sendai earthquake. The plots show a stacked prompt event energy spectrum. In white we see the reactor neutrino spectrum. Above in green and peach, we see alphaN and accidental backgrounds. In the blue dashed region, the best-fit geoneutrino spectrum is shown. The combined lifetime of all three datasets is 5227 days (Mar 9, 2002 - Dec 31, 2020). The total combined best-fit geoneutrino signal is 174^{+31}_{-29} events.

A joint KamLAND and Borexino publication published in 2022 [110], discusses the results in terms of the radiogenic heat. They had a long geological discussion and concluded that the combined calculated radiogenic power from both latest results is $H^{KL+BX}(U + Th + K) = 20.8^{+7.3}_{-7.9}$ TW which currently falls within the 68% confidence range of MidQ models and is compatible at 1σ with LowQ model. This result slightly disfavors, but does not yet exclude HighQ models with any great degree of statistical

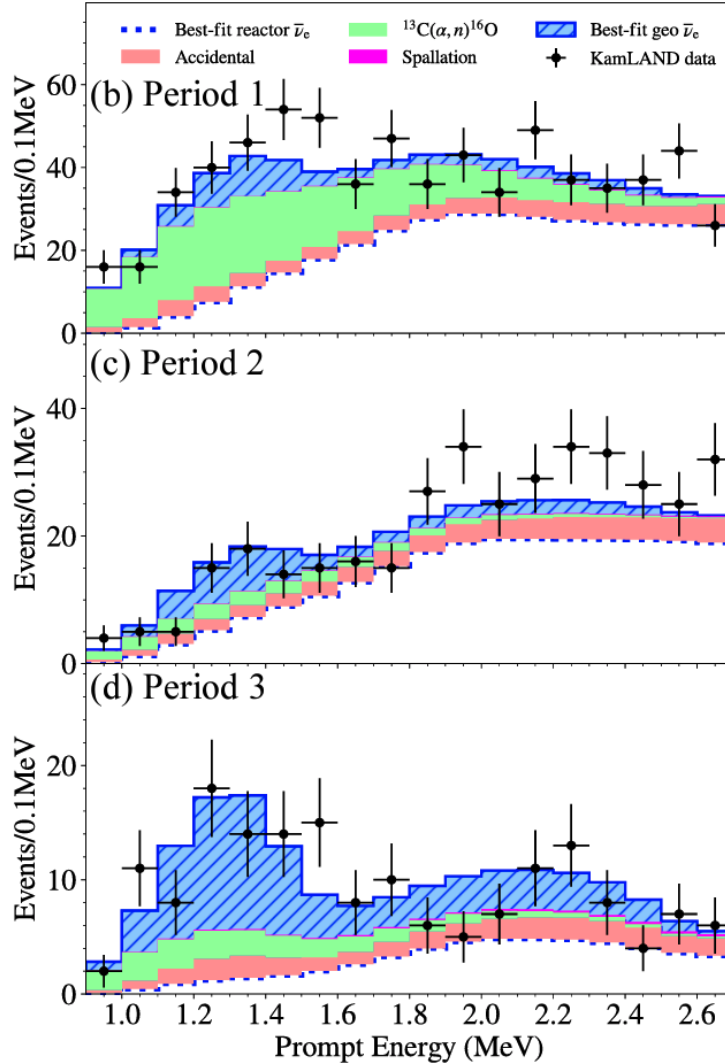


Figure 7.6: Stacked prompt energy spectrum for three periods of data. Period 1 is from 2002 to 2007, period 2 from 2007 to 2011 and period 3 from 2011 to 2020 [103]. The area in white is the fitted reactor neutrino background. above in green the alphaN and in peach accidental backgrounds. The blue-shaded area is the best-fit geoneutrino spectrum.

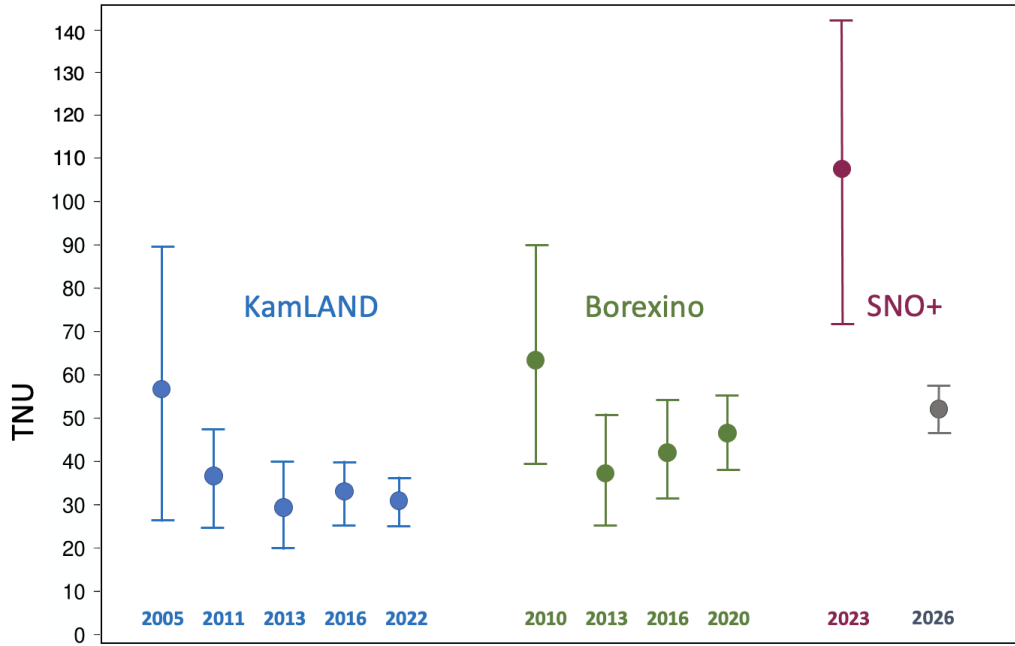


Figure 7.7: Illustration of the historical perspective on the geoneutrino measurements reported by KamLAND and Borexino. Each result is extrapolated to TNU. KamLAND results from [108][111][112][107][103]. Borexino results from [109][113][114][25]. For SNO+, in red the measurement from this thesis, as well as a prediction for a measurement using MidQ model production for 2 years worth of data in gray.

confidence.

Figure 7.7 shows a compilation of reported geoneutrino results by KamLAND and Borexino as a function of time. Included in the figure is the current measurement for SNO+ discussed in this thesis, as well as a prediction for 2 years worth of data of 52.8 ± 7.2 . The prediction was made by generating a dataset using the MidQ model and scaled reactor and alphaN expectation values, then fitting the dataset with the same fitting algorithm as discussed previously in this thesis. For the SNO+ measurement, the systematic uncertainties have not been included, as statistical errors

are dominant. The prediction also currently only includes a statistical error, however, the estimation of systematic errors is important for future measurements.

7.3 Future Work

There are a number of clear avenues for extending and improving the geoneutrino SNO+ analysis in future work.

- As noted in Chapter 6, the log likelihood fit of IBD coincidence data presented in this thesis greatly depends on the $^{13}\text{C}(\alpha,\text{n})^{16}\text{O}$ rate, which is set as an external constraint. The $^{13}\text{C}(\alpha,\text{n})^{16}\text{O}$ background can be studied and characterized more thoroughly. One improvement would be to go run-by-run in calculating the alpha-n background rate to obtain a tighter estimate of this background rate, instead of averaging the rate for all of the data-taking periods. Not mentioned in this thesis is work where I have divided the dataset into two regions of higher and lower alpha-n rates, and attempted to compare the results. However, as of yet there are not enough statistics to do a proper fit after this separation. With a larger dataset, a better measurement of alpha-n will be possible. Besides this inevitable statistical advantage, there is the fact that the rate of $^{13}\text{C}(\alpha,\text{n})^{16}\text{O}$ is decreasing over time as polonium is decaying in the SNO+ detector, and so we can look forward to lower backgrounds in future runs. Another large improvement might be obtained using the classifier discussed in section 5.5. This classifier is currently being studied by James Page, and there are plans to incorporate this into the next data and MC processing campaign. This could cut the alpha-n rate significantly and improve the geoneutrino result.

- Energy calibration is also improving in the SNO+ detector. Exploring the energy correction in terms of position and possibly deploying an AmBe source inside the detector volume at different locations would allow for better calibration of the IBD classifier, in particular, if the match between the MC time residual and data improves, then accurate proton recoil scintillation timing can be incorporated into the classifier. An internal AmBe source may also allow for a better check on the neutron detection efficiency so that the IBD MC efficiency can be calibrated. All of these improvements may allow for an increase in the fiducial volume, if event reconstruction improves enough to permit analysis nearer to the AV surface.
- The geoneutrino result presented here would greatly benefit from incorporating additional data. Besides simply accumulating more data with time, we note that while only “gold” runs were analyzed in this thesis, it would be useful to try incorporating “silver” and “bronze” runs as described in Section 6.1. Incorporating these would involve applying additional corrections to the reconstruction of the events, as for example, missing crates in some “silver” and “bronze” runs would leave a large gap in the PMT coverage. Therefore care would need to be taken to look at the energy and position reconstruction of the events for those runs.
- The work in this thesis determined the detection efficiency using only Monte Carlo simulations which have uncertainties that are much smaller than will be the case when systematics for the efficiency are fully considered. Therefore in future work, systematic uncertainties will have to be explored in detail. Another important systematic to study in future analyses will be the fiducial volume

uncertainty, expected to dominate in the determination of the uncertainty in the number of target protons. The fiducial volume uncertainty will depend on the event position reconstruction.

Bibliography

- [1] Wolfgang Pauli. Pauli Letter Collection: Letter to Lise Meitner. 1930. URL: <https://cds.cern.ch/record/83282>.
- [2] Fred L. Wilson. Fermi's Theory of Beta Decay. *American Journal of Physics*, 36(12):1150–1160, 1968.
- [3] F. Reines and C. L. Cowan. Detection of the Free Neutrino. *Phys. Rev.*, 92:830–831, 1953.
- [4] C. L. Cowan, F. Reines, F. B. Harrison, H. W. Kruse, and A. D. McGuire. Detection of the Free Neutrino: A Confirmation. *Science*, 124:103–104, 1956.
- [5] Raymond Davis, Jr., Don S. Harmer, and Kenneth C. Hoffman. Search for neutrinos from the sun. *Phys. Rev. Lett.*, 20:1205–1209, 1968.
- [6] John N. Bahcall, M. H. Pinsonneault, Sarbani Basu, and J. Christensen-Dalsgaard. Are standard solar models reliable? *Phys. Rev. Lett.*, 78:171–174, 1997.
- [7] Ziro Maki, Masami Nakagawa, and Shoichi Sakata. Remarks on the unified model of elementary particles. *Prog. Theor. Phys.*, 28:870–880, 1962.

- [8] G. Danby, J-M. Gaillard, K. Goulianos, L. M. Lederman, N. Mistry, M. Schwartz, and J. Steinberger. Observation of High-Energy Neutrino Reactions and the Existence of Two Kinds of Neutrinos. *Phys. Rev. Lett.*, 9:36–44, 1962.
- [9] K. Kodama et al. and the DONUT Collaboration. Observation of tau neutrino interactions. *Phys. Lett. B*, 504:218–224, 2001.
- [10] K. Lande, B. T. Cleveland, T. Daily, R. Davis, J. Distel, C. K. Lee, A. Weinberger, P. Wildenhain, and J. Ullman. Solar neutrino observations with the Homestake ^{37}Cl detector. *AIP Conf. Proc.*, 243:1122–1133, 1992.
- [11] B. Pontecorvo. Neutrino Experiments and the Problem of Conservation of Leptonic Charge. *Zh. Eksp. Teor. Fiz.*, 53:1717–1725, 1967.
- [12] Robert Ehrlich. Possible evidence for neutrino oscillations in the Brookhaven solar-neutrino experiment. *Phys. Rev. D*, 18:2323–2328, 1978.
- [13] S. Fukuda et al. and the Super-Kamiokande Collaboration. The Super-Kamiokande Detector. *Nuclear Instruments and Methods in Physics Research Section A: Accelerators, Spectrometers, Detectors and Associated Equipment*, 501(2):418–462, 2003.
- [14] Y. Fukuda et al. and the Super-Kamiokande Collaboration. Evidence for Oscillation of Atmospheric Neutrinos. *Phys. Rev. Lett.*, 81:1562–1567, 1998.
- [15] Q. R. Ahmad et al. and the SNO Collaboration. Measurement of the Rate of $\nu_e + d \rightarrow p + p + e^-$ Interactions Produced by ^8B Solar Neutrinos at the Sudbury Neutrino Observatory. *Phys. Rev. Lett.*, 87:071301, 2001.

- [16] Q. R. Ahmad et al. and the SNO Collaboration. Direct Evidence for Neutrino Flavor Transformation from Neutral-Current Interactions in the Sudbury Neutrino Observatory. *Phys. Rev. Lett.*, 89:011301, 2002.
- [17] Itaru Shimizu, the KamLAND, and KamLAND-Zen Collaborations. Kamland. *Proceedings of Science*, 244:048, 2015.
- [18] T. Araki et al. and the KamLAND Collaboration. Measurement of Neutrino Oscillation with KamLAND: Evidence of Spectral Distortion. *Phys. Rev. Lett.*, 94:081801, 2005.
- [19] Yi Cai, Tao Han, Tong Li, and Richard Ruiz. Lepton Number Violation: Seesaw Models and Their Collider Tests. *Front. in Phys.*, 6:40, 2018.
- [20] R. L. et al. Workman. Review of Particle Physics. *PTEP*, 2022:083C01, 2022.
- [21] Evgeny K. Akhmedov. Neutrino physics. In *ICTP Summer School in Particle Physics*, pages 103–164, 6 1999. <http://arxiv.org/abs/hep-ph/0001264> arXiv: hep-ph/0001264.
- [22] Nikolas I. Christensen and Walter D. Mooney. Seismic velocity structure and composition of the continental crust: A global view. *Journal of Geophysical Research: Solid Earth*, 100(B6):9761–9788, 1995.
- [23] Sanshiro Enomoto. Neutrino Geophysics and Observation of Geo-Neutrinos at KamLAND. *PhD Thesis, Tohoku University*, 2005.
URL: <http://kamland.stanford.edu/GeoNeutrinos/GeoNuResult/SanshirosDoctoralDissertation.pdf>.

- [24] Sanshiro Enomoto. Geoneutrino spectrum and luminosity. URL: <https://www.awa.tohoku.ac.jp/\%7Esanshiro/research/geoneutrino/spectrum/>.
- [25] M. Agostini et al. and the Borexino collaboration. Comprehensive geoneutrino analysis with Borexino. *Phys. Rev. D*, 101:012009, 2020.
- [26] S. Abe et al. and The KamLAND Collaboration. Abundances of Uranium and Thorium Elements in Earth Estimated by Geoneutrino Spectroscopy. *Geophysical Research Letters*, 49(16):e2022GL099566, 2022.
- [27] Jean-Claude Mareschal and Claude Jaupart. Radiogenic heat production, thermal regime and evolution of continental crust. *Tectonophysics*, 609:524–534, 2013.
- [28] Damon Teagle and Benoît Ildefonse. Journey to the mantle of the Earth. *Nature*, 471(7339):437–439, 2011.
- [29] Sean N Raymond and Alessandro Morbidelli. Planet formation: key mechanisms and global models. *Demographics of Exoplanetary Systems: Lecture Notes of the 3rd Advanced School on Exoplanetary Science*, pages 3–82, 2022.
- [30] Dallas Abbott, Lee Burgess, John Longhi, and Walter HF Smith. An empirical thermal history of the Earth’s upper mantle. *Journal of Geophysical Research: Solid Earth*, 99(B7):13835–13850, 1994.
- [31] Thorne Lay, John Hernlund, and Bruce Buffett. Core–mantle boundary heat flow. *Nature Geoscience*, 1, 2008.
- [32] J. H. Davies and D. R. Davies. Earth’s surface heat flux. *Journal of Geophysical Research: Solid Earth*, 1(1):5–24, 2010.

- [33] H. N. Sharpe and W. R. Peltier. Parameterized mantle convection and the earth's thermal history. *Geophysical Research Letters*, 5(9):737–740, 1978.
- [34] Jun Korenaga. Energetics of mantle convection and the fate of fossil heat. *Geophysical Research Letters*, 30:1437–, 2003.
- [35] Richard Carlson et al. How Did Early Earth Become Our Modern World? *Annual Review of Earth and Planetary Sciences*, 42:151–78, 2013.
- [36] V. M. Goldschmidt. The principles of distribution of chemical elements in minerals and rocks. The Seventh Hugo Müller Lecture, delivered before the Chemical Society on March 17th, 1937. *J. Chem. Soc.*, pages 655–673, 1937.
- [37] G. Bellini, A. Ianni, L. Ludhova, F. Mantovani, and W.F. McDonough. Geo-neutrinos. *Progress in Particle and Nuclear Physics*, 73:1–34, 2013.
- [38] W.F. McDonough. Compositional Model for the Earth's Core. In Heinrich D. Holland and Karl K. Turekian, editors, *Treatise on Geochemistry*, pages 547–568. Pergamon, Oxford, 2003.
- [39] M. Javoy et al. The chemical composition of the Earth: Enstatite chondrite models. *Earth and Planetary Science Letters*, 293(3):259–268, 2010.
- [40] H. O'Neill and H. Palme. Collisional erosion and the non-chondritic composition of the terrestrial planets. *Philosophical Transactions of the Royal Society A: Mathematical, Physical and Engineering Sciences*, 366(1883):4205–4238, 2008.
- [41] W.F. McDonough and S. S. Sun. The composition of the Earth. *Chemical Geology*, 120(3):223–253, 1995.

- [42] Jeroen van Hunen. Geodynamics. *Geophysical Journal International*, 200:1236–1236, 2015.
- [43] William McDonough, Ondřej Šrámek, and Scott Wipperfurth. Radiogenic power and geoneutrino luminosity of the Earth and other terrestrial bodies through time. *Geochemistry, Geophysics, Geosystems*, 21(7):e2019GC008865.
- [44] Ondřej Šrámek. Geoneutrinos: Seeing the Earth With Particle Physics. *Encyclopedia of Geology*, pages 258–269, 2020.
- [45] F. Duncan, A. J. Noble, and D. Sinclair. The Construction and Anticipated Science of SNOLAB. *Annual Review of Nuclear and Particle Science*, 60(1):163–180, 2010.
- [46] V. Albanese et al. and the SNO+ Collaboration. The SNO+ experiment. *Journal of Instrumentation*, 16(08):P08059, 2021.
- [47] M. Anderson et al. and the SNO+ Collaboration. Measurement of the ^8B solar neutrino flux in SNO+ with very low backgrounds. *Phys. Rev. D*, 99:012012, 2019.
- [48] A. Allega et al. and the SNO+ Collaboration. Improved search for invisible modes of nucleon decay in water with the SNO + detector. *Phys. Rev. D*, 105:112012, 2022.
- [49] J. Paton. Event-by-event direction reconstruction in a liquid scintillator detector, Publication in preparation. 2022. URL: https://indico.stfc.ac.uk/event/324/contributions/3274/attachments/920/1634/JPaton_Slides.pdf.

- [50] Ziyi et al. Guo. Muon flux measurement at China Jinping Underground Laboratory. *Chin. Phys. C*, 45(2):025001, 2021.
- [51] S. T. Dye. Geoneutrinos and the radioactive power of the Earth. *Reviews of Geophysics*, 50(3), 2012.
- [52] S.Seibert et al. RAT User's Guide. 2023. URL: <https://rat.readthedocs.io/en/latest/index.html>.
- [53] S. Agostinelli et al. GEANT4—a simulation toolkit. *Nucl. Instrum. Meth. A*, 506:250–303, 2003.
- [54] Rene Brun and Fons Rademakers. Root: An object oriented data analysis framework. *Nuclear Instruments and Methods in Physics Research Section A: Accelerators, Spectrometers, Detectors and Associated Equipment*, 389(1):81–86, 1997.
- [55] Ondřej Šrámek, Bedřich Roskovec, Scott A. Wipperfurth, Yufei Xi, and William F. McDonough. Revealing the Earth’s mantle from the tallest mountains using the Jinping Neutrino Experiment. *Scientific Reports*, 6(1):33034, 2016.
- [56] Gabi Laske, Guy Masters, Zhitu Ma, and Mike Pasyanos. Update on CRUST1.0 - A 1-degree global model of Earth’s crust. *Abstract EGU2013-2658 presented at 2013 Geophys. Res. Abstracts 15*, 15:2658, 2013.
- [57] C.G.L. Bassin, Gabi Laske, and Guy Masters. The current limits of resolution for surface wave tomography in North America. *Eos, Transactions American Geophysical Union*, 81:F897, 2000.

- [58] Michael E. Pasyanos, T. Guy Masters, Gabi Laske, and Zhitu Ma. LITHO1.0: An updated crust and lithospheric model of the Earth. *Journal of Geophysical Research: Solid Earth*, 119(3):2153–2173, 2014.
- [59] Yu Huang, Viacheslav Chubakov, Fabio Mantovani, Roberta L. Rudnick, and William F. McDonough. A reference earth model for the heat-producing elements and associated geoneutrino flux. *Geochemistry, Geophysics, Geosystems*, 14(6):2003–2029, 2013.
- [60] W.M. White and E.M. Klein. Composition of the oceanic crust. *Treatise on Geochemistry (Second Edition)*, 2014.
- [61] Terry Plank. The chemical composition of subducting sediments. *Treatise on Geochemistry (2nd Ed.) (Vol. 4): The Crust*, 4:607–629, 11 2013.
- [62] Roberta Rudnick and Sally Gao. Composition of the continental crust. *treatise geochem* 3:1-64. *Treatise on Geochemistry*, 3:1–64, 11 2003.
- [63] Adam M. Dziewonski and Don L. Anderson. Preliminary reference Earth model. *Physics of the Earth and Planetary Interiors*, 25(4):297–356, 1981.
- [64] Ricardo Arevalo Jr., William F. McDonough, Andreas Stracke, Matthias Willbold, Thomas J. Ireland, and Richard J. Walker. Simplified mantle architecture and distribution of radiogenic power. *Geochemistry, Geophysics, Geosystems*, 14(7):2265–2285, 2013.

- [65] Scott A. Wipperfurth, Meng Guo, Ondřej Šrámek, and William F. McDonough. Earth’s chondritic th/u: Negligible fractionation during accretion, core formation, and crust-mantle differentiation. *Earth and Planetary Science Letters*, 498:196–202, 2018.
- [66] Scott Wipperfurth, Ondřej Šrámek, and William McDonough. Reference Models for Lithospheric Geoneutrino Signal. *Journal of Geophysical Research: Solid Earth*, 125, 02 2020.
- [67] Ann Therriault, AD Fowler, and Richard Grieve. The Sudbury Igneous Complex: A Differentiated Impact Melt Sheet. *Economic Geology*, 97:1521–1540, 2002.
- [68] Virginia Strati, Scott A. Wipperfurth, Marica Baldoncini, William F. McDonough, and Fabio Mantovani. Perceiving the Crust in 3-D: A Model Integrating Geological, Geochemical, and Geophysical Data. *Geochemistry, Geophysics, Geosystems*, 18(12):4326–4341, 2017.
- [69] Erick Adam, G Perron, B Milkereit, Jianjun Wu, AJ Calvert, M Salisbury, Pierre Verpaelst, and Denis-Jacques Dion. A review of high-resolution seismic profiling across the Sudbury, Selbaie, Noranda, and Matagami mining camps. *Canadian Journal of Earth Sciences*, 37(2-3):503–516, 2000.
- [70] Oladele Olaniyan, Richard S. Smith, and Bruno Lafrance. Regional 3D geophysical investigation of the Sudbury Structure. *Interpretation*, 3(2):SL63–SL81, 2015.

- [71] Yu Huang, Virginia Strati, Fabio Mantovani, Steven B. Shirey, and William F. McDonough. Regional study of the Archean to Proterozoic crust at the Sudbury Neutrino Observatory (SNO+), Ontario: Predicting the geoneutrino flux. *Geochemistry, Geophysics, Geosystems*, 15(10):3925–3944, 2014.
- [72] L. G. Sammon, C. Gao, and W. F. McDonough. Lower Crustal Composition in the Southwestern United States. *Journal of Geophysical Research: Solid Earth*, 125(3):e2019JB019011, 2020.
- [73] USArray. A Continental Scale Seismic Observatory, 2021. URL: <http://www.usarray.org/researchers/data>.
- [74] G. Audi, F. G. Kondev, Meng Wang, W. J. Huang, and S. Naimi. The NUBASE2016 evaluation of nuclear properties. *Chinese Physics. C, High Energy Physics and Nuclear Physics*, 41(3), 2017.
- [75] Tosaka. Decay chain 4n+2, Uranium series. 2008. URL: [https://en.wikipedia.org/wiki/File:Decay_chain\(4n%2B2,_Uranium_series\).PNG](https://en.wikipedia.org/wiki/File:Decay_chain(4n%2B2,_Uranium_series).PNG).
- [76] Charlie Mills. Improved sensitivity to Δm_{21}^2 by classification of the $^{13}\text{C}(\alpha, n)^{16}\text{O}$ background in the SNO+ antineutrino analysis. *PhD Thesis, University of Sussex*, 2022. URL: <https://snoplus.phy.queensu.ca/theses/cmills.pdf>.
- [77] Ingrida Semenec. Design of a neutron calibration source for the SNO+ experiment. *MSc Thesis, Laurentian University*, 2017. URL: <https://zone.biblio.laurentian.ca/handle/10219/2992>.
- [78] Ling-Jian Meng. Lecture notes: Interactions of Neutrons with Matter, 2023. URL: <https://courses.grainger.illinois.edu/NPRE441/sp2023>.

- [79] Hiroshi Ito, Kohei Wada, Takatomi Yano, Yota Hino, Yuga Ommura, Masayuki Harada, Akihiro Minamino, and Masaki Ishitsuka. Analyzing the neutron and γ -ray emission properties of an americium-beryllium tagged neutron source. 2023. <http://arxiv.org/abs/2304.12153> `arXiv:2304.12153`.
- [80] M.B. Chadwick et al. ENDF/B-VII.1 nuclear data for science and technology: Cross sections, covariances, fission product yields and decay data. *Nuclear Data Sheets*, 112(12):2887 – 2996, 2011.
- [81] Charlie Mills. AlphaNReactor IBD Classifier Documentation, SNO+ Internal Document 6773-v4.
- [82] Marc Paterno. Calculating efficiencies and their uncertainties. 2004. URL: <https://www.osti.gov/biblio/15017262>.
- [83] Iwan Morton-Blake. Partial Fill: BiPo214 Time Residuals + Energy Data/MC comparison, SNO+ Internal Document 6796-v1.
- [84] Anthony Zummico. Residual Energy Correction, SNO+ Internal Document 7896-v1.
- [85] M. Anderson and the SNO+ Collaboration. Development, characterisation, and deployment of the SNO+ liquid scintillator. *JINST*, 16(05):P05009, 2021.
- [86] Richard Perron. CEPSA Quimica Certificate of Analysis, private communication.
- [87] Jie Zhao, Zeyuan Yu, Jianglai Liu, Xiaobo Li, Feihong Zhang, and Dongmei Xia. $^{13}\text{C}(\text{alpha},\text{n})^{16}\text{O}$ background in a liquid scintillator based neutrino experiment, 2014. <http://arxiv.org/abs/1312.6347> `arXiv:1312.6347`.

- [88] F. P. An et al. and the Daya Bay Collaboration. A side-by-side comparison of Daya Bay antineutrino detectors. *Nucl. Instrum. Meth. A*, 685:78–97, 2012.
- [89] Belina Von Krosigk. Measurement of proton and α particle quenching in LAB based scintillators and determination of spectral sensitivities to supernova neutrinos in the SNO+ detector. *PhD Thesis, Dresden, Tech. U., Dept. Math.*, 2015. URL: <https://snoplus.phy.queensu.ca/theses/bvk.pdf>.
- [90] Koichiro Nishikawa and Takaaki Kajita. Atmospheric Neutrinos. *Advances in High Energy Physics*, 2012:504715, 2012.
- [91] C. Lin. Atmospheric neutrinos in partial fill, SNO+ Internal Document 6958.
- [92] Costas Andreopoulos, Christopher Barry, Steve Dytman, Hugh Gallagher, Tomasz Golan, Robert Hatcher, Gabriel Perdue, and Julia Yarba. The GENIE Neutrino Monte Carlo Generator: Physics and User Manual, 2015. <http://arxiv.org/abs/1510.05494> arXiv:1510.05494.
- [93] F. P. An et al. and the Daya Bay Collaboration. Improved measurement of the reactor antineutrino flux and spectrum at Daya Bay. *Chinese Physics C*, 41(1):013002, 2017.
- [94] K. et al. Eguchi and the KamLAND Collaboration. First results from KamLAND: Evidence for reactor anti-neutrino disappearance. *Phys. Rev. Lett.*, 90:021802, 2003.
- [95] IESO. Generator Output Capability Month Report. 2023. URL: <http://reports.ieso.ca/public/GenOutputCapabilityMonth>.

- [96] IAEA. The Database on Nuclear Power Reactors, 2023. URL: <https://pris.iaea.org/PRIS/home.aspx>.
- [97] Paweł Mekarski. Electron Antineutrinos in the Water Phase of the SNO+ Experiment. *PhD Thesis, University of Alberta*, 2018. URL: <https://era.library.ualberta.ca/items/daa7b99c-1970-4230-bc72-b51ed29b414f>.
- [98] Francesco Capozzi, Eleonora Di Valentino, Eligio Lisi, Antonio Marrone, Alessandro Melchiorri, and Antonio Palazzo. Global constraints on absolute neutrino masses and their ordering. *Phys. Rev. D*, 95:096014, 2017.
- [99] K. et al. Abe and the Super-Kamiokande Collaboration. Solar Neutrino Measurements in Super-Kamiokande-IV. *Phys. Rev. D*, 94(5):052010, 2016. <https://doi.org/10.1103/PhysRevD.94.052010> doi:10.1103/PhysRevD.94.052010.
- [100] J. E. Page. Reactor Antinu Flux Scaling, SNO+ Internal Document 7676-v7.
- [101] S. et al. Abe and the KamLAND Collaboration. Production of radioactive isotopes through cosmic muon spallation in KamLAND. *Phys. Rev. C*, 81:025807, 2010.
- [102] SNO+ collaboration. Water UniDoc, SNO+ Internal Document 3461.
- [103] S Abe et al. and the KamLAND Collaboration. Abundances of Uranium and Thorium Elements in Earth Estimated by Geoneutrino Spectroscopy. *Geophysical Research Letters*, 49(16):e2022GL099566, 2022.

- [104] Wouter Verkerke and David Kirkby. The rooFit toolkit for data modeling. In *Statistical Problems in Particle Physics, Astrophysics and Cosmology*, pages 186–189. World Scientific, 2006.
- [105] F. Capozzi, E. Lisi, A. Marrone, and A. Palazzo. Current unknowns in the three neutrino framework. *Prog. Part. Nucl. Phys.*, 102:48–72, 2018.
- [106] G. Alimonti et al. and the Borexino Collaboration. The Borexino detector at the Laboratori Nazionali del Gran Sasso. *Nuclear Instruments and Methods in Physics Research Section A: Accelerators, Spectrometers, Detectors and Associated Equipment*, 600(3):568–593, 2009.
- [107] H. Watanabe for the KamLAND Collaboration. KamLAND. Presented at International Workshop Neutrino Research and Thermal Evolution of the Earth, Tohoku University, Sendai, Japan, 25–27 October 2016. URL: https://www.tfc.tohoku.ac.jp/wp-content/uploads/2016/10/04_HirokoWatanabe_TFC2016.pdf.
- [108] T. Araki et al. and the KamLAND Collaboration. Experimental investigation of geologically produced antineutrinos with KamLAND. *Nature*, 436(7050):499–503, 2005.
- [109] G. Bellini et al. and the Borexino Collaboration. Observation of Geo-Neutrinos. *Phys. Lett. B*, 687:299–304, 2010.
- [110] G. Bellini, K. Inoue, F. Mantovani, A. Serafini, V. Strati, and H. Watanabe. Geoneutrinos and geoscience: an intriguing joint-venture. *La Rivista del Nuovo Cimento*, 45(1):1–105, 2022.

- [111] A. Gando et al. and The KamLAND Collaboration. Partial radiogenic heat model for Earth revealed by geoneutrino measurements. *Nature Geoscience*, 4(9):647–651, 2011.
- [112] A. Gando et al. and the KamLAND Collaboration. Reactor on-off antineutrino measurement with KamLAND. *Phys. Rev. D*, 88:033001, 2013.
- [113] G. Bellini et al. and the Borexino Collaboration. Measurement of geo-neutrinos from 1353 days of Borexino. *Physics Letters B*, 722(4):295–300, 2013.
- [114] R Roncin, M Agostini et al., and the Borexino Collaboration. Geo-neutrino results with Borexino. *Journal of Physics: Conference Series*, 675(1):012029, 2016.